Near-Field Scanning Optical Microscopy Characterization of Metastructures

Near-field Scanning Optical Microscopy Characterization of Metastructures

A DISSERTATION PRESENTED
BY
DANIEL THOMAS WINTZ
TO
THE SCHOOL OF ENGINEERING AND APPLIED SCIENCES

IN PARTIAL FULFILLMENT OF THE REQUIREMENTS
FOR THE DEGREE OF
DOCTOR OF PHILOSOPHY
IN THE SUBJECT OF
APPLIED PHYSICS

HARVARD UNIVERSITY
CAMBRIDGE, MASSACHUSETTS
DECEMBER 2016

Dissertation advisor: Federico Capasso Daniel Wintz

Near-field Scanning Optical Microscopy Characterization of Metastructures

ABSTRACT

Metamaterials and metasurfaces, defined by their ability to achieve functionalities above and beyond normal materials and surfaces, have found a myriad of applications in the fields of electronics, condensed matter, and most notably (for the subject of this thesis), optics. These metastructures typically consist of materials intelligently patterned or structured in a way to realize some traditionally difficult or previously impossible to achieve material property or function. Simply put, metastructures allow for not only the creation of new optical elements, but also the expansion and improvement of existing optics. On

the more fundamental research side, just by virtue of their novelty, metastructures inherently open up new research paths. Thus, the focus of this thesis is twofold: the creation of optical elements with exotic wavefront control and the characterization of these new optical elements.

The optical elements studied here are all devices based on the control of surface plasmon polaritons (SPPs). While the advantages and disadvantages of using SPPs will be discussed later, the use of SPPs as the electromagnetic modes of study and manipulation suggests, and in some cases necessitates, the use of a specific characterization technique: near-field scanning optical microscopy (NSOM). NSOM is able to probe the electromagnetic near-field of the surface plasmons, enabling direct optical detection of the otherwise non-radiative SPPs.

First, we describe the creation and measurement of a metastructure that acts as a switchable and tunable SPP lens. The metalens has four operating wavelengths in the visible and exhibits on/off switching based on the polarization of the incident light. The performance of the lens is characterized by an effective

numerical aperture of $NA \approx .7$ and a concentration of optical energy of an order of magnitude higher than an isotropic source of SPPs. This corresponds to an efficiency of roughly 25%. Beyond the performance of the actual lens, the design principle itself is also noteworthy. The creation methodology of the metalens is based on holographic principles and is the driving force behind the metalens' ability to switchably focus the operating wavelengths. We note that the design principle is not inherent to surface plasmons, and can act as a blueprint for free space lenses as well.

Next, we demonstrate a metastructure that is capable of creating and steering surface plasmon wavefronts based on the angle of incidence and the spin angular momentum of the photons impinging on the metastructure. An interesting and elegant pedagogical analogy to wakes is made, in that, the metastructure creates surface plasmon wakes. Wakes are a general wave phenomenon whereby a disturbance propagates through a medium faster than the phase velocity of the waves it creates. Examples of this in nature include boat wakes, sonic booms, and Cherenkov radiation. Our experiment was the first observation of this effect

with surface plasmons. We achieved this by creating a 'running wave of polarization' along a one-dimensional metastructure. This running wave of polarization has a specifically tailored phase velocity, allowing for the creation of surface plasmon wakes. By using a suitably designed metastructure, we demonstrated the steering of surface plasmon wakes. Furthermore, the sign of the wavevector of the wake is dependent on the spin-angular-momentum of the incident light, and an analogy to Cherenkov and reversed Cherenkov radiation is discussed.

The next chapter of this thesis expands, experimentally and theoretically, on the previous section regarding Cherenkov surface plasmon wake generation. In designing a new metastructure, we demonstrate two anisotropies in surface plasmon wake generation. The first anisotropy is an asymmetric wake angle—wakes that propagate away from the metastructure at different angles. We note that, in general, this is not possible with just a single medium with a single refractive index. The second anisotropy is a focusing/defocusing effect for the two wakes created. These asymmetries are made possible by the use of a more

complex metastructure—a single line of sequentially rotated bimodal V-shaped antennas. The crux of the metastructure performance is that the second mode of the V-antenna breaks the symmetry of the system and can be used to create anisotropies in surface plasmon wavefront generation.

Lastly, we discuss a work-in-progress experiment utilizing techniques developed during the course of this thesis. The motivation for this work hinges on the fact that measuring the refractive index of small-area ($< 100\ \mu m^2$), thin ($< 100\ nm$) films is notoriously difficult using common techniques such as ellipsometry. We develop a methodology using surface waves to measure two unknowns: the in-plane $n_{||}$ and out-of-plane $n_{\perp}$ refractive index of exfoliated hexagonal boron nitride (h-BN). Elegantly, surface waves are well-suited as measurement tools for two-dimensional materials as they are able to interact along the *length* of the structure, rather than the thickness. Two experiments are performed to determine the two unknown refractive indices. The first experiment utilizes a standing wave mode in the h-BN to probe the in-plane refractive index only, and the second experiment employs SPPs, which are able to probe both the in-plane

and out-of-plane refractive indices. Given the results of both experiments, both the in-plane and out-of-plane refractive indices can be uniquely determined for a range of visible frequencies. In the spirit of science, we note that this is an ongoing experiment and our analysis has not fully concluded as of yet, but promising preliminary results are contained herein.

Table of Contents

List of Figures

List of Tables

Dedicated to my parents.

Acknowledgements

Wow. Where to even begin? Looking back, when I started my Ph.D., I really had no idea what I was getting myself into. I may still not know, but I did learn a few things. And for all the things I didn't know before I started… these were the people that helped me figure some of them out.

First, to my adviser, Professor Federico Capasso –thank you. You took me in at the beginning of my G4 year, and taught me what I believe to be the most important lesson of my graduate school career: the most important thing is *vision*. You're a fantastic manager and scientist; you're creative and supportive, and it is your vision that has created such a successful lab. Vision for projects, vision for applications of projects, vision for collaborations, vision for lab atmosphere, vision for philosophy of science, vision for papers and the story they should tell, vision, vision, vision. You care about the bigger picture, but don't get

lost in it. I can give no higher praise. Thank you for fostering my growth and leading by example.

Antonio Ambrosio, my Italian friend. This thesis literally would never have happened without you, or it would have been turned in several years later (if at all). Thank you for teaching me the ways of NSOM, for fixing all the dumb mistakes I made, for not getting mad when I broke tip after tip for ungodly stupid reasons. This thesis is like half yours. Honestly. I never would have made it without you, and for that I am eternally grateful. You're an inspiration really—honest, hardworking, intelligent. My first day in lab you told me, 'so, if you want to work on this project, on NSOM, you should know this: it's hard and it's a lot of work'. I should have quit right then. Haha, kidding. I wouldn't change a thing mate. Well, maybe the Nanonics software. Now, let's go to California?

Patrice Genevet, you crazy Frenchman. I'll never forget how you broke a spectrometer in 30 seconds, just by clicking a bunch of buttons. You broke

hardware by messing with the *software*—that's a special talent. Another person who deserves much credit for this thesis. The ducks and holograms started as ideas in that crazy French head of yours, and even when Federico told us not to do the holograms we left his office and you said 'no way, we are going to do it anyway'. Good vision—thanks buddy. I was at my best when you were around; there's no way around it. The Harvard Duck Dynasty lives on. Quack quack my friend.

Alex Woolf, a true partner in crime. I never would have made it without you, mentally or logistically. I'll never forget: Tuesday September 10th, 2013. We are sitting at the bar past midnight, you helping me hash it out if I should leave my old lab, and ask me: "Would you consider joining the Capasso group, cause you should." I say okay, you email Federico an immensely flattering (and untrue!) email, he calls you at 12:20AM while we are still at the bar. "He's intrigued, but won't meet with you until you're out of the other lab." I quit the next day Wednesday at 5pm and joined the Capasso lab Thursday. Hopefully Federico doesn't read this far, because thank you for lying to him for me. You told

Federico that I had a ton of experimental experience—I had none. Haha. But, you had faith in me that I would succeed anyway. So, thank you. And thank god for Antonio and his ability to take people from NSOM zero to NSOM hero. I'll never forget the NSOM dance party we had with Toby in lab at 2pm on a Wednesday—complete with the 'SNOM song' and 'My hero (tip)'. Please burn your wingman shirt and here's a friendly reminder to check for socks underneath your sink from time to time. Sorry Sylvie. Speaking of which, thank you as well. You're one of my best friends and I love both of you guys—you both have made my life immensely better—I can only hope to do a fraction of the same for you guys.

Tommi Hakala, yoooooo maaaaaate. You taught me a lot of things at the beginning of my grad school career, both science and life-wise. However, a few things of note: snooker is not better than pool, no matter how many little red balls you hit into the smaller pockets. Santa Claus is not a goat, I don't care if Finnish people created him. Finnish mulled wine, however, that stuff is a gem. I miss you mate. Thanks for keeping me sane—our routine was impeccable.

xxx

Every time we got a nasty email, had a bad meeting, or just in general felt demotivated—Graaaaaaaaaaaafton mate. The bartenders there still recognize me—I think that's a good thing. Speaking of which, we should still publish that graphene paper. You were the original BHP #throwinthursdays partner, and I'll always love you for that. Everyone I know calls that game 'Finnish Killer', named after you. You're one of the coolest, smartest people I know and I miss you all the time. Thanks for being a great friend and mentor, you mean a lot to me. Can't wait to come visit you in Finland, hopefully this summer.

Jesse Crossno—thanks for being a great friend, and particularly for keeping me sane at the end. That trip to the beach helped me out so much, and no, I don't mean the one where we got hailed on at the beach. Hail. At. The. Beach. Thanks for all the good times at lunch, even if you are a shitty tipper. There's nobody else I'd rather watch The Bachelor with, and that's saying something. You're definitely responsible for the best thanksgiving I've ever had—1000 pushups and us finding out Balthasar hates the army. You're holistically intelligent, fun, and a great friend.

To my committee members, Professor Marko Loncar and Professor Philip Kim, thank you. Professor Loncar, sadly we didn't get to collaborate beyond the occasional borrowing of the superK or loaning Haig a beam profiler. Professor Kim, collaborating with you has been a pleasure. Hopefully the rough draft of the BN paper I put in isn't too rough! Haha. Thank you both for taking time to be on my committee.

To my labmates in the early years—Rui, Evan, Danny, Tony, Xi, thanks for the support. To my collaborators—Alan, Romain, Ke, Luis, Rob, thanks for all your help. To the younger students that helped me immensely towards the end—Kundan and Alex, thank you. You guys were pleasures to work with.
To the labmates I'd always have thoughtful discussions with—Toby, Mikhail, Balthasar, thank you.

To my lifelong grad school friends over the years, thank you. Raj—my first grad school friend, feels like we grew up together in a way. Dogus, the Turkish

Hammer, you're the middle to my setter. To both of you guys—5 for 5, baby (Ricardo, Lee, and Erin too). Haig, "Wintz, you piece of shit" Atikianson. Bryan—thanks for all the fun shenanigans and board games, let's go on a whiskey spree. Toby—what a great partner in crime, thanks for spoofing that email and making Alex wet himself with the 'thx fc'. Best prank ever.

To Catherine, thank you for all your loving support in the early years. Another person I grew up with in many ways, thanks for teaching me things about myself and life.

To Kelly, thank you for your selfless support in the lead up to and during the lab transition. You're a great friend and person, and I always truly enjoy talking science with you.

To my best Boston friends, thank you. Pete, stop licking my face. Brady, thanks for the schticks and being a great roommate. Fine, fine, I admit it: you guys picked *me* up. Ugh. You guys welcomed me in to your circle and I'll always be

grateful for that. 'I'll be reading for the role of Taylor Ross.' Isabel, you're a useless lump of flesh, but you're *my* useless lump of flesh, thanks for being a great neighbor and friend. Caroline, thank you for always being great friend and repping east side Beacon Hill with me. Bailey, thanks for making me a part of your family—you guys are my Boston family.

To the table, I love you guys. I know you'll always have my back, no matter how many times Kenny punches someone, Chad takes his clothes off, or Camacho plays volleyball.

Andrew Perkins, my best friend. Boston isn't the same without you, and I miss you. You've been my lifelong partner in crime so far—I actually had to like, grow as a person when you left a couple years ago. It's been the worst. Sorry I got into board games and pool *after* you left. Love you man.

And finally, last but not least, to my parents. You guys have always been there for me—the safety net that lets me take risks without fear of failure. This work is dedicated to you.

Chapter 1

Outline

This thesis is divided into three main parts. The first part is an introductory portion, where I will discuss all the main topics contained in this thesis. I give a brief history of optics, describe why optics is important, and detail the motivation and vision behind this thesis work. The research performed here deals with wavefront control of surface plasmon polaritons, studied using near-field scanning optical microscopy. As such, introductory chapters on SPPs and NSOM are included. Finally, a brief history of metasurfaces and the guiding principles behind them are discussed.

The second part, and what I consider to be the bulk of the work contained herein, are Chapters 3 and 4. They describe a novel metalens for focusing SPPs and a platform for creating and steering surface plasmon wakes respectively. These works represent already published articles.

The final portion, Chapters 5 and 6 expand upon and use techniques discussed in the earlier chapters. Chapter 5 describes an extension of the work performed in Chapter 4, realizing a more complicated structure capable of introducing controlled anisotropies, which has just been accepted. Chapter 6 details an ongoing project in the lab designed to measure the refractive index of two-dimensional materials, currently in preparation/tying up loose ends.

Chapter 2

Introduction

Since the dawn of time, man hath sought to tame the sun.

2.1 Optics

Of the four fundamental forces, electromagnetism certainly provides the largest playground for laypeople and scientists alike. In fact, studying electrodynamics has proven throughout history to be a fantastic investment time and time again, allowing for massive technological strides in optics, circuits, and materials science—where many of the aforementioned strides contribute heavily to the everyday quality of life. As such, the goal of this section is to discuss the history of optics and its power, my motivations for studying optics, and how scientists

across the world use optics as both a subject of fundamental research and as a tool to advance other disciplines.

2.1.1 History

The history of optics has a fairly well-defined arc, and the known history starts with the ancient settlers of Anatolia. Their first mirrors date back almost 8000 years, created out of obsidian or large pools of still water (*1*). Next, the Egyptians and Mesopotamians discovered the first lenses and used copper polished mirrors, dating back to 750-500 BCE (*2*). Interestingly enough, the name lens comes from the Latin word for lentil, as double convex lenses are lentil-shaped. The oldest known lens is the 'Nimrud Lens', dating back 2700 years to ancient Assyria (*2*). These primitive lenses and mirrors already foreshadow humanity's acceptance of optics as a powerful tool for both everyday life and scientific investigations. At this point in time, the history of optics parallels the history of civilization, and the torch was passed to the Greeks. Geometric optics, stagnant for hundreds of years, found new life when geometry was discovered. The famous mathematician Euclid enumerated many fundamental properties of what is now known as Euclidean geometry (and even noted that light traveled in

straight lines!), laying the groundwork for early thinkers such as Ptolemy, who published a book on optics detailing reflection, refraction, and even tabulating refraction angles for several media (*3*, *4*). Over the next 1500 years or so, the pace of discovery was relatively stunted, however. Despite this, noteworthy discoveries include the first navigational compass (*5*) and Dietrich Frieberg's studies of primary and secondary rainbows (*6*).

Europe found itself in much turmoil during the Middle Ages, but surprisingly the arts and sciences flourished, earning the moniker 'The Renaissance'. Forced to flee Constantinople after its fall in 1453, hordes of Byzantine scholars immigrated to mainland Europe, bringing back many classical texts with them from the capitol city (*7*, *8*). This caused a resurgence in examining historical tomes and treatises, and the thinkers of the day began to question long held theories. At the center of this was Nicolaus Copernicus, who challenged Ptolemy's long held belief that the sun revolved around the Earth (*9*). In fact, this renewed interest in astronomy necessitated breakthroughs in optics as a means of observation and discovery. As such, the first telescope was created by

the Dutch optometrists Hans Lippershey and Zacharias Janssen in 1608, and in less than a year the news of their invention had reached Galileo Galilei—the first to point this discovery towards the heavens (*10*). This boon in astronomy attracted the famous German mathematician Johannes Kepler as well. Paramount to the scientific breakthroughs of this time was the subtle shift in the perception of astronomy as more 'pure mathematics' and less 'divine-oriented', which further enabled the 17th century thinkers to develop optics as a science (*11*). To this end Kepler, in a (single) yearly report to the emperor in 1603, detailed the inverse-square law for the intensity of light, described how the eye focuses light, discovered total internal reflection, was the first to use parallax to measure astronomical distances to heavenly bodies, mathematically described reflection by flat and curved mirrors, and detailed the use of a pinhole camera (*12, 13*). In 1657, Pierre de Fermat introduced the 'principle of least time', stating that light will always take the path that requires the least amount of time, in an insightful preview to Einstein's special and general relativity (*14*). The beginnings of wave-particle duality were already beginning to form as well: Francesco Maria Grimaldi discovered diffraction in 1665, and Christiaan

Huygen's developed his principle of wavefronts to describe refraction and diffraction of light rays (*15*). In the next century, Sir Isaac Newton and Benjamin Franklin had entered the fray, developing a particle theory of light and demonstrating that lightning was electricity, respectively (*16, 17*).

On the precipice of the 19th century, optics, on the whole, had been rather disjointed. Great advances had been made and many optical elements discovered, but an overarching, unifying theory was missing. Describing light as a wave tended to explain some theories (but not others), and Newton's 'corpuscular', particle-based theory was much of the same. Given Newton's status as a scientific giant, his particle-based theory was more widely accepted than Huygens' wavefronts—at least until the seminal experiments of the early 1800s. The most important of these experiments was performed by Thomas Young, demonstrating the principle of interference. Expanding on interference, two years later he performed the pivotal double-slit experiment. A decade later, Augustin-Jean Fresnel supplied more evidence to the wave nature of light theory with his experiments on diffraction, firmly supplanting Newton's corpuscular

theory (*18*). Electronics and circuits received much attention as well, and through contributions from Ohm, Faraday, and Ampere, James Clerk Maxwell found the final piece and solidified the set of four differential equations that have come to be known as Maxwell's Equations (*19*).

2.1.2 Motivation

Not on accident, the History of Optics section was truncated just at the advent of Maxwell's Equations, and the rationale can be summed up in a single quote:

'At the end of the day, it's all just Maxwell's Equations.'

The above quote was used as a pithy rebuttal to the criticism (at a conference talk), "This work has been done before!" And while seemingly glib, the deeper meaning illuminates the core of optics as a science: optics is defined by its building blocks and blueprints. Lenses, mirrors, detectors, lasers, etc., are the building blocks—combinations of which provide us with technologies such as cameras, LEDs, surgical tools, and telescopes. The blueprints—ideas and principles like near-field microscopy, interference, holography--provide

scientists and engineers ways to assemble and use the building blocks in novel ways. And so, the motivations and results of this thesis are humble and straightforward: create a building block or two and improve some existing blueprints. Because, at the end of the day, it's all just Maxwell's Equations.

2.1.3 Bringing optics to nanotechnology: nano-optics

Given the power of optics as an investigative tool for scientists of all fields and disciplines, it seems only prudent to apply the principles of optics to nanotechnology. The field of nano-optics, concerned with manipulating light at the nanoscale, is an inherently uphill battle. To wit, traditional optical components cannot fully harness the power of light at the nanoscale because of the diffraction limit. Still, techniques exist to concentrate and manipulate electromagnetic energy at subwavelength scales. The most notable of these (for the subject of this thesis) are: 1) the surface plasmon polariton (SPP), an electromagnetic, light-like mode involving a concentration of energy and oscillations of the free, plasma electrons in a metal and 2) near-field scanning

optical microscopy (NSOM), a microscopy technique utilizing nano-apertures and near-field principles to circumvent the diffraction limit.

2.2 Surface Plasmon Polaritons

2.2.1 History of Surface Waves

After the consolidation of Maxwell's Equations:

$$\nabla \cdot E = \rho/\epsilon_0$$

$$\nabla \cdot B = 0$$

$$\nabla \times E = -\partial B/\partial t$$

$$\nabla \times B = \mu_0\left(\frac{\partial E}{\partial t}\epsilon_0 + J\right)$$

it took roughly another 40 years for physicists to solve for the exact geometry that gives rise to Zenneck-Sommerfeld surface waves (*20, 21*). Discussed in Section 2.2.2, the main finding is that two semi-infinite half-spaces with opposite signed permittivities can support a surface wave at the interface. This wave propagates parallel to the interface and decays exponentially away from it. Initially discovered for radio waves propagating over the Earth's surface,

Zenneck and Sommerfeld's findings extend also to the visible portion of the frequency spectrum—the derivation makes no reference to the exact frequency needed, just the geometry and optical constants (*22*).

Nearly a full century after Maxwell, Pines and Bohm detailed the existence of the 'plasmon', a quantized oscillation of the free electrons in a metal, in order to explain the energy losses of fast electrons traveling through metal films (*23-25*). Several years later, RH Ritchie coined the term 'surface plasmon', extending the work of Pines and Bohm to the surfaces of metal films as well (*26*). This work brought the Zenneck-Sommerfeld radio waves on Earth to optical frequencies on metals.

In general, and for the purposes of this thesis, no distinction is made between a surface plasmon and a surface plasmon polariton. The full name of surface plasmon polariton only serves to highlight the light-like nature of the mode by affixing the name polariton. Fundamentally, the surface plasmon polariton is an

electromagnetic mode that exists at the interface of a metal and a dielectric. The SPPs have a well-defined frequency, modal dispersion, and can be thought of as a hybridization (in terms of electromagnetic energy) of the oscillation of free electron charges at the surface of a metal, and a light-like, oscillating electric field extending out into the dielectric, as shown in Figure 2-1.

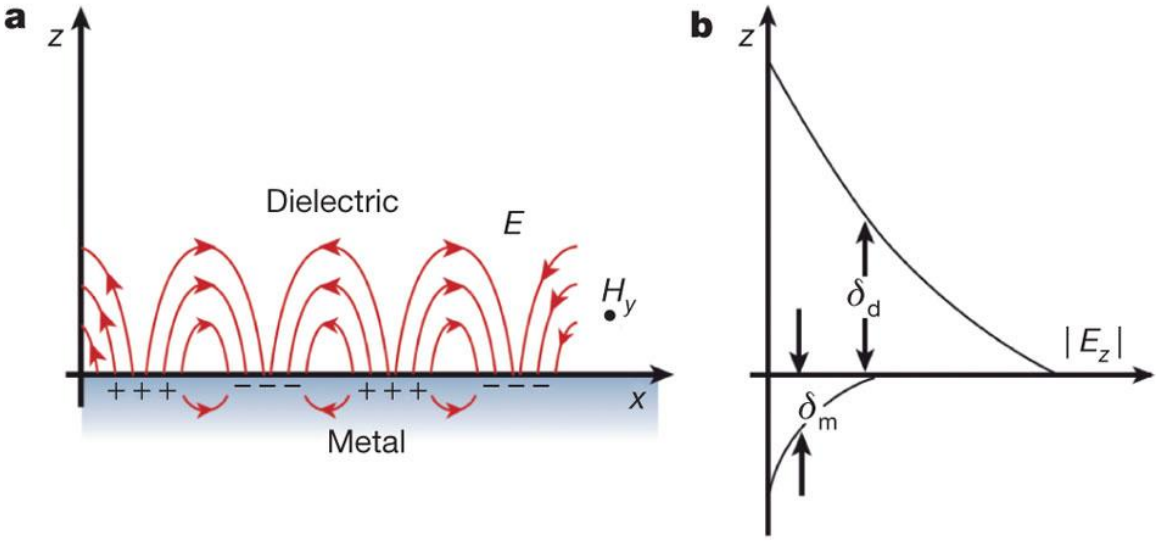

Figure 2-1. a) Geometry and electric field distribution of surface plasmon polaritons. b) Evanescent nature of the waves, decay lengths into the dielectric and metal (27).

2.2.2 Surface Plasmon Dispersion Derivation

2.2.2.1 Drude-Sommerfeld Model of Electrons

In deriving the dispersion relationship for surface plasmon polaritons, it is instructive to first begin with the Drude Model. First proposed in 1900 by Paul Drude (*28, 29*), the Drude model treats electrons as classical free charges in a sea of positive ions. Drude assumed a mean scattering time τ between purely elastic collisions, but makes no assumptions as to the origin of τ (the origin of collisions does not matter for the results of the model) (*30*). By stating that electrons, after an elastic collision, have roughly only a time τ to accelerate in an electric field E, he found that their momentum is: $< p > = qE\tau$. Using familiar relations for momentum, $< p > = m < v >$, and current density, $< J > = nq < v >$, a form of Ohm's Law can be derived:

$$\text{Equation 2-1.}\quad J = \left(\frac{nq^2\tau}{m}\right)E.$$

These ideas prompted Arnold Sommerfeld's analysis and development of the free electron model, where he combined Drude's model with Fermi-Dirac statistics (*31*). He noted that if an oscillating electric field is applied to the free

electron gas (plasma), the plasma would tend to move a distance x apart from the background of positive ions, developing a surface charge density, $\rho = -nex$ at either ends of the metal. The electric field in the sample is now, $E = nex/\epsilon_0$. Using the common expressions for the electric displacement $D(\omega)$ and the polarization density $P(\omega)$, and noting the oscillating electric field has the form: $E(\omega) = E_0 e^{-i\omega t}$, Sommerfeld found that the AC dielectric constant of the solid is:

$$\text{Equation 2-2.} \quad \epsilon_m(\omega) = 1 - \frac{ne^2}{\epsilon_0 m\omega^2}$$

where n is the electron density, e the magnitude of the electron charge, and m the mass of electrons. At the resonance frequency, denoted ω_p as the plasma frequency, the real part of the dielectric constant changes sign from negative to positive. This marks the regime where the metal stops behaving as a metal and begins to behave as a dielectric. At frequencies above the plasma frequency the free electrons simply don't have enough time (relative to the period of the incident electromagnetic field) to provide an adequate restorative force/electric field. Thus, the incident radiation is able to penetrate the material at frequencies above ω_p.

2.2.2.2 Derivation

Consider the geometry of Figure 2-1a, and let us search for TM modes that can exist, namely, modes that have a single magnetic component, H_y. The harmonic fields will have a time component of $e^{-i\omega t}$ that will be omitted in the following for clarity, except where specified. Thus, we begin with the following magnetic field:

$$\text{Equation 2-3. } H_y = H_0 e^{ik_{x,i}x \pm ik_{z,i}z}.$$

where H_0 is the incident field strength, $k_{x,i}$ is the wavevector in the x-direction in the i^{th} medium (dielectric or metal), and $k_{z,i}$ is the wavevector in the z-direction. The wavevectors can be complex, where the imaginary component is tied to absorption, dissipation, or loss. Using Ampere's Law with $J = 0$, the electric field can be computed using the following relation:

$$\text{Equation 2-4. } E = \frac{\nabla \times H}{-i\omega\epsilon(\omega)}$$

which will give E_x and E_z components, and $\epsilon(\omega)$ refers to the frequency dependent dielectric constant of the medium in question. Using the Maxwell's boundary conditions of 1) $D_\perp$ continuous and 2) $E_{||}$ continuous ($H_{||}$ gives the

same information) on our H_y, E_x, and E_z fields we find that 1) $\epsilon_m E_{zm} = \epsilon_d E_{zd}$ and 2) $E_{xm} = E_{xd}$, $k_{xm} = k_{xd}$. Using this information we can find that the following equation must be satisfied for these TM modes to exist:

Equation 2-5. $\frac{k_{zd}}{\epsilon_d} + \frac{k_{zm}}{\epsilon_m} = 0.$

Equation 2-5 demonstrates why the surface plasmon polariton mode can only exist at the interface of a metal and dielectric. In order for the equation to have any solutions, the dielectric constants must differ in sign—one positive, one negative. In conjunction with the wave equation $\left(k_x^2 + k_z^2 = \frac{\epsilon \omega^2}{c^2}\right)$, the dispersion relationship for surface plasmon polaritons is:

Equation 2-6. $k_x = \frac{\omega}{c}\sqrt{\frac{\epsilon_m \epsilon_d}{\epsilon_m + \epsilon_d}}.$

Analysis of this equation establishes that a mode can exist ($Re(k_x) \neq 0$) if $\epsilon_m < 0$ and $|Re(\epsilon_m)| > \epsilon_d$. A consequence of this is that both of the transverse wavevector components, k_z, are imaginary. This property describes the evanescent field that extends away from the interface and into both the dielectric

and the metal. After substituting ϵ_m from Equation 2-2. $\epsilon_m(\omega) = 1 - \frac{ne^2}{\epsilon_0 m\omega^2}$ into Equation 2-6, the dispersion relationship of SPPs can be plotted (Figure 2-2).

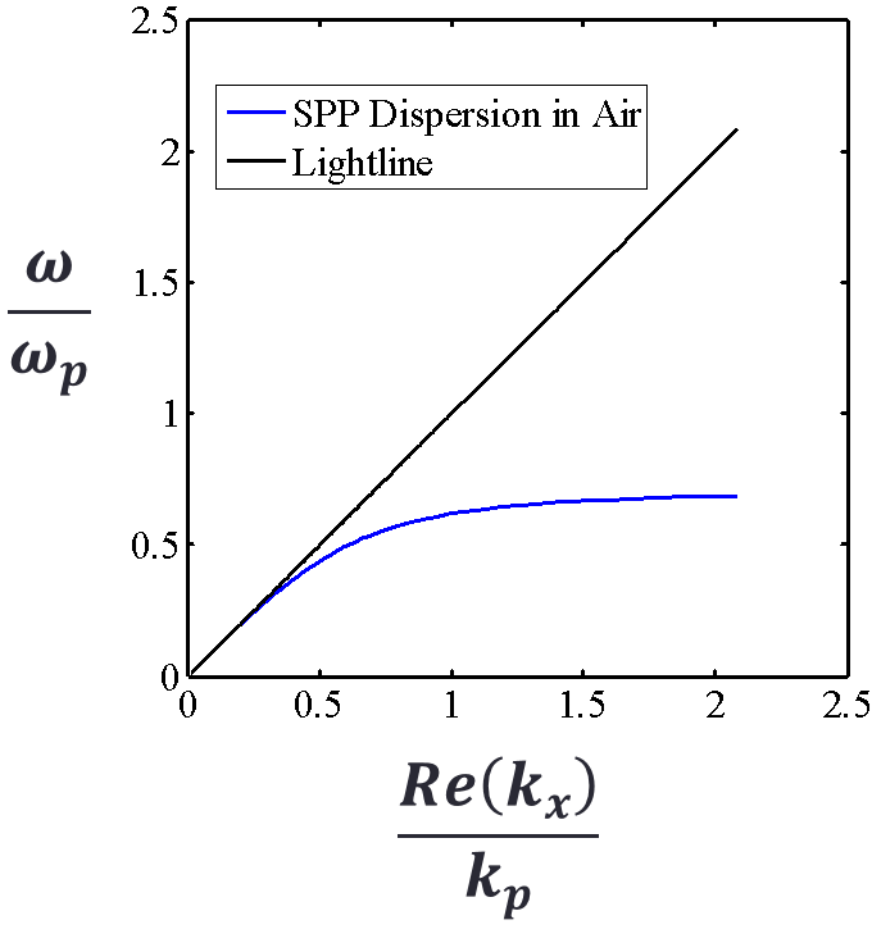

Figure 2-2. SPP dispersion at a gold/air interface. Values for ω_p and τ taken from Jackson's Classical Electrodynamics (*19*). Wavelength range of 200 nm to 10 μm.

It is important to note that, given the SPP dispersion relationship, SPPs are non-radiative 'dark' modes. This can be seen from Figure 2-2, where the SPP dispersion lies to the right of the light-line, at higher k values. This also necessitates special techniques for exciting surface plasmons, as $k_{SPP} > k_0$, for all frequencies. Luckily, many techniques exist to overcome this wavevector mismatch, discussed in Section 2.2.3.

2.2.3 Techniques for Exciting Surface Plasmons

The oldest forms of exciting surface plasmons are known as the Kretschmann-Raether and Otto configurations (*32, 33*). The key point of these techniques is the use of a prism (most commonly glass), where the wavevector inside the prism is given by $k_n = nk_0$, where n is the refractive index of the prism and k_0 is the free space wavevector. Thus, the magnitude of the wavevector can be increased by a factor of the refractive index, and under suitable conditions, can overcome the wavevector mismatch and excite surface plasmons at a metal/air interface.

The experimental geometry of the Kretschmann configuration is shown in Figure 2-3. Incident light (p-polarized) encounters the glass prism and refracts (not depicted). This refracted light has an increased wavevector, and reflects off the metal at the metal/glass interface. A fraction of this light undergoes frustrated total internal reflection (analogous to quantum tunneling for particles, if the electromagnetic field is considered the wavefunction of the photon), or evanescent mode coupling (as the modes overlap spatially), and couples into the SPP mode at the metal/air interface. This occurs when the parallel wavevector in the glass prism satisfies the relation: $k_{||} = k_{||,SPP}$.

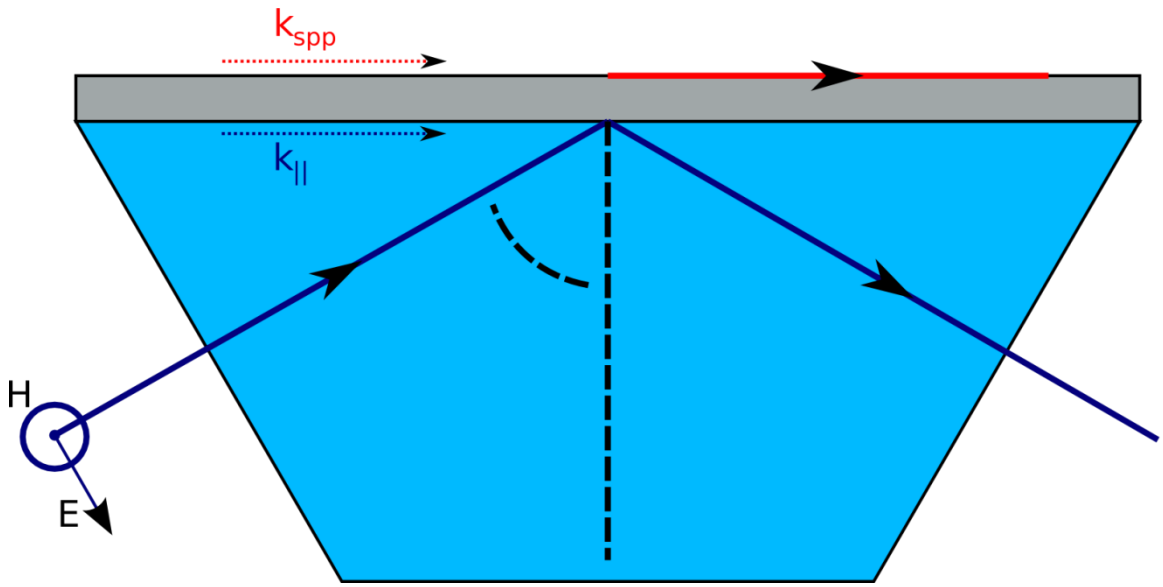

Figure 2-3. Kretschmann-Raether geometry (*34*). The glass prism (blue) provides the wavevector kick to couple into SPPs at the metal/air interface at the top of the structure via evanescent mode coupling.

Another common technique for exciting SPPs uses a grating to couple energy in to SPP modes. As before, any excitation method for SPPs must provide a wavevector kick to overcome the momentum mismatch between the free space modes and the SPP modes. With gratings, this is provided by a multiple of the grating vector, where the wavevector of the light after interaction with the grating is given by: $k = k_0 + 2\pi/a$ where a is the grating pitch, as shown in Figure 2-4.

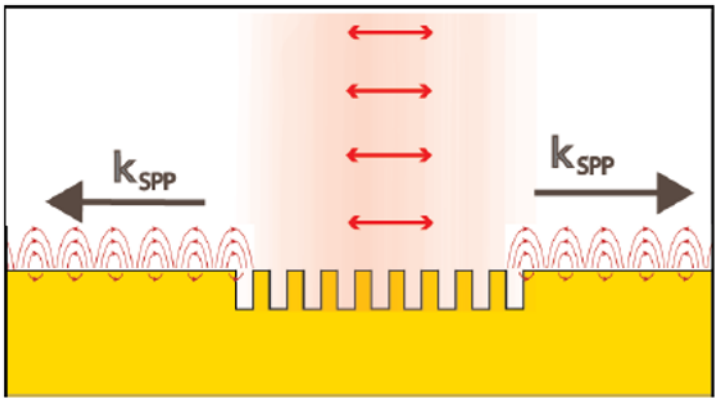

Figure 2-4. Diffraction grating coupler configuration. Light polarized perpendicular to the grating receives a wavevector kick and can couple into SPP modes (Figure credit: poster by JPB Mueller).

SPPs can also be launched from a long slit etched into a metal film. Incident light polarized perpendicular to the slit, as depicted in Figure 2-5a, induces a charge oscillation along the slit that oscillates with the same frequency as the incident light. This oscillation is the launched SPP waves which propagate with a wavevector perpendicular to the slit.

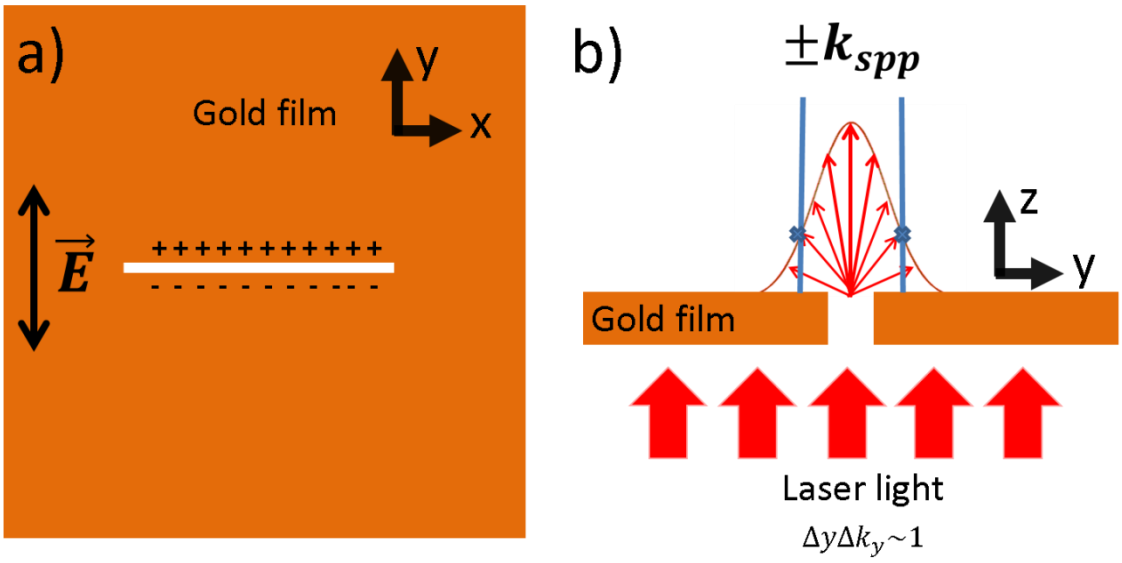

Figure 2-5. Long slit as a plane wave coupler of SPPs. a) Light polarized perpendicular to a slit induces a charge oscillation in the vicinity of the slit, launching SPP waves. b) The wavevector kick is provided by diffraction, where some of the diffracted light can couple into SPP modes.

The mechanism of coupling is similar to the grating coupler depicted in Figure 2-4. Light confined to a small lateral dimension Δy will undergo diffraction and experience a spread in wavevectors according to: $\Delta y \Delta k_y \sim 1$. This is the mechanism providing the wavevector kick. A fraction of these new wavevectors will satisfy the relationship: $k_{||} = k_{SPP}$ and can couple into the SPP mode. As the

slit is long compared to the surface plasmon wavelength, SPP plane waves will be emitted from the slit (*35*).

The last excitation method discussed here is the nanoslit, which acts as a dipole source for SPPs. A schematic is presented in Figure 2-6.

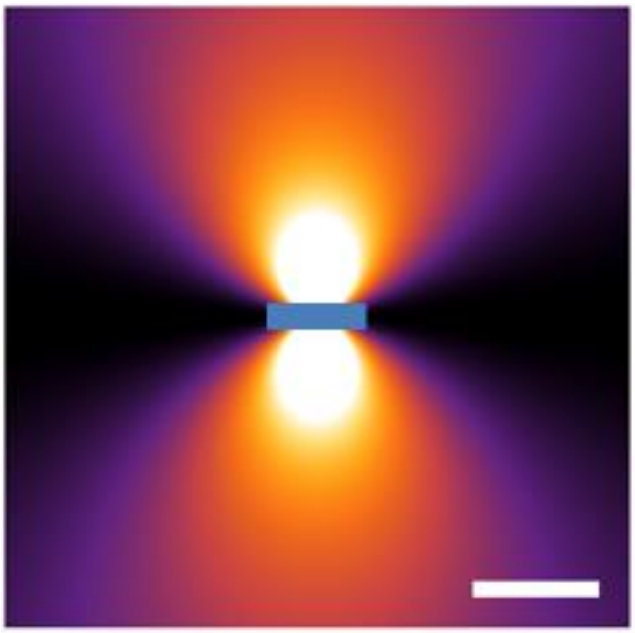

Figure 2-6. Nanoslit as an SPP dipole source. Nanoslit (blue rectangle) emission pattern when light polarized perpendicular to the slit impinges on the slit. Note the dipolar $\cos^2\theta$ emission pattern. Scale bar: λ_{SPP}.

The method of excitation is the same as discussed in Figure 2-5, but as the slit is subwavelength in length, the nanoslit emits in a dipolar fashion. A unique

difference between the SPP dipole and an electric dipole radiating in free space is the polarization—SPPs are TM waves, so the dipole moment is parallel to the wavevector of the SPPs instead of perpendicular like radiating free space electric dipole.

2.2.4 Surface Plasmon Properties and Applications

The first applications of SPPs were to measure the optical properties of the noble metals by Kretschmann (*36*). He had the misfortune of: 1) needing to measure three unknowns (real and imaginary dielectric constant *and* thickness of the < 100 *nm* film) and 2) being completely overshadowed by Johnson and Christy's seminal data some six months later, in 1972 (*37*). As we will see in Chapter 6, measuring refractive indices can be quite challenging.

However, today the most commercialized and successful application of surface plasmons is known as surface plasmon resonance, or 'SPR' in biology and chemistry communities. SPR is used to detect minute changes in refractive index, mostly as a check to validate if a chemical reaction has occurred.

Heuristically, this is done by placing a molecule on the metal surface, introducing possible reactants then analyzing whether the dielectric environment of the SPPs has been altered. We note that the term resonance in SPR is a misnomer, as surface plasmon modes are not a resonance, but a mode with dispersion. The nomenclature is not without merit, however, and comes from the apparent resonant coupling, evidenced by the reflectivity dip seen in the Kretschmann configuration (Figure 2-3). The 'resonance' occurs when the incident light couples into the SPP mode instead of reflecting off the metal surface Figure 2-7.

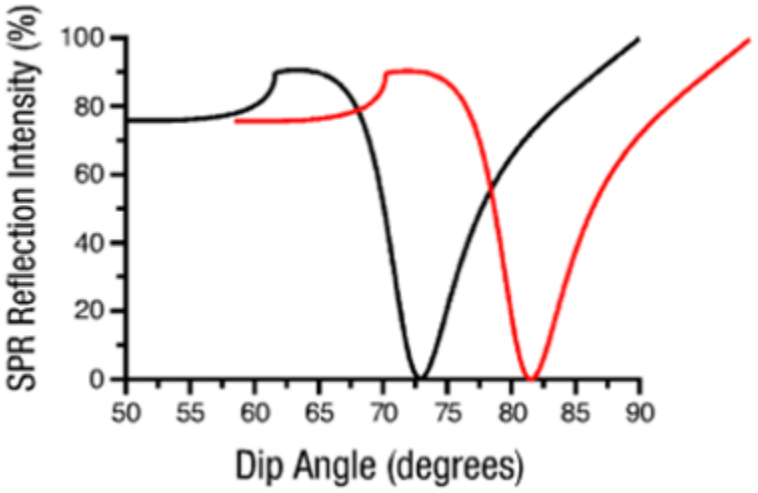

Figure 2-7. Surface plasmon resonance reflectivity dip. Reflection as a function of angle of incidence for a given wavelength in the Kretschmann configuration of

Figure 2-3. The position of the dip is determined by the frequency and wavelength of the incident light, angle of incidence, the refractive index of the metal, the dielectric above the metal, and the refractive index of the prism used. By holding other factors constant, a change in refractive index of the dielectric above the metal can be inferred from displacement of the dip. (*38*)

Many of the other applications of SPPs are sensing based, including: nanoparticle sensors with zeptomole sensitivity, optical fiber sensors, and surface enhanced Raman spectroscopy (SERS) (*39-41*).

For the purposes of this thesis, the main advantage of surface plasmon polaritons is their ability to confine electromagnetic energy into two dimensions rather than three. This has the advantage that planar structures are easier to work with and fabricate, particularly if any plasmonic effect is to be used in circuitry. An added benefit is that surface plasmons confine the electromagnetic energy to subwavelength scales as well. These advantages come at a high cost—a significant portion of the modal volume resides in the metal, where Ohmic losses cause dissipation, loss of energy, and lower efficiency. In addition, surface plasmons are non-radiative modes and require special detection schemes. In the

next section, we detail the use of near-field scanning optical microscopy as a means to detect and measure the surface plasmon polariton fields.

2.3 Near-field scanning optical microscopy

Near-field scanning optical microscopy belongs to the family of various scanning probe technologies, the most popular of which is atomic force microscopy (AFM), used to measure the morphology of samples. NSOM is an evolution of the AFM technique, adding an optical component. As will be discussed in more detail later in this chapter, the motivation for using NSOM is simple: electromagnetic near-field to far-field propagation results in the loss of information. This loss of information comes from low spatial frequency bandwidth—i.e., propagation acts a low pass filter for spatial frequencies. In this vein, we first turn to a discussion of Fourier analysis, resolution limits, and spectral decompositions.

2.3.1 Plane Waves and the Diffraction Limit

From Maxwell's Equations, detailed in Section 2.2.1, the electromagnetic wave equations for E and B can be derived by taking a cross product and using vector identities, (shown for E):

$$\text{Equation 2-7. } \frac{1}{c^2}\frac{\partial^2 E}{\partial t^2} - \nabla^2 E = 0.$$

Through Fourier analysis, every real electromagnetic wave can be decomposed into a set of frequencies and spatial frequencies. Using separation of variables, we write the solutions of Equation 2-7 with a time component of: $e^{-i\omega t}$, and a spatial frequency component in the form e^{ikx}, where ω denotes the frequency and k denotes the spatial frequency. Real values of k denote plane waves, and imaginary values of k denote evanescent waves. We note a small distinction—true plane waves, with a perfectly defined k, require infinite extent in space and thus cannot exist. However, in most practical applications, this approximation is valid.

The resolving power of any system is limited by the collection of these wavevectors, the plane waves and evanescent waves. Fourier mathematics leads us to: $\Delta x \Delta k_x \geq 1$, where the product is minimized for Gaussian distributions of Δx and Δk_x. The physical interpretation/reason for this is that the quantum mechanical operators for x and p ($p = \hbar k$) do not commute. For far field optics, the largest amount of wavevectors, or largest spread in k that can be collected is twice the magnitude of the wavevector in the medium, $2k = 4\pi/n\lambda_0$, corresponding to all the wavevectors from $-k$ to k. The associated minimum spread in distance is now given by:

Equation 2-8. $\Delta x = \frac{\lambda_0}{4\pi n}$.

which is the absolute best case. In real experiments, limited by the numerical aperture of the system, n can be replaced by the numerical aperture: $NA = nsin\,\theta$, which is always less than or equal to n by virtue of the range of the sine function. These concepts form the basis of the diffraction limit for conventional microscopes. At this point, it is useful to talk about the angular spectrum representation to discuss more about the collection of wavevectors (*19, 42*).

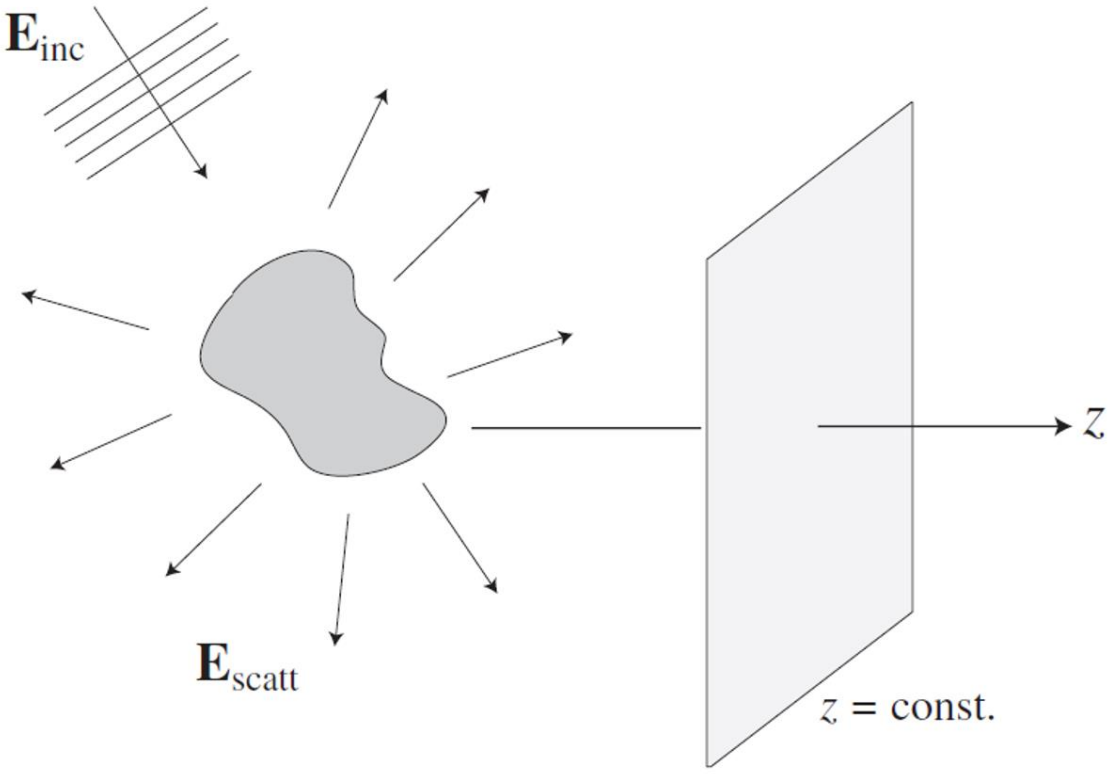

Figure 2-8. Scattering problem highlighting the angular spectrum representation. Electric fields are evaluated in a plane perpendicular to some arbitrarily chosen z-axis (*42*).

From Figure 2-8, if the electric field is known at some $z = 0$ value, the field along the z-axis is given by:

Equation 2-9.

$$E(x,y,z) = \iint_{-\infty}^{\infty} \hat{E}(k_x,k_y,0)e^{i[k_x x + k_y y \pm k_z z]}dk_x dk_y.$$

While seemingly cumbersome, the intuition is relatively straightforward. If we know the electric field in the plane $z = 0$, we can also know the spatial frequencies k_x and k_y by taking the Fourier transform. Thus, reconstructing the electric field at some arbitrary z is simply a matter of integrating over all the spatial frequencies and 'propagating forward' the field to the new z plane. In other words, finding the electric field at the new point (x, y, z) amounts to calculating which of the points in $(x, y, 0)$ have spatial frequencies that can propagate to and contribute to the field at (x, y, z), and then integrating over all of the points and wavevectors that contribute to find the final value.

Detecting and collecting all of the k vectors associated with the electric field at $(x, y, 0)$ is another matter entirely. In fact, as can readily be seen by the limits of integration of Equation 2-9, many of these k vectors are evanescent waves, satisfying: $k_x^2 + k_y^2 > k^2$, leaving a purely imaginary k_z. The waves associated with these spatial frequencies decay exponentially away from the z-axis. Mathematically, these wavevectors are needed information for accurate image reconstruction. However, for the purposes of conventional far-field optics, these

evanescent wavevectors are lost information—perfect resolution of an image is impossible without collecting *all* of the wavevectors associated with scattering from the object.

While the idea of simply performing measurements in the near-field to collect the evanescent wavevectors seems intuitive, in practice it is quite difficult. This is evidenced by the fact that this idea was first proposed in 1928 by Edward Synge (*43*), but only carried out at optical frequencies by Betzig and Lewis *et al*. in 1986 (*44*).

2.3.2 Functional Details of NSOM

2.3.2.1 Introduction

While the motivation is clear, the working details of NSOM are immensely complicated, many of which are beyond the scope of this thesis. In this sub-section, I will briefly discuss other types of NSOM, with a later section on the

details of the Nanonics collection mode, bent fiber NSOM used for all of the work to date in the Capasso group.

Atomic force microscopy use typically involves a cantilever or tuning fork, with a feedback loop to control the probe-sample distance. In general, the system measures changes in the frequency of a mechanical oscillation as the probe scans over a sample. When the sample interacts with the probe, the system senses this interaction and adjusts the height accordingly. For the purposes of this thesis, it suffices to describe the phenomenon as 'electromagnetic friction'. This force is van der Waals in nature between the tip and sample. This implies that the interaction can change from tip, tip dimensions, and sample—complicating measurements. Thermal fluctuations cause local orientations of the electric dipoles in both the tip and the sample, and if they are in close enough proximity, these dipoles and their image dipoles interact via their electric fields and can become correlated. Once correlated, and tiny electric fields exist between the dipoles of the tip and sample, any fluctuation causes a re-orientation of these dipoles (van der Waals force). Work is done to reorient the dipoles, dissipating

energy via Ohmic losses (*45*). Operationally, this electrostatic interaction changes the oscillation frequency of the tip, and this change is measured by the feedback loop and corrected.

2.3.2.2 Tuning Forks, Tips, and Bent Fibers

Turning AFM into NSOM simply requires adding a method of optical detection. The two main categories of NSOM are aperture and aperture-less NSOM. Aperture-less NSOM uses a metallic AFM tip to scatter light close to the sample, which is then detected. Apertured NSOM, which was the method used for this thesis work, relies on mounting a tapered optical fiber to a tuning fork, which collects light from the near-field of the sample for detection.

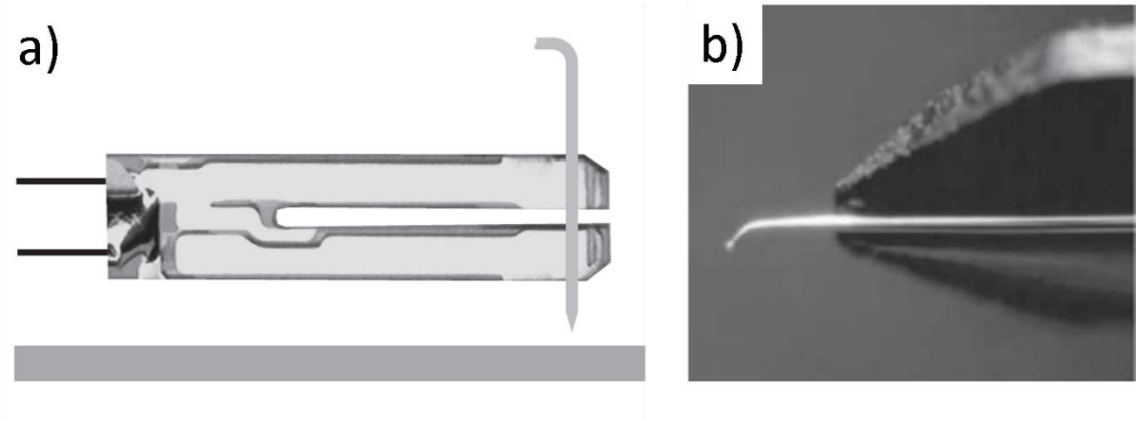

Figure 2-9. a) AFM tuning fork with optical fiber attached, sample below. b) Cantilever example with a bent fiber, similar to the probes used during this thesis from Nanonics Ltd (*42*).

The tapered optical fibers are mounted onto an AFM tuning fork using an epoxy. Tapered fibers can be created by heating and pulling, or by chemical etching (*46, 47*). For all of the work in this thesis, the fibers are then coated with various metals to reduce aperture size, as shown in Figure 2-10.

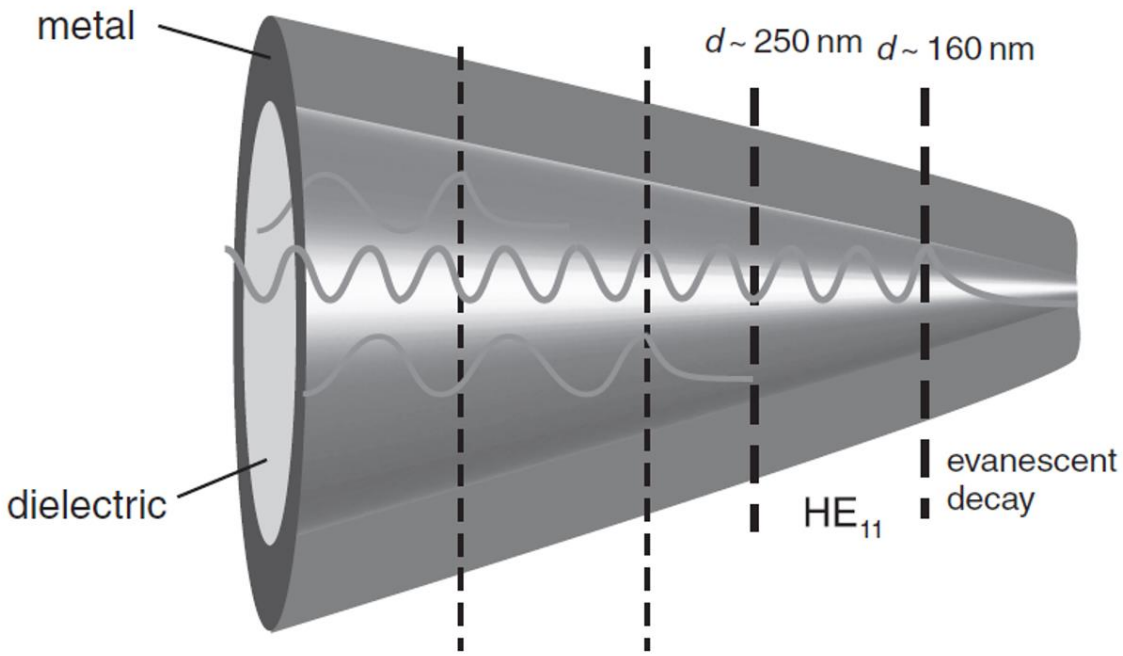

Figure 2-10. Metal coated tapered optical fiber tips. Propagation and decay of modes is shown (*48*).

Some NSOM experiments utilize the tip as a source, coupling light into one end of the fiber and delivering the light to the sample via the tapered fiber tip. The tapering of the fiber down to a diameter of ~50 nm serves the purpose of localizing the light spatially, allowing the tip to act as a dipole source with a wide range of wavevectors according to the equation: $\Delta x \Delta k \sim 1$. The localization of the light from the tapered fiber (acting as a high pass filter) is illustrated by the modes in Figure 2-10. For our purposes however, we operate in collection mode (illuminating the sample externally and collecting light with the tip). Consequently, time reversal symmetry implies that small tips can also serve to collect the high wavevector components from external evanescent waves.

In summary, all of the NSOM experiments contained in this thesis are performed with an AFM tuning fork (tapping mode) with a tapered optical fiber attached (collection mode NSOM). The tip of this fiber has a diameter of roughly 50 nm. The tip is brought into close proximity of the sample, such that it can interact

with the near-field. Detection occurs when the energy is scattered out of the SPP mode, and into a propagating mode in the optical fiber. The other end of the fiber is connected to an avalanche photodiode or a spectrometer, depending on the measurement.

2.4 Metamaterials and Metasurfaces

Metamaterials were first used/discovered post World War II as a means to artificially control microwaves (*49*). Over time, blueprints such as photonic crystals, cloaking devices, negative index of refraction materials, and superlenses have been created (*50-52*). In short, the idea of artificially patterning materials has led to some quite exotic building blocks for science, and in particular, optics.

2.4.1 Metasurfaces

In 2011, Yu *et al*. demonstrated a generalized version of reflection and refraction (*53*). This was achieved by patterning a single surface with an array of subwavelength gold antennas. The basic principle is the following: each antenna is suitably designed such that the array of such antennas provides a linear phase gradient to the surface—altering the centuries old law of refraction:

Equation 2-10. $n_1 \sin\theta_1 + \frac{1}{k_0}\frac{\partial\phi}{\partial x} = n_2 \sin\theta_2$

where n_i refers to the index of refraction of the i^{th} medium, θ_i refers to the angle of propagation relative to the normal in the i^{th} medium, k_0 is the free space wavelength, and the $\partial\phi/\partial x$ term is the linear phase gradient provided by the metasurface itself.

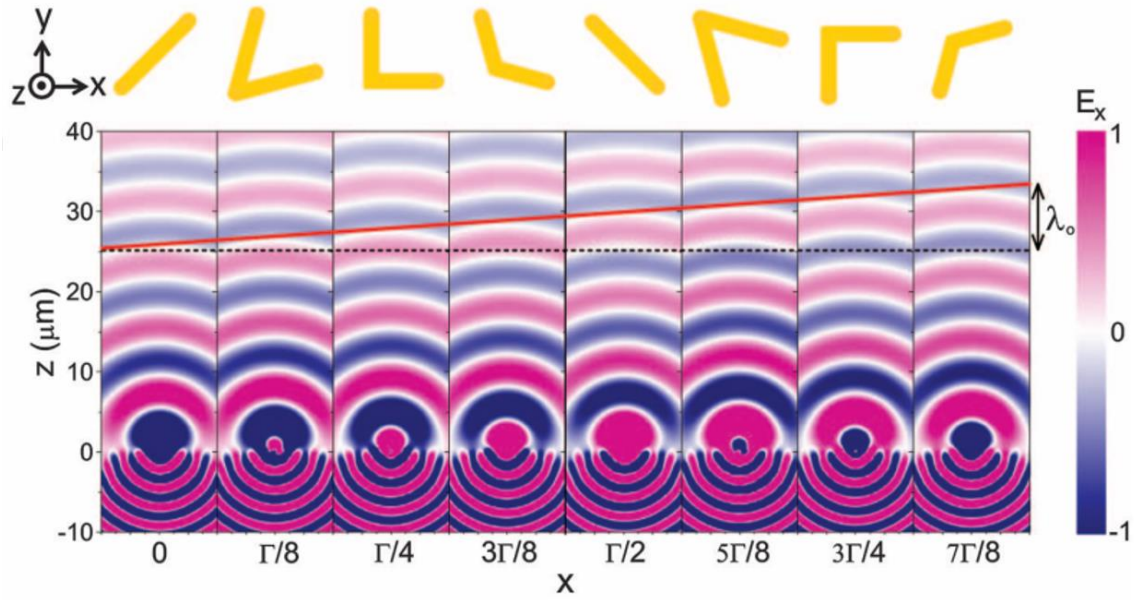

Figure 2-11. Linear phase gradient by a metasurface. (Top) The geometries of gold antennas to impart the correct phase. (Bottom) FDTD simulations for each antenna, stitched together to highlight the deflection (red solid line) imparted by the metasurface (*53*).

The effect has been an explosion of activity in the field—after all, most optical elements are defined by their phase profile, and now phase can be altered seemingly at will with a single step of lithography patterning.

This methodology is known in the microwave and radiowave communities as the phased array (*54, 55*). Thus, while the concept itself is not necessarily novel (it's all just Maxwell's equations anyway), the development and vision of bringing phased arrays to the optical regime *is* new. The staggering amount of research into metasurfaces over the past five years is a testament to this fact. In reality, the story arc of metasurfaces over the past five years is reminiscent of the Wild Wild West. Groups all over the world have raced to develop lithography techniques, discover new constitutive phase elements, and design exotic optical phase profiles with said elements. The field has rapidly progressed—starting from lossy elements in the mid-IR all the way to dielectric elements in the visible (*53, 56*).

This ends the introduction section, detailing the power of optics, the pros, cons, and manipulation of surface plasmons, the need for near-field scanning optical microscopy, and a brief introduction to metasurfaces. The remainder of the thesis presents experimental works performed with these themes in mind.

Chapter 3

Holographic Metalens for Tunable Focusing of Surface Plasmons

ABSTRACT

Surface plasmons polaritons (SPPs) are light-like waves confined to the interface between a metal and a dielectric. Excitation and control of these modes requires components such as couplers and lenses. We present the design of a new lens based on holographic principles. The key feature is the ability to switchably control SPP focusing by changing either the incident wavelength or polarization. Using phase-sensitive near-field imaging of the surface plasmon

wavefronts, we have observed their switchable focusing and steering as the wavelength or polarization is changed.

3.1 Introduction

Surface plasmon polaritons (SPPs) are electromagnetic surface waves confined to propagate at the interface of a metal and a dielectric, involving both a charge oscillation of free electrons in the metal and an evanescent electric field extending into the dielectric(*57*). SPPs have garnered attention for decades now, affording the possibility to control light at the nanoscale, transfer information on subwavelength scales, and other novel optical techniques(*58-60*). Coupling into SPP modes can be accomplished by simple experimental configurations, typically by using prism geometries or diffractive gratings. In addition, the development of high resolution lithography and milling techniques allows for the design of structures that can be integrated into complex optoelectronic circuits whose functionality is based on the processing of SPPs. Recently developed nanostructured surfaces (metasurfaces) that control the amplitude, phase, and polarization of propagating light or SPPs, are particularly suited for

wavefront engineering(*53, 61-64*). Metasurfaces based on plasmonics have already been used to implement flat lenses that work in transmission(*65-68*) or in reflection(*69, 70*) with reduced aberrations(*71, 72*). On the metal-dielectric interface, wavelength selective focusing(*73, 74*) and unidirectional coupling to plane waves(*75*) has also been shown by means of plasmonic couplers made of nanoslits. Nanoholes and nanoslits are among the most commonly used unit elements when designing metasurfaces for SPP manipulation(*76-79*).

3.2 Metalens Design Principle

Here, we demonstrate a metalens design strategy based on holographic principles. The metalens has the ability to steer SPPs between several foci on the surface based on the incident wavelength and has on/off switchability based on the incident polarization. Our design is straightforward and consists of placing non-resonant nanoslits (50 nm wide, 200 nm long) along the contours defined by the wavefront of SPPs propagating out from an imaginary emitter placed at the location on the surface where we want SPP focusing. The imaginary point source is treated as a Huygens' emitter that can be described by a simple 2D

circular wave: $\vec{E} \propto e^{ik_{SPP} \cdot r}$, where k_{SPP} is the wavevector of the SPP at gold/air interface and r is the distance from the imaginary source point (Figure 3-1). Since the nanoslits lie on the equiphase lines (wavefront of the SPPs), if the nanoslits are excited in phase, then the re-radiated SPPs will constructively interfere at the position of the original imaginary emitter. Since we want to have multiple foci (for tunability purposes), adding another focus requires the nanoslits to be placed not just on the equiphase lines of one imaginary emitter, but on the equiphase points resulting from the intersections of the wavefronts of all the imaginary point sources (Figure 3-1). In our device, a different source point for each free space wavelength ($632, 670, 710,$ and $750\ nm$) is chosen such that light at each wavelength couples to SPPs via the nanoslits and is focused to the four corners of a 16 μm x 16 μm square. Within each of Figure 3-1a and Figure 3-1b, the mutual wavefront intersections are denoted by the black dots, which are the positions where we mill nanoslits in the gold film.

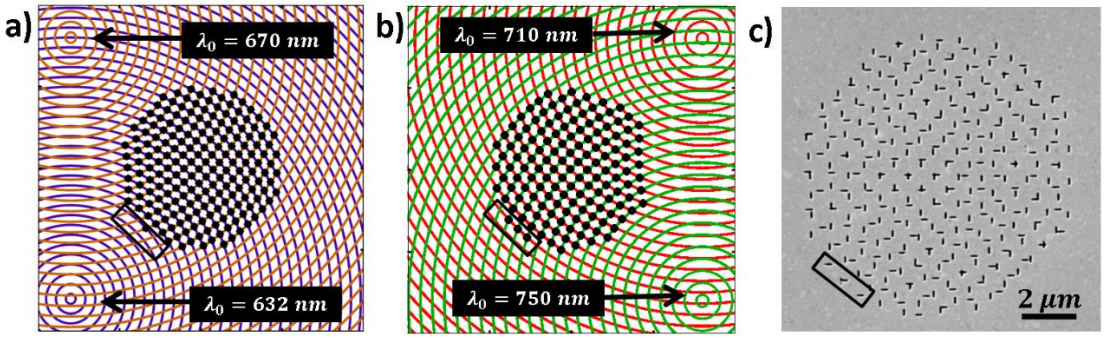

Figure 3-1. Metalens design. a) Focal points for illuminating light wavelengths $\lambda_0 = 632, 670\ nm$ in the bottom and top left corners, respectively. Purple circles denote the wavefronts of an imaginary circular point source located in the bottom left corner, for $\lambda_0 = 632\ nm$ ($\lambda_{SPP} = 604\ nm$). Orange circles denote the wavefront for $\lambda_0 = 670\ nm$ imaginary source in the top left corner. Black dots denote the intersections of the two wavefronts (within a 5 μm radius), which is where vertical nanoslits are milled. Vertical nanoslits couple light into surface plasmon polaritons preferentially when excited with normally incident horizontally polarized light. Thus, if the vertical apertures are illuminated with the latter at $\lambda_0 = 632$ or $670\ nm$ light, all of the scattered surface plasmons that reach the respective focal point (on the left side) will be in phase, since by design they lie on the equiphase lines. b) Equivalent of a), but for the other two wavelengths ($\lambda_0 = 710$ and $750\ nm$), which will be focused to the remaining corners of the 16 μm × 16 μm square. Black circles in b) denote where horizontal nanoslits are milled. There are fewer intersection (equiphase) points because the wavelengths are longer. c) Scanning electron micrograph of our device after the nanoslits are etched into the gold film by focused ion beam. Even though some of the nanoslits overlap, this does not appreciably affect the performance of the device. The black box is shown for reference and denotes the same physical space in all panels.

Interestingly, our approach is a special case of a more general design principle based on holography(*80-82*), which has been extended for use with surface plasmons(*83-92*). In general, holography involves recording the interference pattern between a suitably chosen reference wave and the light scattered by an object into a photo-sensitive material. Both intensity and phase information of the object's scattered wavefront can be retrieved by illuminating the recorded interference pattern with the reference beam. In regards to our device, the equiphase lines (on which the nanoslits are placed) are equivalent to the lines of constructive interference between a flat wavefront (e.g. a normally incident plane wave) and a circular point source, where the flat wavefront assumes the holographic role of the suitably chosen reference wave and the SPP from the imaginary point source assumes the role of the light scattered by an object. It is worth noting here that an iterative algorithm is not needed(*73, 93*)—most holographic approaches utilize such algorithms to maximize the constructive interference between antennas. Moreover, as these algorithms only aim to maximize the intensity at a specific position, they do not necessarily result in a propagating beam of light, producing intense hot-spots instead. Furthermore,

our approach allows us to choose the phase of the SPPs at the focus (relative to the incident beam), since the initial choice of point source phase is arbitrary. This can be important if a specific phase is needed, for instance, to couple the SPPs to a specific plasmonic waveguide mode or other components of a more complex circuit located at the focal positions.

3.3 Origin of Polarization On/Off Switching

Another central point of our design is to use nanoslits instead of nanoholes for coupling light to SPPs. Light passing through a nanoaperture diffracts, giving rise to a large spread of wavevectors that allows coupling into SPP modes. A nanoslit that is subwavelength predominantly in one direction re-radiates SPPs preferentially when the incident light is polarized normal to the slit. Far from the nanoslit (several hundred nanometers), the SPP intensity has a simple dipole-like distribution. Nanoholes can couple free space light to SPPs, but they do so without polarization selectivity. Employing nanoslits adds polarization selectivity since light polarized perpendicular to the nanoslit couples preferentially. Horizontal nanoslits are excited by vertically polarized light and

vice versa, which forms the basis for the polarization on/off selectivity and polarization tunable coupling of the metalens. Each orientation (horizontal or vertical) of nanoslits in the device has two operating free space wavelengths—vertical slits couple to $\lambda_0 = 632$ and $\lambda_0 = 670\ nm$, horizontal slits couple to $\lambda_0 = 710$ and $\lambda_0 = 750\ nm$. Wavelength tunable directionality is based on the following: for a set of slits, if one of the operating wavelengths with the correct polarization is incident on the device, the only location where all of the SPPs constructively interfere is the original imaginary source point—nowhere else will all of the SPPs constructively interfere. These slits are shown in the scanning electron micrograph (SEM) of Figure 3-1c.

3.4 Fabrication and Experimental Setup

To fabricate our device, we e-beam evaporate a 50 *nm* film of gold onto a polished silicon wafer and template strip(*94*) it onto a glass slide for decreased surface roughness. Then, after following the design depicted in Figure 3-1, we use focused ion beam (FIB) milling to etch the nanoslits into the gold film Figure 3-1c. The sample is illuminated from below with linearly polarized light (Figure

3-2). The illuminating beam is at normal incidence and focused (beam waist of $\sim 10\ \mu m$) on the metalens. The incident light is emitted from a super continuum laser with a wavelength range in the band $400 - 850\ nm$. This laser excites the nanoslits causing SPP emission while the probe of a near-field scanning optical microscope (NSOM) scans an area of the surface that includes the metalens and the focal points. Our NSOM (Nanonics Imaging Multiview) probe is a metal-coated, tapered optical fiber with a subwavelength aperture at the facet. The NSOM probe interacts with the evanescent field of the SPPs close to the metal/air interface that are then coupled into propagating modes in the optical fiber (collection mode NSOM). The other end of the fiber is connected to a single photon avalanche photodiode (SPAD) or a spectrometer. Figure 3-2a presents a full schematic of the experimental setup.

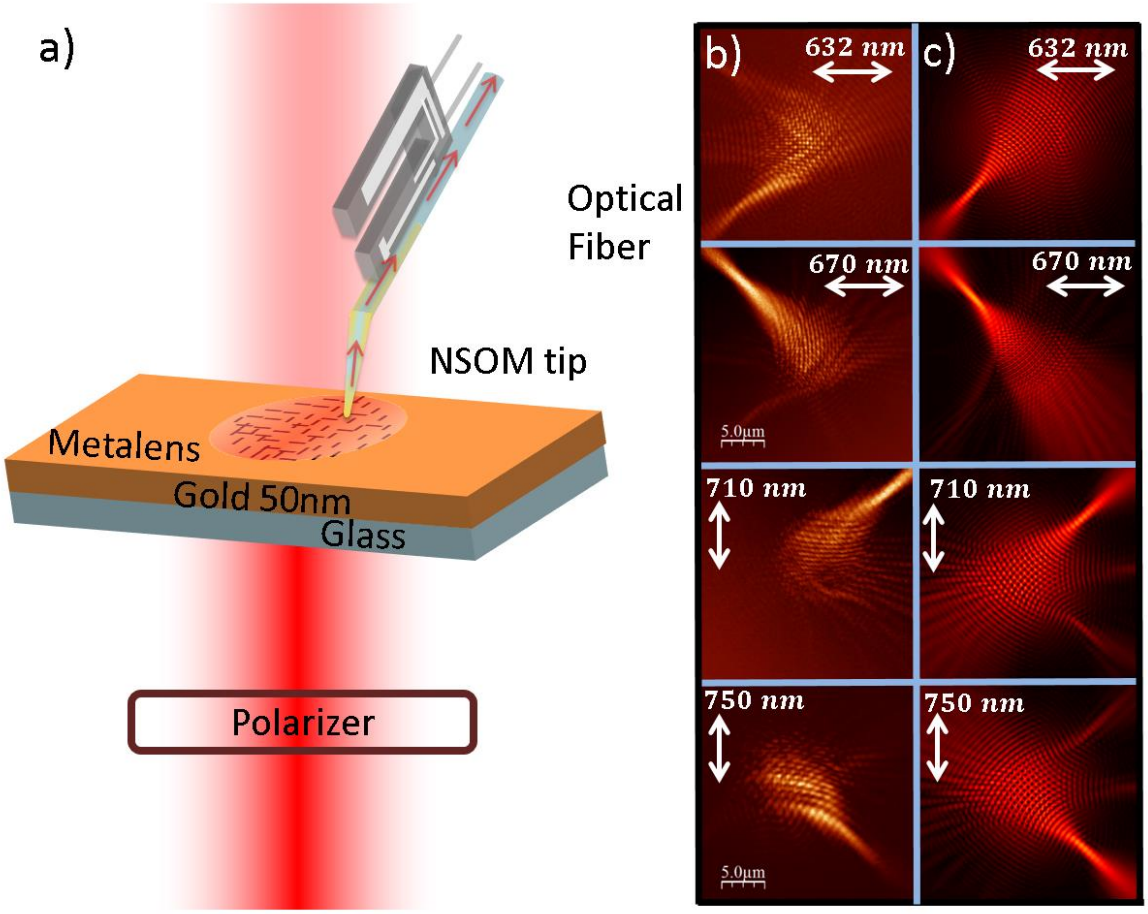

Figure 3-2. Experimental setup and results. a) Experimental setup—light from a supercontinuum laser source is incident on the sample from below. Light at a single wavelength is passed through a polarizer in order to set the incident light polarization, and the light is focused onto the metalens (not depicted). Some of the laser light is transmitted, which can produce an interference pattern in the data depending on the relative intensities of the surface plasmon polaritons (SPPs) and the transmitted light. Near-field scanning optical microscopy (NSOM) is used to collect light. The NSOM tip, which is a metal-coated, tapered optical fiber, interacts with the evanescent field of the SPP and scatters it,

converting energy from the SPP mode into a propagating waveguide mode in the optical fiber. b) Experimental results with the polarization of light denoted by the white arrow. SPP beams are unidirectionally focused to the four corners of a square depending on the wavelength and polarization. c) Analytical simulations used to compare to the experimental results. Each aperture (with the correct orientation) in the metalens is treated as a point dipole and the fields from all the nanoslits are summed to give the in-plane total electric field.

3.5 Experimental Results

Since the metallic film in our device is optically thin ($40 - 50\ nm$), some of the incident light is transmitted through the sample. This transmitted light interferes with the SPPs at the surface such that the signal recorded by the NSOM at each pixel is the SPP intensity modulated by this interference. This useful effect allows for direct imaging of the wavefronts of the focusing SPP beam without any external reference beam or interferometric setups. Figure 3-2b shows the operation of the device when illuminated by light with the correct polarization and wavelength from the laser source (one polarization and wavelength at a time). Directional focusing of SPPs on the surface is evident as the different wavelengths are focused to the four corners of a square.

3.5.1 Analytical Modeling

In order to better understand our experimental results, we implemented an analytical model of how the designed metalens will function. We treat each nanoslit as an infinitesimal perfect electric point dipole—with a direction of emission perpendicular to the slit, such that a vertical nanoslit is represented by a horizontal dipole. Adapting Eq. 2 from Ref. (*73*), we then sum the contribution from each antenna:

Equation 3-1. $$E_{total} = \sum_i \frac{e^{jk_{SPP}\left[(x-x_i)^2+(y-y_i)^2\right]^{\frac{1}{2}}}}{\left[(x-x_i)^2+(y-y_i)^2\right]^{\frac{3}{4}}}\left[(x-x_i)\cos(\eta)-(y-y_i)\sin(\eta)\right]$$

where k_{SPP} is the wavenumber of the surface plasmon, x_i, y_i is the position of the i^{th} dipole, and η is the angle of orientation of the nanoslit relative to the vertical—0 for vertical apertures and $\frac{\pi}{2}$ for horizontal apertures. This total field is then added to the electric field produced by a flat wavefront—representing our focused Gaussian beam at the focal plane. Implementation and comparison of this analytical model to the experimental results can be seen in Figure 3-2b,c. The agreement between the data and the analytical model suggests that multiple reflections of SPPs from the nanoslits are not a serious factor in the performance

of the device, as the model does not take this into account. Furthermore, an effective numerical aperture (NA) can be defined according to $NA = \frac{\lambda_{SPP}}{\pi w}$ where $2w$ is the full-width at half maximum of the beam at the focus. The effective NA for the metalens with this definition is calculated to be on average .68 for the operating wavelengths. The full width at half maximum at the focus for all the wavelengths is roughly λ_{SPP}. Reminiscent of the diffraction limit, this waist could be decreased by fabricating a larger metalens—a larger diameter metalens would include more wavevectors and recreate the point source more accurately. We note that the nanoslits closest to the focal point will contribute more than the nanoslits that are farther, mainly due to their dipolar nature (Equation 3-1) and their propagation losses

Table 1.

3.5.2 Efficiency Calculation

In order to calculate the relative efficiency of the metalens, it is useful to compare it to an isotropic scatterer of SPPs (for example, radially or circularly polarized light incident onto a circular aperture). The percentage of SPPs contained within

a given angle θ of the isotropic scatterer is simply given by $\theta/360°$. To compare this to our device, we measure the intensity of SPPs as a function of θ along the circumference of a circle with radius equal to the focal distance, 11.3 μm. We find that on average 23% of the SPPs at the focal radius are contained within a 10° angle, which is almost an order of magnitude higher than the isotropic scatterer, which only contains 2.8% of the SPP intensity within a 10° angle.

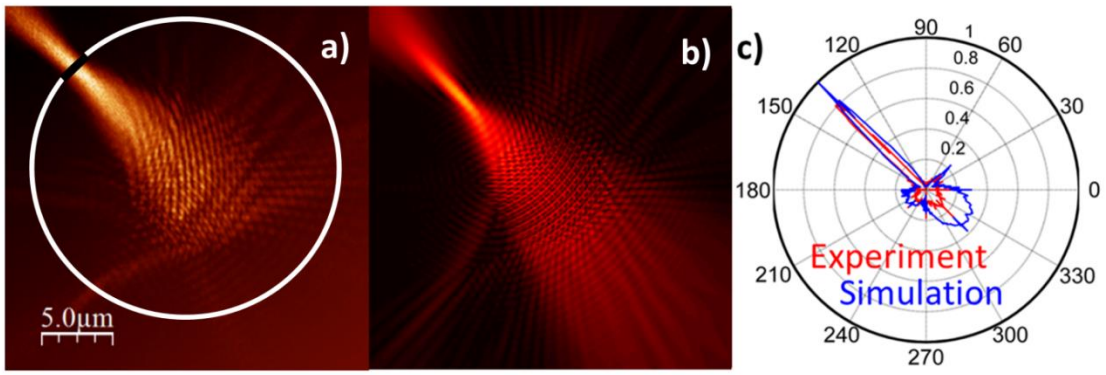

Figure 3-3. Angular agreement between simulation and experiment for the horizontally polarized $\lambda_0 = 670\ nm$ light case. a,b) Experimental and simulation data respectively, as presented in the main text. The white circle in (a) highlights the relative efficiency calculation method. Angular focusing efficiency is calculated as the intensity of the image at the focus (black line) divided by the total (white line), which is 23.3% for this image. c) Normalized intensity emission, which agrees to within $\pm 2°$ for all images.

3.6 Spectrally Resolved NSOM Imaging

In order to further characterize our metalens, we illuminated the sample with a wide band ($580 - 700\ nm$), chosen to include two of the operating wavelengths. In this case, the NSOM fiber is connected to a spectrometer (Andor Shamrock and Newton EMCCD Camera). The spectrally resolved NSOM data are presented in Figure 3-4. Interestingly, the SPPs are always concentrated into the two different channels, but with different relative intensities. For example, while $\lambda_0 = 632$ and $670\ nm$ light are almost completely concentrated into a single direction (following the original design), $650\ nm$ light is split between two directions (Figure 3-4e). This behavior, imposed by the design, can be understood by noting that the difference in SPP wavelengths is small compared to λ_{SPP}, ($\sim 20\ nm$ for $\lambda_0 = 632$ and $650\ nm$ light). When excited by $650\ nm$ light, the apertures are only slightly offset from the equiphase lines in Figure 3-1a, and their emissions will constructively interfere at the source points (though not as completely as it does for 632 and $670\ nm$). In addition, this explains why the power transfers from one direction to the other as λ_{SPP} gets closer to or further

away from one of the operating wavelengths. For example, 640 *nm* light concentrates more power in the 632 *nm* channel and less into the 670 *nm* channel; however, 660 *nm* light experiences the opposite. In terms of applications, monitoring the relative intensities in each arm would allow for an on-chip spectrometer.

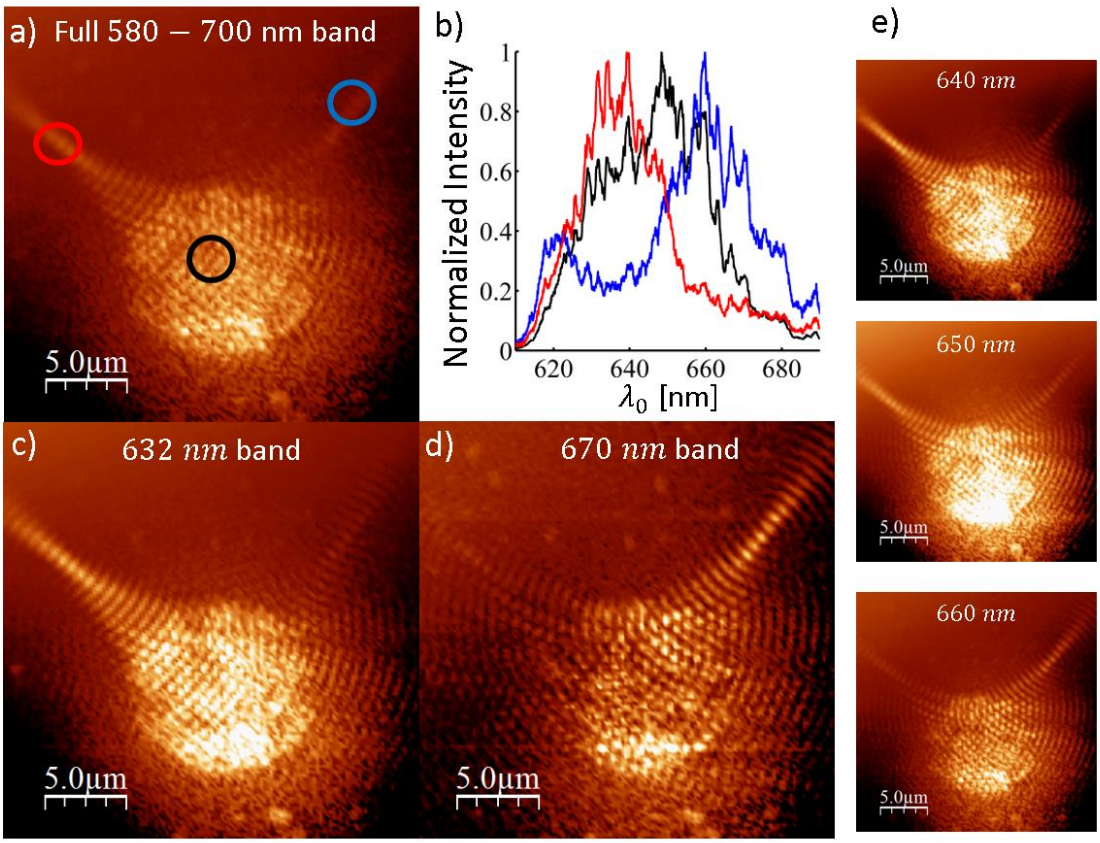

Figure 3-4. Spectrally resolved near-field scanning optical microscopy (NSOM) imaging. A single NSOM scan is performed while the metalens is illuminated with $\lambda_0 = 580 - 700\ nm$. The same experimental setup as in Fig. 2a is used except the optical fiber connected to a spectrometer. a) Spectrally resolved NSOM image for the whole wavelength range—each pixel in the image represents the number of counts in a wavelength range of $580 - 700\ nm$ (the full band). The colored circles in (a) correspond to the physical location on the metalens where the colored spectra (b) are taken, i.e., the black spectrum from (b) is taken inside the black circle in (a). Each curve in (b) is normalized independently to highlight the spectral shifts. c) Spectrally resolved NSOM image for a band of $632 \pm 3\ nm$. Each pixel intensity represents the sum of all photon counts within that wavelength range. d) Same as in c), but for a wavelength range $670 \pm 3\ nm$. e) Spectrally resolved data for wavelength bands in between the operating wavelengths. A unique characteristic of the device is that the power is always concentrated into the two directions, but with different relative intensities that depend on how close the wavelength is to the two operating wavelengths $(632, 670\ nm)$.

3.7 Polarization On/Off Switching

Figure 3-5 shows the focusing of the SPPs and characterizes the polarization on/off switching. In Figure 3-5a, the interference of the incident beam and focusing SPPs is shown in order to view the SPP wavefronts during focusing. In Figure 3-5b, the metalens is illuminated with the polarization that maximizes coupling into SPP modes. For comparison, Figure 3-5c shows the metalens when

illuminated with a polarization that is parallel to the associated nanoslits, minimizing the coupling to SPPs.

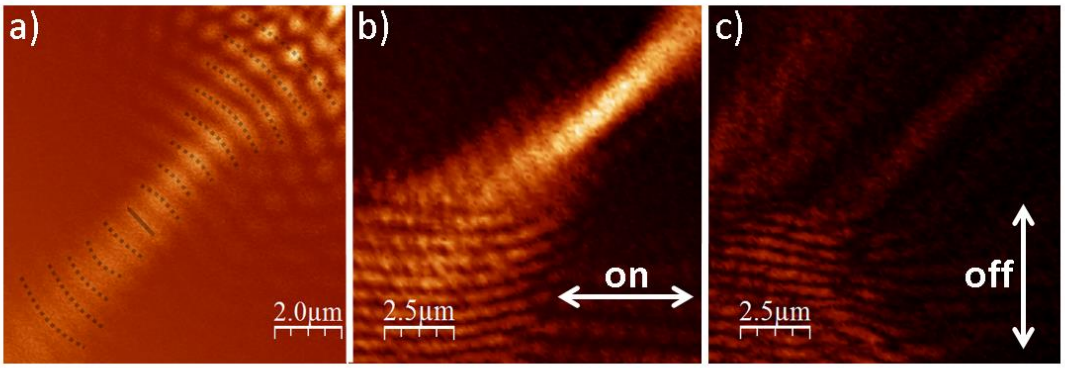

Figure 3-5. Focusing and polarization on/off switching. (a) Near-field scanning optical microscopy (NSOM) image of the focal point when the metalens is illuminated with 750 nm light with vertical polarization. Superposed are black dashed lines that highlight the wavefront curvature as the beam focuses, with the focus denoted by the solid black line. Note the single apertures in the top right portion of the image which act as surface plasmon polariton (SPP) sources (together with all the others in the device). b) SPP beam focusing for $\lambda_0 = 710\ nm$ when the metalens is illuminated with the 'on' polarization (horizontal). c) Same as panel (b) but with the metalens illuminated with the 'off' polarization (vertical). The ratio of the intensities at the foci of (b) and (c) are 15:1, giving 12 dB of modulation.

3.8 Conclusion

In this paper, we demonstrated a metalens design strategy that can be used to overcome some of the coupling and focusing issues for SPPs. The design strategy can be used to gain both wavelength and polarization tunability over the direction of SPP beam propagation; most importantly, by recreating the wavefront of a point source we are able to focus SPP beams after coupling. The metalens is studied under both single wavelength illumination (collecting intensity) and broadband illumination (collecting spectrally resolved intensity), with phase information in certain cases. Free space light is coupled to a nanostructured surface via subwavelength slits and steered into different directions based on its wavelength and polarization in the form of a focused SPP beam. We note that the relative efficiency of our metalens as compared to an isotropic coupler is improved by an order of magnitude. Also, the coupling conversion efficiency can be improved by optimizing the nanoslit geometry to take advantage of a plasmonic resonance. We show phase evolution of the created SPP beams, and highlight the focusing. In principle, these beams could

be easily outcoupled and re-radiated back into free space modes, which would serve to completely demultiplex free space light of different wavelengths, accomplished by a single, ultrathin optical element. The design strategy presented here could open up new opportunities in the realms of integrated waveguides, on-chip spectroscopy, or broadband demultiplexers.

3.9 Supplementary Information

λ_0	λ_{spp}	n_{eff}	**Propagation Length**
633	604	1.0478	12.5 μm
670	644	1.0395	21.9 μm
710	688.3	1.0315	34.0 μm
750	731.8	1.0249	45.5 μm

Table 1. Design parameters. Provides values of the free space wavelength, surface plasmon polariton wavelength, effective index of the SPP mode, and propagation length respectively for the different wavelengths used in the experiment. λ_{SPP} and n_{eff} are computed from tabulated Johnson and Christy data(37) and interpolated using high order polynomials to get accurate values.

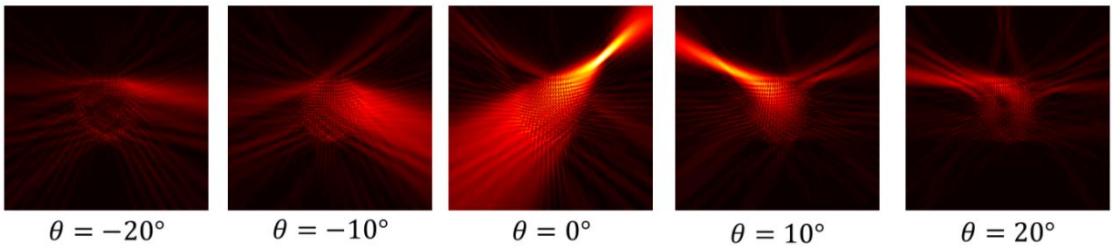

Figure 3-6. Analytical calculations plotting the SPP intensity of the metalens under varying angle of incidence for $\lambda_0 = 670\ nm$. When the angle of incidence changes, the nanoslits are no longer excited in phase, which reduces the constructive interference at the initial desired focal point.

As further proof of our design method, we fabricated a metalens that behaves as a two polarization and two wavelength tunable coupler. Only two operating wavelengths are chosen and the design strategy highlighted in Figure 3-1 is repeated, with the result shown in Figure 3-7. Figure 3-7b-e shows the dual wavelength and polarization tunability of the metalens where changing either the wavelength or polarization serves to completely change the direction of SPP

launching. The extra noise in the 670 nm horizontally polarized image is due a fabrication defect which caused the nanoslits in the top right portion of the image to have higher emission.

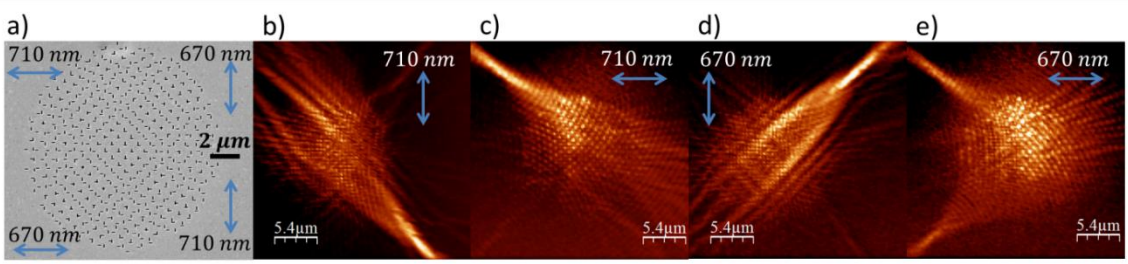

Figure 3-7. Two polarization and two wavelength demultiplexing metalens. a) Shows the scanning electron micrograph for the polarization demultiplexer, denoting where each wavelength ($\lambda_0 = 670$ or $710\ nm$) and corresponding polarization (blue arrows) will be focused, following the analogous procedure from the main text. Near-field scanning optical microscopy (NSOM) images obtained for all combinations of wavelength and polarization, highlighting the power of the metalens design strategy.

Chapter 4

Controlled Steering of Cherenkov Surface Plasmon Wakes with a One-dimensional Metamaterial

ABSTRACT

In the Cherenkov effect a charged particle moving with a velocity faster than the phase velocity of light in the medium radiates light that forms a cone with a half angle determined by the ratio of the two speeds. In this paper, we show that by creating a running wave of polarization along a one-dimensional metallic nanostructure consisting of subwavelength spaced rotated apertures that

propagates faster than the surface plasmon polariton phase velocity, we can generate surface plasmon wakes, a two-dimensional analogue of Cherenkov radiation. The running wave of polarization travels with a speed determined by the angle of incidence and the photon spin angular momentum of the incident radiation. By changing either one of these properties we demonstrate controlled steering of the Cherenkov surface plasmon wakes.

4.1 Introduction

As an accomplished sailor, Lord Kelvin was fascinated by the marvelous yet complex wave patterns generated behind his boat on the water's surface(*95*). He realized that his boat was always ahead of the waves that it creates, generating a wave pattern of two lines that form the arms of a V, with the boat giving rise to the wake at the apex. In shallow water, the angle γ between the boat trajectory and the wake is given by the relation: $\sin\gamma = c/U$, where c is the speed of the surface wave and U is the speed of the boat. In fact, this is a general wave phenomenon—wakes are formed each time a perturbation travels faster than the phase velocity of the waves it creates, accounting for phenomena as diverse as

sonic booms and Cherenkov radiation. The latter occurs when a charged particle (for example, an electron) moves at a velocity faster than the phase velocity of light in that medium. Microscopically, the moving charge induces a trail of polarization by interacting with polarizable dipoles in the medium. In returning to equilibrium, the induced dipoles re-radiate immediately after the electron has passed the interaction zone(*96*). (Note: the particle itself is not radiating and only the response of the medium produces the secondary waves forming the Cherenkov radiation.)

Combining Cherenkov physics with the concept of artificial optical materials, Veselago predicted that the wake of the Cherenkov radiation would be directed backwards relative to the motion of the charged particles in negative index materials(*97*). Experimental demonstration of this effect has been observed with microwaves, and promises the development of Cherenkov counters with higher efficiency(*98, 99*) along with novel high power electric devices with miniaturization and higher efficiency In Ref.(*99*), the authors showed that a moving charged particle can be accurately modeled by a phased dipole array

consisting of an infinite number of dipoles situated along the trajectory of the moving charge. More precisely, they demonstrated that the current density of a moving charge is very similar to the current density of a phased dipole array (note: the only noticeable difference is the charged particle emits a spectrum of frequencies). Other unusual Cherenkov emissions related to the Smith-Purcell effect have been reported for charged particles propagating in or nearby periodic media(*100, 101*), such as photonic crystals(*102*), and other types of periodic inhomogeneous or anisotropic media(*103-106*) Here, we show that a one-dimensional array of nanostructures can excite and steer surface plasmon wakes via a mechanism analogous to Cherenkov radiation.

4.2 The introductory case: a long slit

Consider a light beam polarized perpendicular to a slit etched in a thin metal film and incident at an angle θ. As analyzed by Lee *et al*.(*35*), this beam will induce a polarization along the slit. If $\theta = 0°$ and the slit is long compared to λ_{SPP}, the slit will radiate SPP plane waves that propagate with a wavevector normal to the slit. Instead, if S-polarized light impinges obliquely at an angle θ

(Figure 4-1a), the light creates a 'running wave of polarization' (RWP) with an amplitude that varies sinusoidally along the slit with a wavelength: $\lambda_{RWP} = \frac{\lambda_0}{\sin\theta}$, as indicated in Figure 4-1b, where λ_0 is the free space wavelength. The phase velocity of the RWP is $c_{RWP} = \frac{\lambda_{RWP}}{2\pi}\omega_0 = c/\sin\theta$, where c is the speed of light in vacuum and ω_0 is the frequency. Note that at normal incidence ($\theta = 0°$) c_{RWP} is infinite, and all of the dipoles are excited together in phase. An example of the electric field component normal to slit in the vicinity of the surface calculated by finite difference time domain simulation (FDTD) is shown in Figure 4-1c.

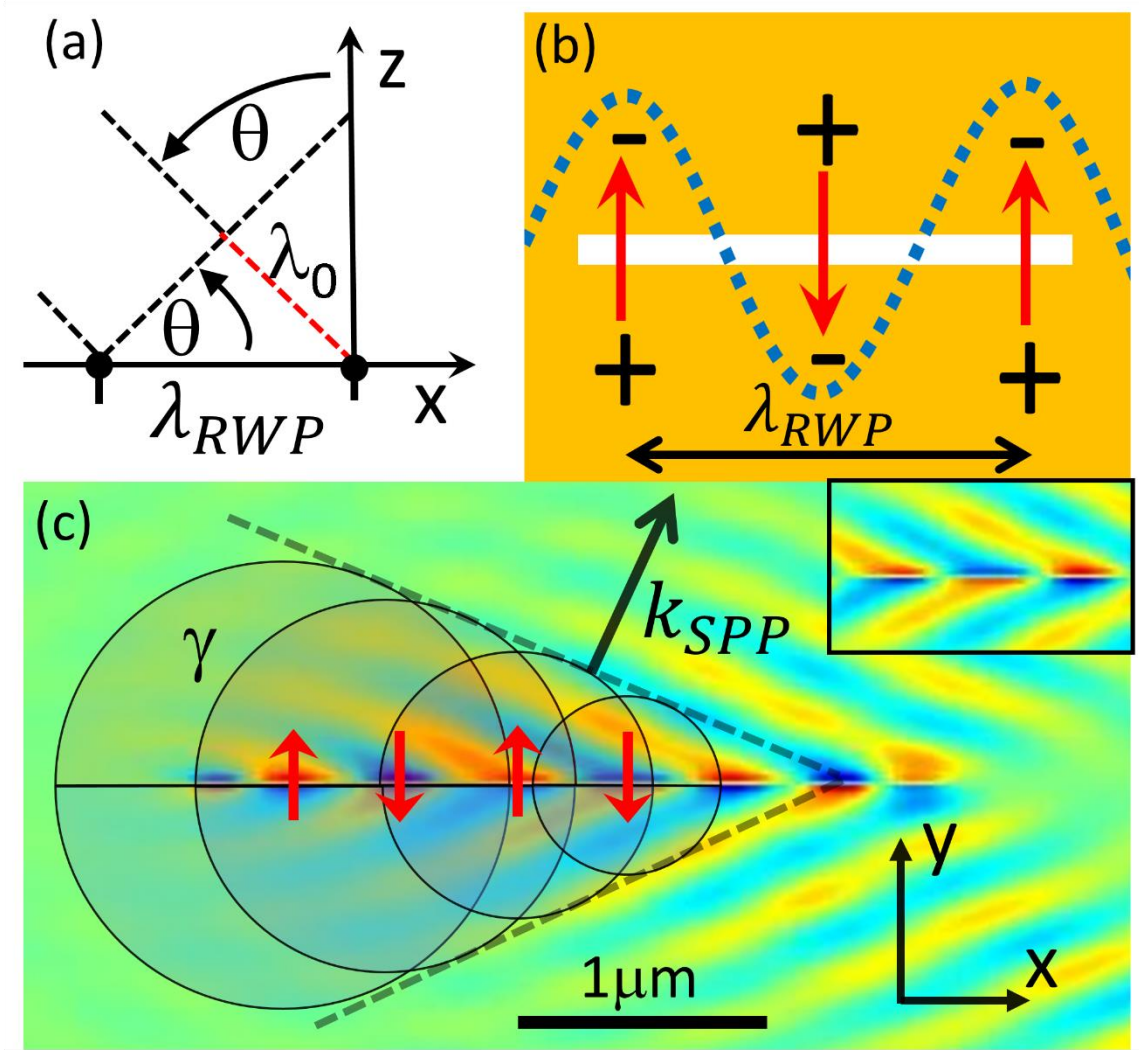

Figure 4-1. Excitation of Cherenkov surface plasmon wakes with a running wave of polarization. (a,b) Light impinging on a slit in a metal film at oblique incidence θ with free space wavelength λ_0 generates a running wave of polarization (RWP) of wavelength $\lambda_{RWP} = \frac{\lambda_0}{\sin\theta}$ which propagates with a phase velocity: $c_{RWP} = \frac{c}{sin\theta} > c_{SPP}$, where c is the phase velocity of light in free space and c_{SPP} is the surface plasmon polariton (SPP) phase velocity. The red dashed line denotes an extra path length of one free space wavelength, such that the light incident at

the black dots has the same phase. (c) Finite difference time domain (FDTD) simulation showing the real part of the electric field normal (z axis) to the slit (x axis) 5 nm above the surface. The slit (3 μm long and 50 nm wide) is excited at visible wavelength (610 nm) by a beam incident at $\theta = 30°$. The superimposed circles are the Huygens' representation of the surface waves centered at selected dipoles. It shows the running wave of polarization that generates the SPPs, which interfere to form wakes at an angle γ that follows the Cherenkov equation: $\sin\gamma = \frac{c_{SPP}}{c_{RWP}}$. The inset is a zoomed in view of the slit.

The running wave of polarization can be understood as a series of dipoles oriented normal to the slit axis, distributed along the slit with a phase profile: $\phi(x) = \frac{2\pi}{\lambda_0} x\sin\theta$, which propagates along x at a velocity c_{RWP}. As can be seen in Figure 4-1c, the RWP excites SPPs that constructively interfere along the dashed lines, creating wakes defined by the angle γ. The angle of the wakes can be derived by imposing the condition that the propagation phase shift $\left(\frac{2\pi}{\lambda_0}\sin\theta\,\Delta x_0\right)$ between two light rays of the incident wavefront at an angle θ, impinging on the surface at points separated by a distance Δx_0, is exactly compensated by the phase shift $\left(\frac{2\pi}{\lambda_{SPP}}\sin\gamma\,\Delta x_0\right)$ between SPP wakes propagating out of those points. This yields:

$$\text{Equation 4-1. } \sin\gamma = \frac{c_{SPP}}{c_{RWP}} = \frac{sin\theta}{n_{eff}}$$

where: $n_{eff} = \frac{\lambda_0}{\lambda_{SPP}} = [(\epsilon_{air}\ \epsilon_{metal})/(\epsilon_{air} + \epsilon_{metal})]^{1/2}$ is the effective index of the SPP mode on a metal-air interface. Note that n_{eff} always exceeds unity and the SPP dispersion curve is below the lightline; thus the condition for generating SPP wakes: $c_{RWP} = \frac{c}{sin\theta} > c_{SPP}$ is satisfied for any θ.

We experimentally analyzed the angle of surface plasmon wakes from a slit as a function of angle of incidence with a near-field scanning optical microscope (NSOM) (see Supplementary Fig. 3). To access not only the intensity, but also the phase profile of SPPs propagating on the metal film, we used a ~50 nm thick gold film, template stripped(*107*) from a silicon wafer. The film thickness allows a fraction of the incident free-space light to be transmitted through the film and interfere with the SPPs propagating along the gold-air interface. The light intensity collected at each point of the NSOM scan is the interference of the electric field of the incident light and the SPP field generated by the slit. An example of the resulting interference is presented in Figure 4-2a. From this interference pattern, we can extract the angle of propagation γ of the SPP wakes.

Even though the wakes are generated at an angle γ given by Equation 4-1, the fringes are parallel to the slit due to the interference of the SPP wake and the obliquely incident beam that is transmitted through the thin gold film (see supplementary material sections 1 and 3). Through geometric analysis, we derive the angle of the SPP wake from the period of the intensity modulation, $\Delta y = \frac{\lambda_0}{n_{eff}\cos\gamma}$. Combining this expression with Equation 4-1, we obtain the separation of the fringes as a function of the angle of incidence:

Equation 4-2. $$\Delta y = \frac{\lambda_0}{\sqrt{n_{eff}^2 - (\sin\theta)^2}}$$

The solid line in Figure 4-2b represents the calculated Δy expressed in terms of θ using Equation 4-2. To extract the experimental value of Δy, we compute the spatial Fourier transform of the NSOM scans (inset Figure 4-2a), and compare the results with the expression above (Figure 4-2b).

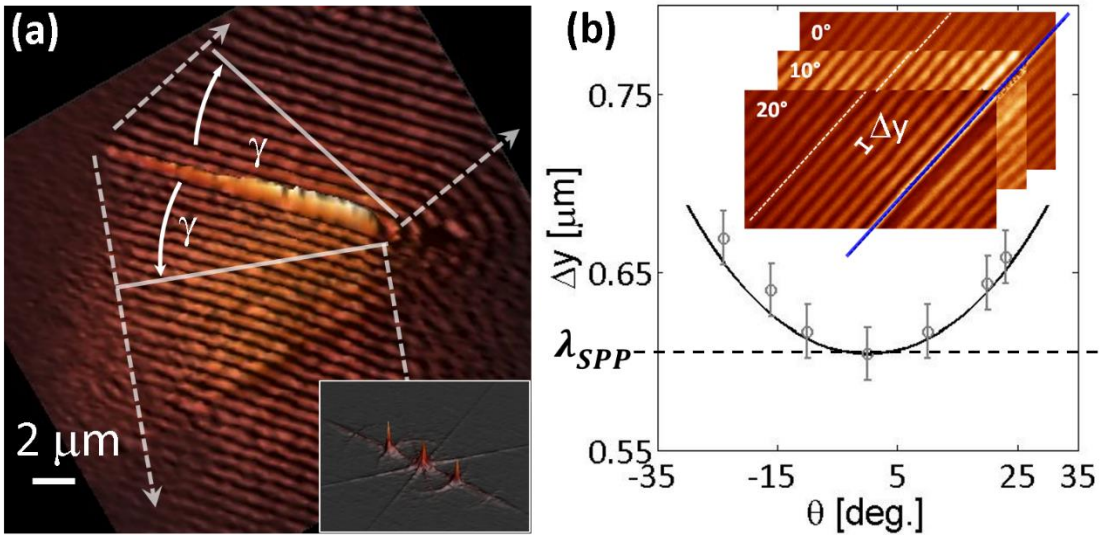

Figure 4-2. Near-field scanning optical microscopy data for surface plasmon wakes created along a long slit etched in a metal film. (a) Three-dimensional rendering of an experimental near-field scanning optical image of the interference pattern of surface plasmon wakes propagating and a beam incident at an angle $\theta = 23°$. γ is the angle of wake propagation with respect to the slit axis. The fringes result from the interference pattern of the surface plasmons and the incident light that is transmitted through the thin gold film. The fringes are parallel to the slit but the surface plasmons propagate at an angle relative to the slit (see Supplementary Fig. 1). The white arrows indicate the wavevector of the surface plasmon wakes, and the grey dashed lines denote the wavefront. Inset: spatial Fourier transform of (a), which is used to calculate the period of the interference pattern. (b) Evolution of the period of the interference pattern as a function of θ. The solid line is the expected theoretical value from Equation 4-2; its minimum corresponds to the surface plasmon wavelength: $\lambda_{SPP} = \lambda_0/n_{eff}$. The inset shows the measured interference patterns for different angles θ. The blue line in the inset represents the position of the slit for all three images. The distance between the white dashed line and the slit in each image corresponds to $7\Delta y$, providing a visualization of the change in fringe separation with angle of

incidence. Error bars in Δy are computed as the full-width at half maximum (FWHM) of the peaks in the Fourier transform in the inset of (a).

Metasurfaces made of arrays of optical resonators (antennas, etc.) have been widely investigated recently (*53, 61, 62, 108, 109*) In our experiment, we use a 1D metagrating made of elements that introduce a linear phase shift along the running wave of polarization's trajectory. This extra phase shift $\Delta\phi$ is imposed by fabricating aperture antennas in a line, separated by a distance small compared to λ_{SPP}. With these local phase shifts along the trajectory of the RWP, we modify the radiation angle γ of SPP wakes. A plane wave incident on the surface at an angle θ will excite SPPs in adjacent antennas, which will constructively interfere at an angle γ given by the condition that the phase shifts associated with optical paths of adjacent antennas are equal. From Figure 4-3a, one can see that this condition can be written as:

Equation 4-3. $$k_0 \sin\theta\, \Delta x + \Delta\phi = k_{SPP} \sin\gamma\, \Delta x$$

The first term in Equation 4-3 represents the relative phase shift due to the plane wave's oblique incidence θ on two adjacent apertures separated by Δx ($<< \lambda_0$)(

Figure 4-3a). The term on the right hand side of the equation represents the phase shift between the SPP waves emerging from the two antennas, and $\Delta\phi$ is the phase difference introduced by the 1D phased array (Figure 4-3a). Taking the limit $\Delta x \rightarrow 0$ yields the relation:

Equation 4-4. $$\sin\gamma = \frac{sin\theta}{n_{eff}} + \frac{1}{k_{SPP}}\frac{d\phi}{dx}$$

Note that the wakes can be made to propagate either forwards or backwards with respect to the RWP depending on the relative magnitude of the terms on the right hand side of Equation 4-4.

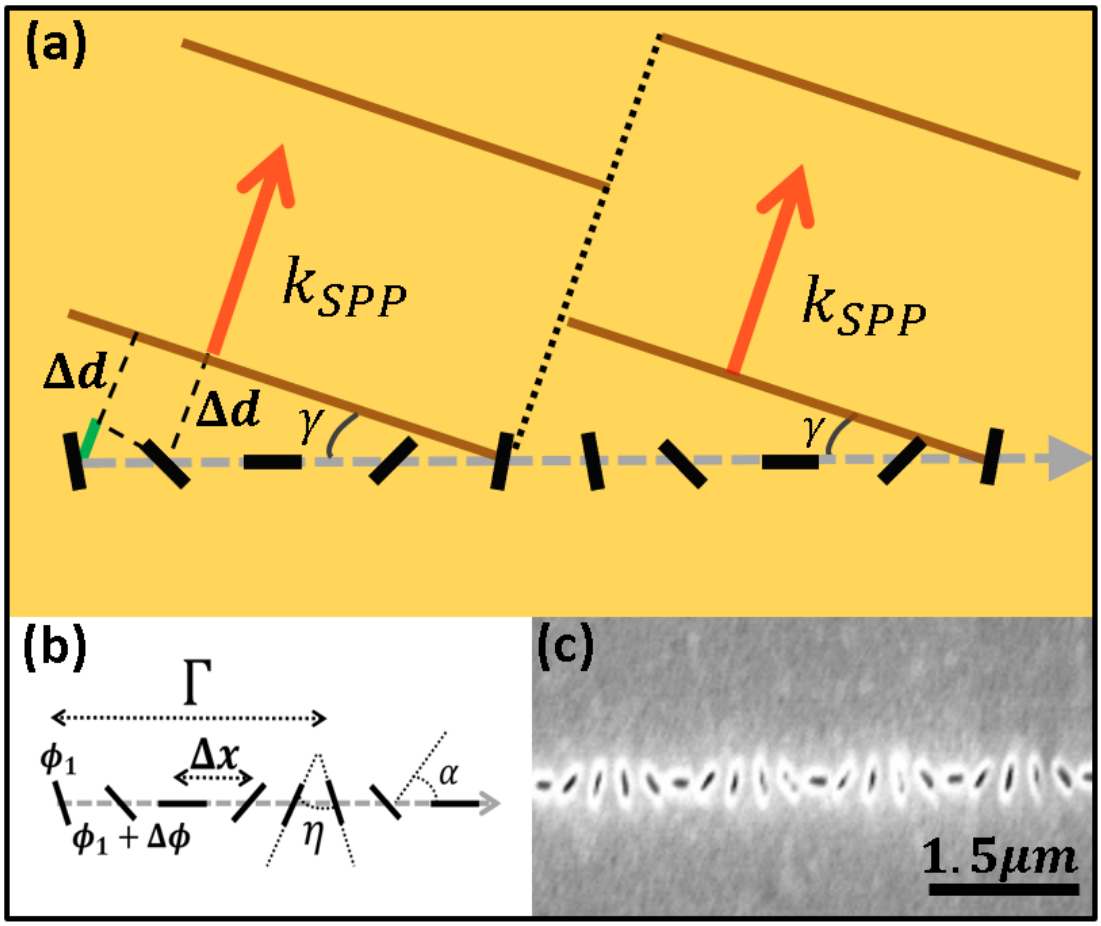

Figure 4-3. Creation of SPP wakes by a one-dimensional metamaterial and SEM of the nanostructure. (a,b) Schematic representation of the creation of surface plasmon polariton (SPP) wakes by a one-dimensional array of aperture antennas (black rectangles) designed to generate a phase change with constant phase gradient $\frac{\Delta\phi}{\Delta x}$ in the emission of SPPs. The 1D phased array is excited by light incident on the surface at an angle θ, creating a running wave of polarization denoted by the grey arrow. In (a) the SPP propagation path length difference between adjacent antennas is highlighted in green (corresponding to the right hand side of Equation 4-3. $k_0 \sin\theta\, \Delta x + \Delta\phi = k_{SPP} \sin\gamma\, \Delta x$). Note that each antenna period, denoted by Γ in (b), creates its own wake (brown lines) which

arises from the constructive interference of the wavelets originating from each antenna within the period. The angle of the wake γ depends on the angle of incidence (Equation 4-4. $\sin\gamma = \frac{sin\theta}{n_{eff}} + \frac{1}{k_{SPP}}\frac{d\phi}{dx}$), where positive (negative) γ corresponds to a wake wavevector propagating to the right (left). The dotted black line corresponds to the zero intensity alleys separating the wakes generated by adjacent periods. (b) The angle γ can be controlled by changing $\Delta\phi$, which is proportional to the spatial rotation rate of the antennas $\frac{d\alpha(x)}{dx} = \frac{\Delta\phi}{\Delta x} = \frac{\pi}{\Gamma}$. η is defined as the rotation step. (c) Scanning electron micrograph of the nanostructures used to generate the SPP wakes. The apertures are created by focused ion beam milling.

By replacing the slit discussed in the introduction with the ensemble of rotating linear apertures of Figure 4-3, we experimentally demonstrate the ability to route the SPP wakes in different directions by introducing a local phase shift. As discussed recently, there are different ways for achieving local phase shifts (*110-112*). Here we use the geometric phase shift (often called the Pancharatnam–Berry phase) imparted to the SPPs by the interaction of elliptically or circularly polarized light with anisotropic aperture antennas.

Consider normally incident light with linear polarization. Even if the antennas are sequentially rotated, all of the apertures are excited in phase (with different amplitudes that depend on the projection of the polarization onto the axis normal to the aperture). This scenario does not allow us to introduce a local phase shift from the rotation of the apertures. On the other hand, circularly or elliptically polarized light has a phase delay between the x and y components, and this phase delay introduces a dephasing in the excitation of the rotated apertures. Under this illumination condition, coupling to SPPs at a nanoslit depends on the electric field component perpendicular to the nanoslit ($E_x \cdot \hat{n} + E_y \cdot \hat{n}$, where $\hat{n}$ is the unit vector perpendicular to the nanoslit). For circularly polarized light, this field projection is constant in amplitude with respect to the orientation of the nanoslit; however, its phase depends linearly on the nanoslit rotation angle. Therefore, by simply rotating each nanoslit, one by one with respect to the others a progressive phase delay in SPPs emission can be imposed (see Supplementary Fig. 2 and Fig. 8 and section 2.2). This phase shift combines with the phase shift associated with the angle of incidence to modify the emission angle of the SPP wakes (*110, 112*). Because of both their local

orientation (Figure 4-3b) and the spin angular momentum associated with circular polarization, the phase shift varies with the rotation angle as:

$$\text{Equation 4-5.}\quad \frac{\partial \phi}{\partial x} = \sigma_{\pm} \frac{\pi}{\Gamma}$$

where $\sigma_{\pm} = \pm 1$ is the photon's spin corresponding to right and left circular polarization respectively. Thus, according to Equation 4-4 and Equation 4-5, the angle of the wakes becomes photon spin-dependent with an extra phase shift $\Delta\phi$ that can be added or subtracted from the phase shift due to the obliquely incident light. For light impinging at normal incidence, the angle γ of the wakes, which was 0° for the slit, becomes nonzero and opposite by reversing the spin angular momentum of the light.

4.3 Phased Array Analytical Modeling

The expected SPP intensity distribution far from each antenna can be calculated by using the model discussed previously, which approximates the line of apertures by a series of phased dipoles with varying orientation, as given by Equation 4-5. Every antenna on the line can be modeled by a single, in-plane

dipole oriented normal to the aperture (see Supplementary information section 2). Notice that, for a given observation point on the surface, while the amplitude of the SPP from each antenna depends on the antenna orientation, the SPP wakes result from the coherent sum of the SPPs excited by each nanoslit. Using this dipolar model, we calculated the SPP fields emitted by a linear array of 10 periods of apertures rotating at a rate: $= \frac{\pi}{1.5\mu m}$. These are assumed to be excited by a focused Gaussian beam impinging onto the apertures at normal incidence, i.e., with a flat wavefront (Figure 4-4a). Under this condition, the coupling efficiency of light to surface wakes is rather low. Around 13 % of the incident optical power is coupled at the metallic surface. The efficiency of this launching mechanism can be significantly increased by utilizing a plasmonic resonance, or by changing the incident light beam waist to concentrate more of the power onto the nanoslits (see Supplementary Fig. 9 and Fig. 10).

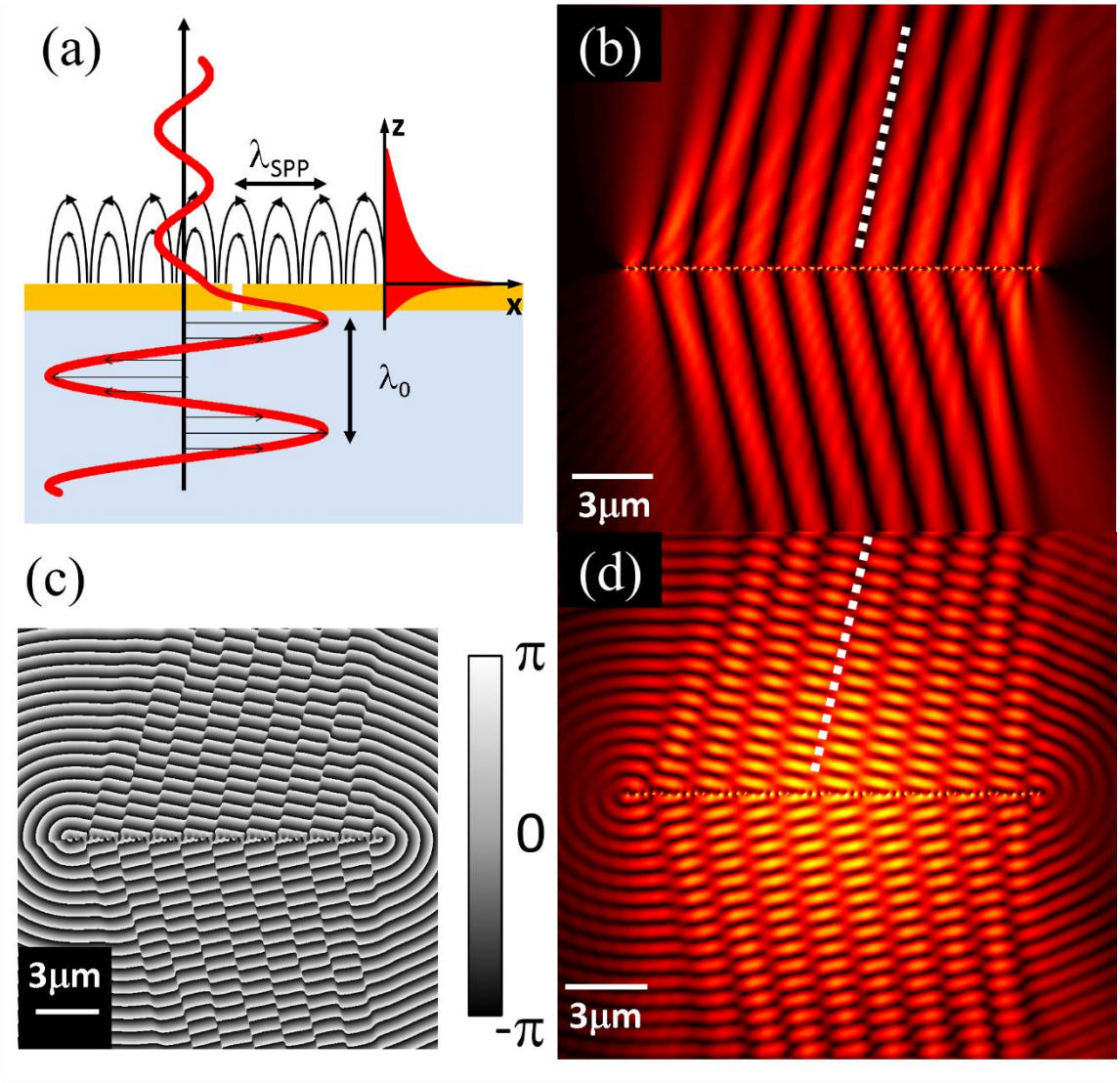

Figure 4-4. Analytical model treating the rotated nanoslits as a phased dipole array, including the interference between the SPP wakes and the incident beam. (a) Light incident onto an aperture excites surface plasmon polaritons (SPPs) and some light transmits through the thin gold film. (b) Calculated intensity and (c) phase distribution of SPPs generated by a phased array (rotated apertures) with $\Gamma = 1.5\ \mu m$ excited by right circularly polarized light. The imparted phase from

the rotation of the apertures varies from 0 to π along each period, creating alleys of high intensity separated by lines of zero intensity. Simpler geometries are presented in Supplementary Fig. 4 and Fig. 5. (d) The simulated interference pattern between the SPPs and the transmitted beam for normal incidence. The white dashed line represents the alley where the SPP electric field is zero; the intensity is that of the transmitted beam. These lines are parallel to the direction of propagation of the wakes. Comparison of the analytical model to an FDTD computation is presented in Fig. S7.

The results of the calculation in Figure 4-4a show that the arrangement of antennas generates SPP wakes which feature parallel alleys of vanishing intensity (dotted line in Figure 4-3a) oriented in the direction of constructive interference as shown in Figure 4-4d. This effect is due to the phase shift introduced by each period, which according to Equation 4-5 varies only from 0 to π. This range occurs because linear antennas oriented at α and $\alpha + \pi$ are equivalent, as can be seen from Figure 4-3a. Thus, each period generates an independent plasmon wavefront, tilted as described by Equation 4-4 and π-phase shifted with respect to the wavefronts generated by the two adjacent periods (Figure 4-3a). Furthermore, due to destructive interference, zero intensity alleys are created in the direction normal to the wavefronts. These lines (Figure 4-4b) correspond to the low intensity parallel alleys in Figure 4-4d, where the residual

intensity is that of the transmitted beam. At normal incidence, the wavefront is spatially homogeneous in the xy plane; therefore, interference with the SPPs produces an intensity distribution where the maximum intensity lines within each alley match the SPP wavefronts. Using the dipolar model we calculated the expected intensity and phase distribution of the surface plasmons (Figure 4-4b,c respectively).

To verify the generation of wakes as predicted by Equation 4-4, we excite the apertures at an angle. To do so, we modify the NSOM setup to excite the apertures with a circularly polarized focused Gaussian beam at oblique incidence, as shown in Figure 4-5a. An example of the experimental NSOM images (Figure 4-5d,e) obtained using σ^+ polarization and comparison with the dipolar model (Figure 4-5b,c) are also presented. Interestingly, since the incident beam that interferes with the plasmon field is not impinging at normal incidence, the lines of maximum intensity within each alley are not normal to the SPP wakes' propagation direction. To accurately measure the angle of the plasmon wakes, we rely on the orientation of the minimum intensity lines, which are

parallel to the alleys and wavevectors (Figure 4-5). We obtained images for different angles of incidence θ and spin angular momentum of light, extracted the γ angles, and compared our results with the theoretically expected angles given by Equation 4-4.

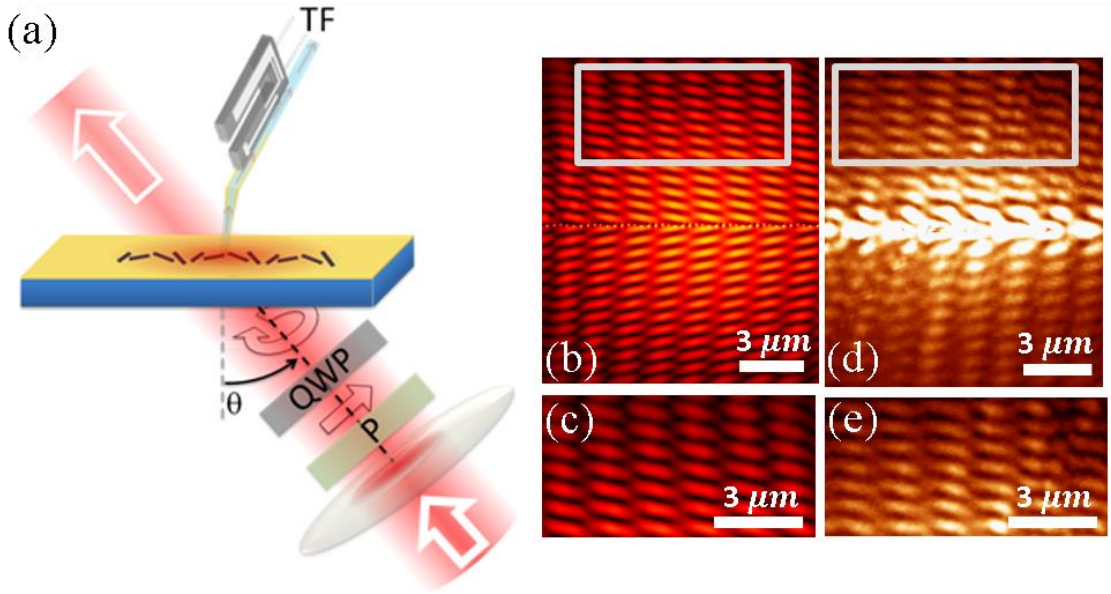

Figure 4-5. Experimental setup, NSOM images for the one-dimensional metamaterial, and comparison to analytical model. (a) Schematic of the near-field scanning optical microscope (NSOM) setup. A circularly polarized beam is incident at different angles onto the sample. The NSOM signal measured is the interference between the surface plasmons and the transmitted laser light. P, QWP, and TF denote the polarizer, quarter wave plate, and the NSOM tuning fork respectively. (b) and (d) are the calculated and measured results respectively, using the experimental setup in (a) with angle of incidence $\theta = -18°$ (sign denotes counterclockwise, as in panel a). (c) and (e) are the insets of (b) and (d) at the location given by the two white rectangles.

The measurements are in excellent agreement with the calculated images and the theoretical expected angles (Figure 4-6). By exciting the apertures with light with spin angular momentum, we achieve directional launching of SPPs. Unidirectional on-axis emission (*75*) (corresponding to $\gamma = 90°$), could also be possible whenever the phase velocity of the RWP along the line (Equation 4-5) matches the phase velocity of SPPs. Interestingly, we also note that an analogue to reversed Cherenkov radiation, previously observed in negative index metamaterials(*113*), can be observed in our device simply by switching the spin of the photon for small angles of incidence (Figure 4-6b), as the SPP wakes can be made to propagate in the forward or backward direction relative to the incident light.

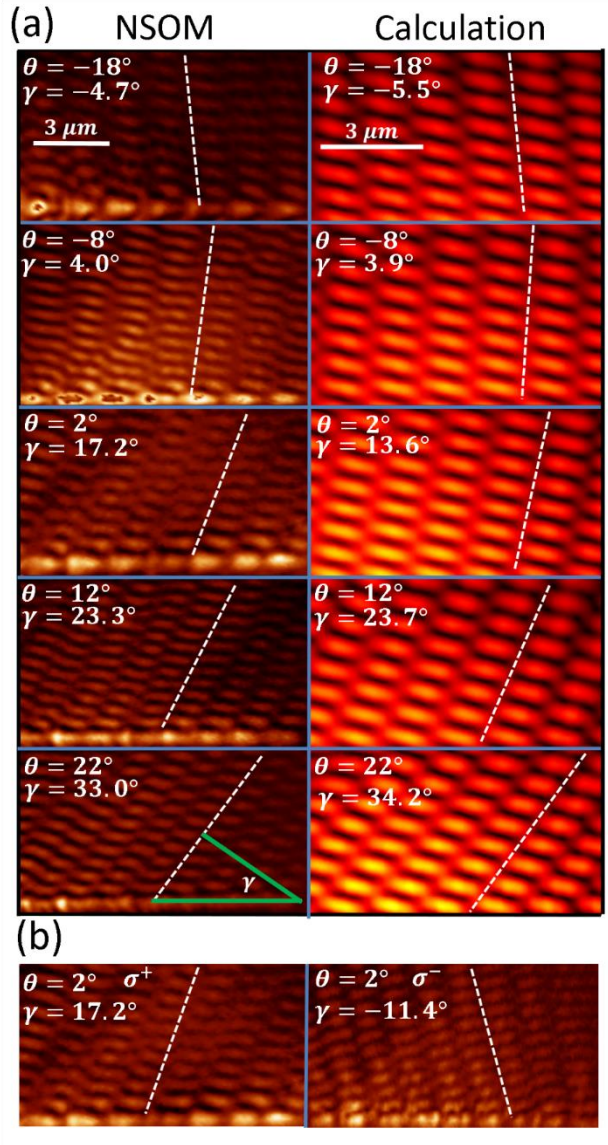

Figure 4-6. NSOM images on the steering of surface plasmon wakes. (a) Side-by-side comparison between near-field scanning optical microsope images for different angles of incidence and the calculated interference patterns. The linear

array of antenna apertures has a period $\Gamma = 1.5\ \mu m$ and the incident beam is σ^+ polarized. The dashed lines show the minmum intensity regions parallel to the alleys. The angles γ are obtained from the intersection of the normal to the white dashed lines as shown with the green lines. (b) Comparison between σ^+ and σ^- polarization showing that for small angles, changing the spin angular momentum of the light reverses the direction of the wakes. The standard deviation on the γ angle measurements for all experimental images is $< 2.8°$.

Expanding on the Cherenkov description for the case of a slit, where the wake angle is determined by $\sin\gamma = \frac{c_{SPP}}{c_{RWP}}$, we derive a generalized phase velocity for the RWP of a 1D phased array metamaterial, where $\sin\gamma = c_{SPP}/c_{RWP,gen}$. By substituting in Equation 4-4 and recalling that the phase gradient is given by Equation 4-5, we find that:

Equation 4-6. $$c_{RWP,gen} = \frac{c}{\sin\theta \pm \frac{1}{k_0}\frac{\pi}{\Gamma}}$$

From Equation 4-6, we note that by decreasing the phase velocity of the excitation, i.e., by increasing the magnitude of the denominator, one could access an interesting new regime in which a propagating polarization wave, with dispersion given by $\omega = c_{RWP,gen}k$, exists along the line of apertures without creating any SPP wakes. Such a subplasmonical regime is connected to the recent work by Sun *et al*. and Qu *et al*., in which the authors studied the propagation of

waves guided along gradient index metasurfaces and their re-radiation into free space (*114-116*). They reported that 2D metasurfaces radiate into free-space whenever the moving charges have an effective velocity greater than the speed of light. Below this limit, the waves are confined at the interface. In our structures, analogous driven waves could be confined along a line and generated without coupling to a propagating SPP mode.

4.4 Conclusion

In this section of the thesis, we demonstrate that a 1D metamaterial made of rotated nano-apertures etched in a metallic film can arbitrarily control the phase velocity of a running wave of polarization propagating along the line formed by the apertures. The phase velocity of the running wave of polarization exceeds the SPP phase velocity and results in the creation of SPP wakes. We show that SPPs are excited and constructively interfere via a mechanism analogous to Cherenkov radiation, and we demonstrate that the rotation of the antennas makes the wake direction spin angular momentum dependent, meaning that the direction of propagation of SPPs could in principle be reversed in the real time

by rotating a quarter waveplate to change the incident polarization from σ^+ to σ^-. This demonstration of SPP wake generation and SPP steering can be further exploited to create new types of plasmonic couplers such as plasmonic holograms (*86*) or directional lenses (*117, 118*). Besides connecting this coupling mechanism with the physics of the Cherenkov effect, our methodology could represent a unique and practical way to test concepts associated with fast traveling perturbations. This work also brings the concepts of leaky wave antennas, previously demonstrated in the millimeter and microwave bands (*119*) to optical frequencies. Leaky wave antennas have found innovative applications in wavefront engineering, and we expect that these ideas can be exploited to develop similarly impactful applications at optical frequencies.

4.5 Supplementary Information

4.5.1 Full Description of the NSOM Interferogram of the Slit Case

In our experiments, to observe SPP wavefronts (without having to set up a phase-sensitive NSOM experiment, which is a cumbersome and difficult task in the visible), we used the fact that some fraction of the incident wavefront is

transmitted through the thin metallic film and interferes with the plasmons propagating on the other side of the film, as was recently shown (*120*). NSOM images obtained in our experiments show the near-field intensity of the interference pattern between surface plasmons propagating on the metal film and the transmitted light. This interference gives information on the phase distribution of the propagating SPPs. The interfringe distance is given by $\Delta y = \lambda_{SPP}/\cos\gamma$ (Figure 4-7b). By measuring Δy, this expression is used to calculate the angle of the wakes γ and these are compared to the experimental values.

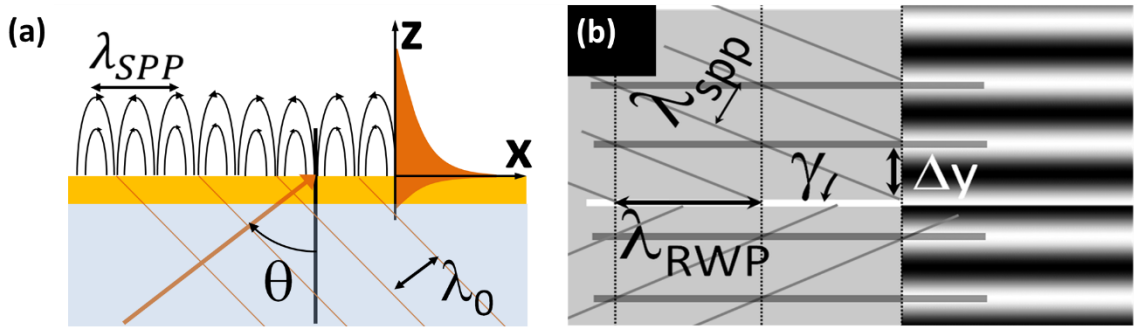

Figure 4-7. (a) x-z schematic of the experiment and resultant electric fields on the control sample (slit). Obliquely incident free space light (wavefronts shown as thin orange lines) generates SPPs, which propagate away from the slit with wavefronts tilted at an angle γ. The SPP wavefronts are shown in (b) as gray lines. A purely visual representation of their interference with the incident oblique wavefront (vertical lines) is shown. This constructive interference produces an intensity pattern with iso-intensity lines parallel to the slit axis

(thick grey lines). The distance between the interference fringes, denoted by Δy, is experimentally measured and used to calculate the SPP emission angle γ.

4.5.2 Dipole-like Description of Linear Rotating Aperture Antennas

4.5.2.1 Surface Plasmon Polaritons from a Straight Aperture Antenna

When a surface plasmon is generated at a metal-dielectric interface by illuminating a subwavelength slit on the metallic film (straight apertured antenna), the two-dimensional evolution of the electric field (complex amplitude) in the plane can be approximated by:

Equation 4-7. $E_{SPP}(x,y) = \frac{e^{jk_{SPP}((x-x_0)^2+(y-y_0)^2)^{\frac{1}{2}}}}{((x-x_0)^2+(y-y_0)^2)^{\frac{3}{4}}}((x-x_0)\cos\alpha - (y-y_0)\sin\alpha)$

where $k_{SPP} = \frac{2\pi}{\lambda_{SPP}}$ is the SPP wavenumber (neglecting any attenuation of the SPP), x_0, y_0 is the position of the aperture, α is the angular orientation, and $j = \sqrt{-1}$. This equation is obtained by transforming equation (2) of Reference (*73*) to follow the notation and orientation of axes introduced in Figure 4-8.

Figure 4-8 also shows the dipole-like intensity and phase distributions of the SPPs from a straight aperture antenna oriented along the x-axis computed using Equation 4-7 and excited by an S-polarized source impinging at normal incidence.

If more apertures are milled into the metallic surface, it is possible (neglecting near-field interactions between apertures), to consider SPPs from each antenna, as described by Equation 4-7. Then the contributions from each dipole are summed up (each with phase and amplitude) to obtain the total field distribution of the surface wave. It is worth noting that, although simplistic, this approximation can still be applied to cases of practical interest (*73, 121*).

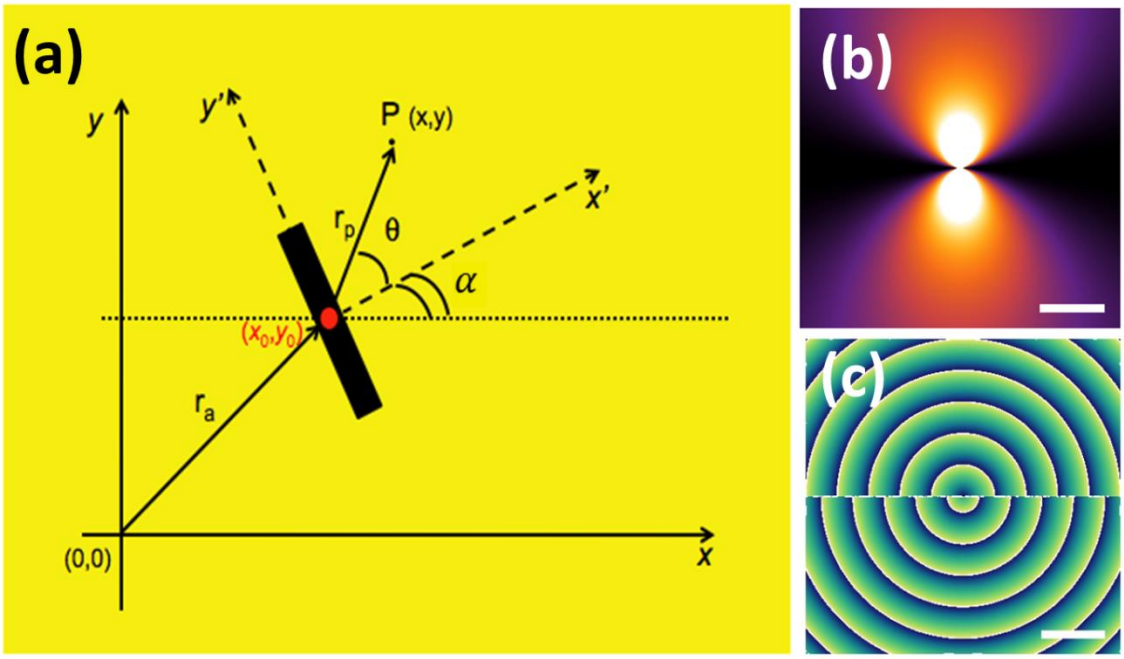

Figure 4-8. (a) Notations for the axes and antenna rotation angle (α). (b) Calculated intensity at the metal film and (c) phase distribution of the SPPs launched by a straight aperture antenna oriented along the x-axis. The scale bar length in the pictures is $2\lambda_{SPP} = 1.2\mu m$.

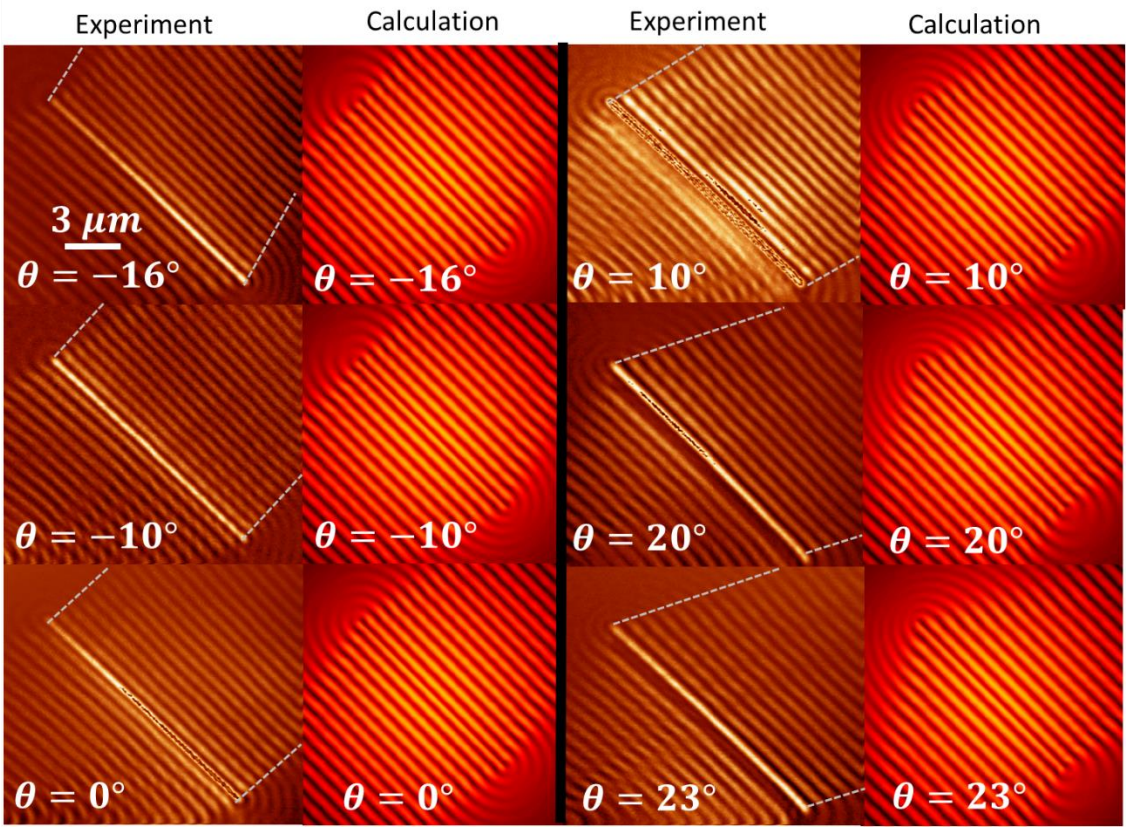

Figure 4-9. Left: experimental NSOM data for slits with different incident angles. Right: calculated electric field distribution of the interference pattern of surface plasmon wakes excited by S-polarized light at different incident angles. The results are summarized in Figure 4-2 in the main text.

Figure 4-10 shows two cases of straight aperture antennas close together, rotated by $\frac{\pi}{2}$ and excited by a linearly polarized beam incident at 45°. In this case, there is no further phase delay between the antennas and the final picture is only due to the relative orientations of the apertures.

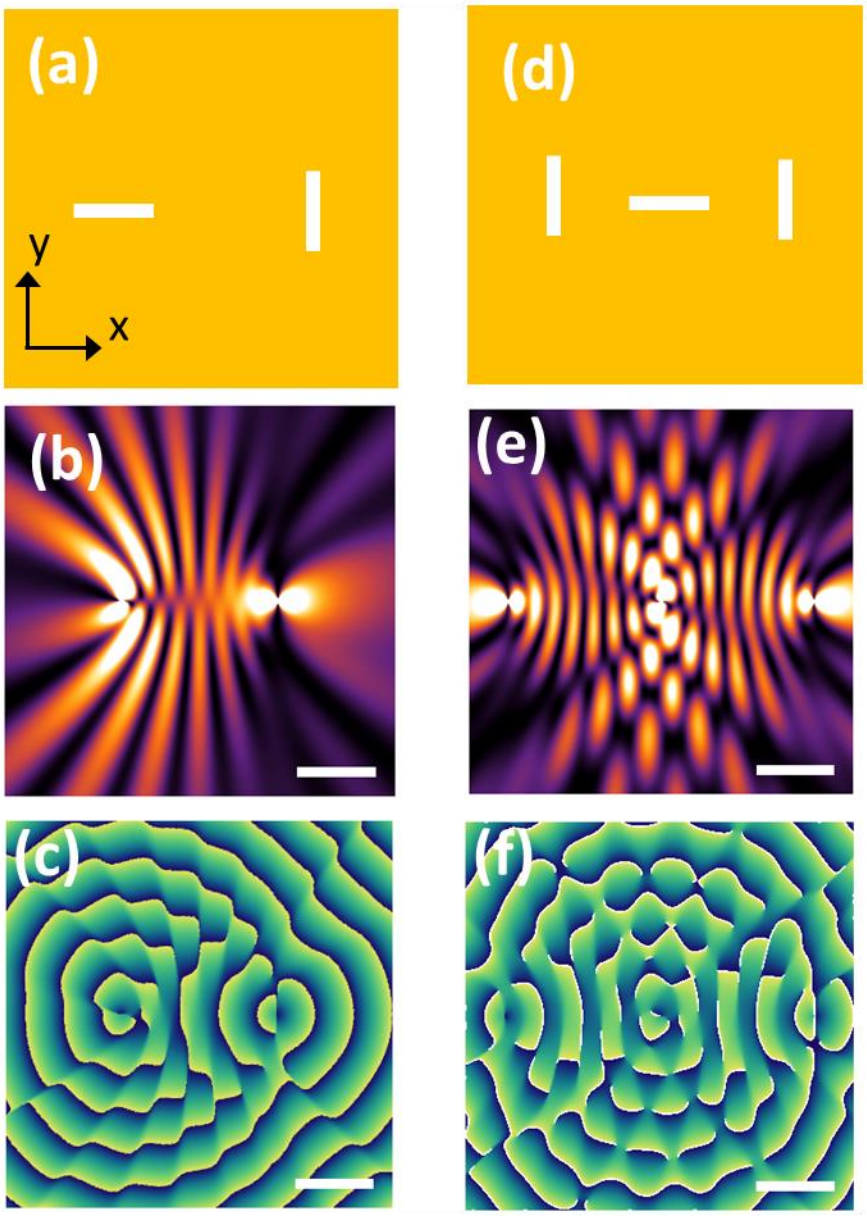

Figure 4-10. (a,d) Schematic of two (three) nano-apertures successively oriented at a 90° angle. (b,e) Intensity and (c,f) phase distributions of the total SPP field of two (a,b,c) and three (d,e,f) straight aperture antennas illuminated by linearly

polarized light and $\frac{\pi}{2}$ rotated with respect to each other. The scale bar length in the pictures is $2\lambda_{SPP} = 1.2\mu m$

In the special case of a rotationally symmetric aperture (symmetric cross or circle), illumination with circularly polarized light (E_x and E_y have equal magnitudes and are phase delayed by $\frac{\pi}{2}$) results in a $\frac{\pi}{2}$ phase delay between the SPPs launched along the two directions (for the behavior of elliptically polarized dipoles, for example, see Ref. (*122*)). For this scenario, the intensity and phase distributions are reported in Figure 4-11. The phase of the emitted surface plasmons covers 2π radians around the structure. This results from the transfer of spin angular momentum of light, allowing generation of SPPs with 2π phase coverage along the azimuthal coordinate θ. It is important to stress that even if the phase coverage around the symmetric aperture range between 0 to 2π, the rotation of a symmetric element cannot be used to address a Pancharatnam-Berry phase retardation.

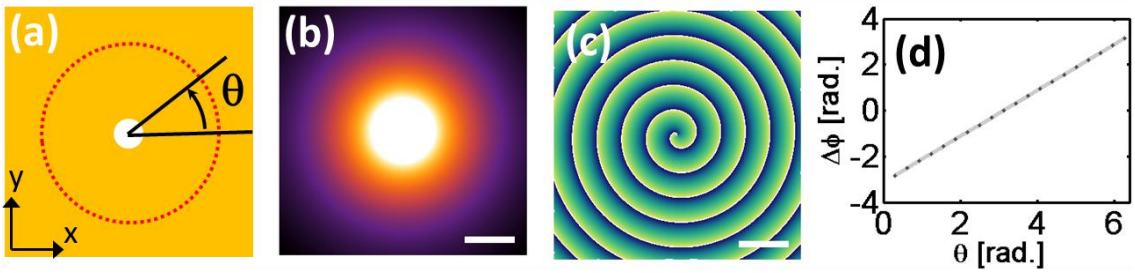

Figure 4-11. (a) Schematic of the metallic nanohole (circular aperture). (b) Calculated intensity at the surface of the metal and (c) phase distributions of the total SPP field of a nanohole illuminated by circularly polarized light. The scale bar length in the pictures is $2\lambda_{SPP} = 1.2\mu m$. (d) Phase of the emitted plasmons along the red circle in (a) as a function of the angle θ.

4.5.2.2 Surface Plasmon Polariton from a Linear Array of Straight Rotated Aperture Antennas

In order to correctly describe the total in-plane SPP field distribution created by a linear array of straight rotated antennas arranged along an axis (Figure 4-12), we need to consider a generalized version of Equation 4-7.

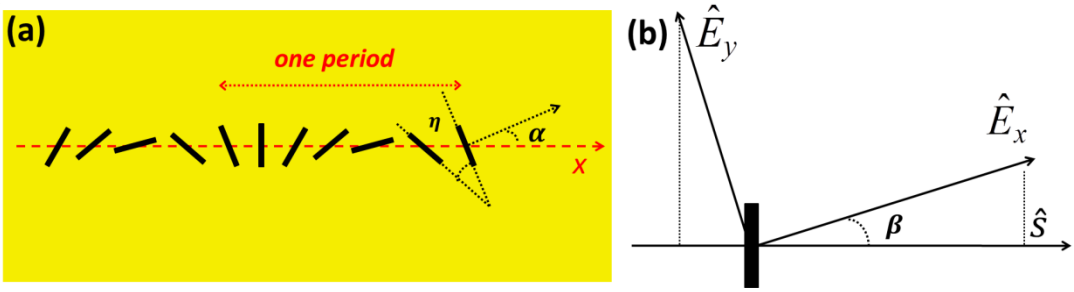

Figure 4-12. (a) Straight aperture antennas rotated by η with respect to each other, whose centers are aligned along the x-axis. (b) Sketch of the orientation of the illuminating electric field components with respect to a generic aperture antenna.

With reference to the axes represented in Figure 4-12b, the electric field of the illuminating plane wave has components along the direction normal to the antenna axis:

Equation 4-8. $\overrightarrow{E_x} \cdot \hat{s} + \overrightarrow{E_y} \cdot \hat{s} = E_{0x} \cos\beta - E_{0y} \sin\beta$

where E_{0x} and E_{0y} are the complex field amplitudes.

In the experiment, the linear polarization of the illuminating beam is changed by means of a quarter waveplate. Accounting for the projection of the incident field onto the x and y axes, the total field in the xy plane due to every antenna excited by an elliptically polarized beam can be summed up as:

Equation 4-9. $E(x,y)_{total} = \sum_i (E_{0x} \cos\alpha_i - e^{j\xi}\, E_{0y} \sin\alpha_i) \frac{e^{jk_{SPP}\left[(x-x_i)^2+(y-y_i)^2\right]^{\frac{1}{2}}}}{\left[(x-x_i)^2+(y-y_i)^2\right]^{\frac{3}{4}}} \left[(x-x_i)\cos(\alpha_i) - (y-y_i)\sin(\alpha_i)\right]$

Where: $E_{0x} = \left|\tilde{E}_{0x}\right|; E_{0y} = \left|\tilde{E}_{0y}\right|; \xi = Arg[\tilde{E}_{0x}] - Arg\left[\tilde{E}_{0y}\right]; j = \sqrt{-1}.$

Equation 4-9 correctly describes the field produced by a single straight aperture antenna. Note that the schematic in Figure 4-12(b) describes the case $\alpha = 0$. The field emitted by an array, as presented in Figure 4-12(a), is obtained by considering a linear superposition of the field created by each individual antenna oriented as in Figure 4-12. For the purpose of explaining the linear phase relationship between the rotation angle of the antenna and the phase delay of the radiated surface plasmons, one can simplify Equation 4-9 to the case of a single antenna placed in $x_i = y_i = 0$. In this conditions the field at a generic point on the y-axis ($x = 0$) is proportional to $e^{\mp j\alpha} \sin \alpha$. This case is presented in Figure 4-13 andFigure 4-14, confirming that for circularly polarized light, the phase retardation is directly given by the rotation angle of the antenna and is modulo π.

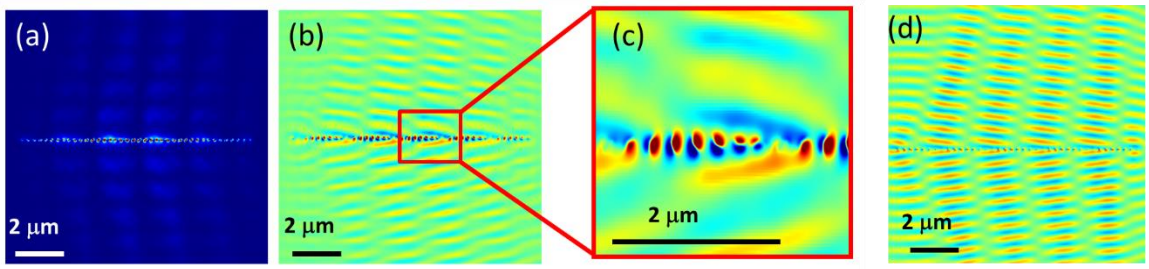

Figure 4-13. (a) FDTD simulation of the intensity distribution of the SPP excited by a 2 μm period array of 8 rotated antennas. (b) Real part of the out of plane E_z field distribution. (c) Zoomed in picture of the real part of E_z, showing that the phase at the antenna axis rotates from 0 to π in a period. All values are taken at 5 nm above the gold film. (d) Analog of (b) but from the analytical model described by Equation 4-9.

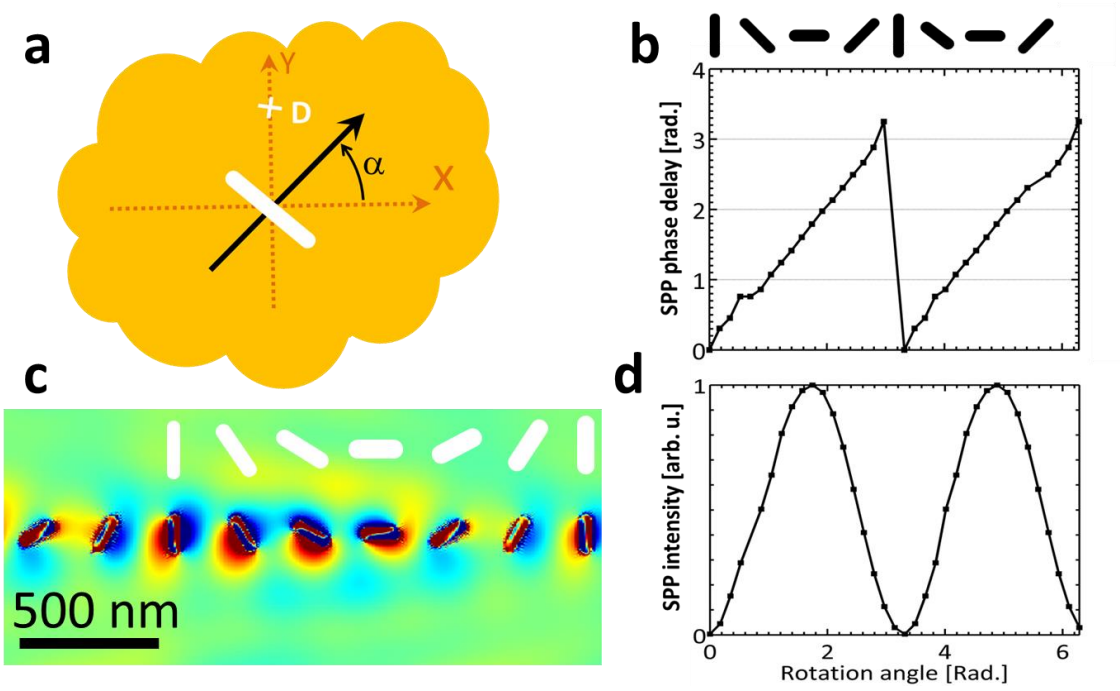

Figure 4-14. a) Schematic of the antenna modeled using FDTD, with the amplitude and phase monitored at point D. b) SPP phase delay relative to the circularly polarized reference beam at point D as a function of rotation angle α of the antenna. The phase delay results are modulo π. c) Real part of the out-of-plane electric field for an array of linear aperture antennas. This is useful to visualize the dipole-like emission of the SPP from each antenna and the relative phase accumulated along the line of antennas. d) SPP intensity monitored at point D as a function of rotation angle α. The normalized intensity varies from 0 to 1 as the projection of the incident electric field changes from parallel to the slit axis to perpendicular to the slit axis.

We confirmed the predictions of the analytical model (intensity and phase distribution) by performing full electromagnetic wave FDTD simulations. An example of the obtained simulations is presented in Figure 4-14 and is in excellent agreement with the analytical model described above.

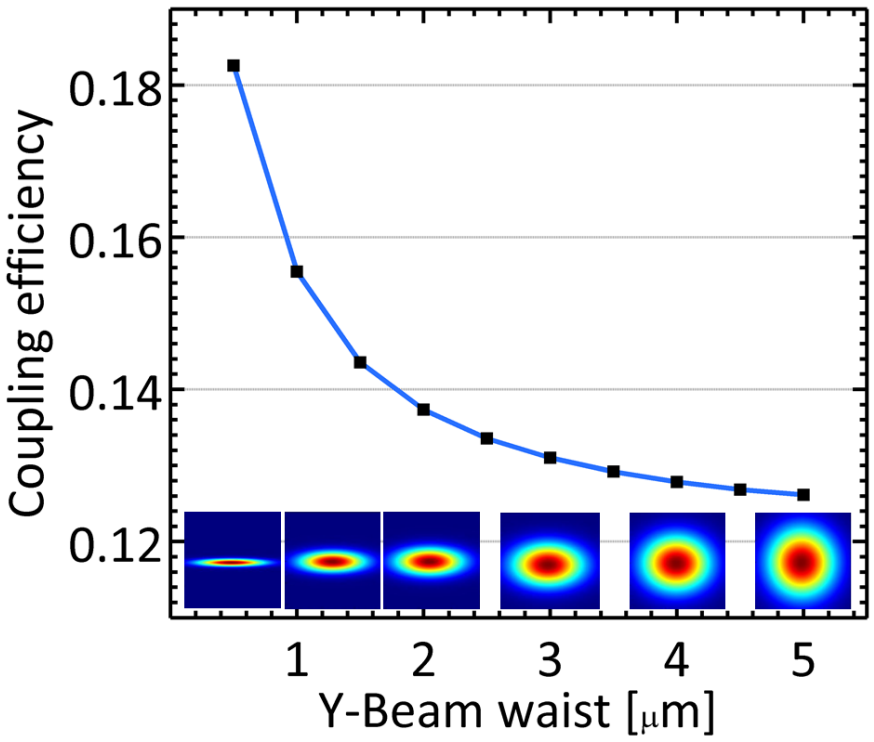

Figure 4-15. Coupling efficiency calculated numerically as a function of beam waist. Four periods of antennas with $\Gamma = 1.5\ \mu m$ is excited by a Gaussian beam. Efficiency is calculated by monitoring the reflection and transmission and calculating $C = 1 - R - T$. Changing the beam waist shows that the efficiency of the device can potentially be doubled.

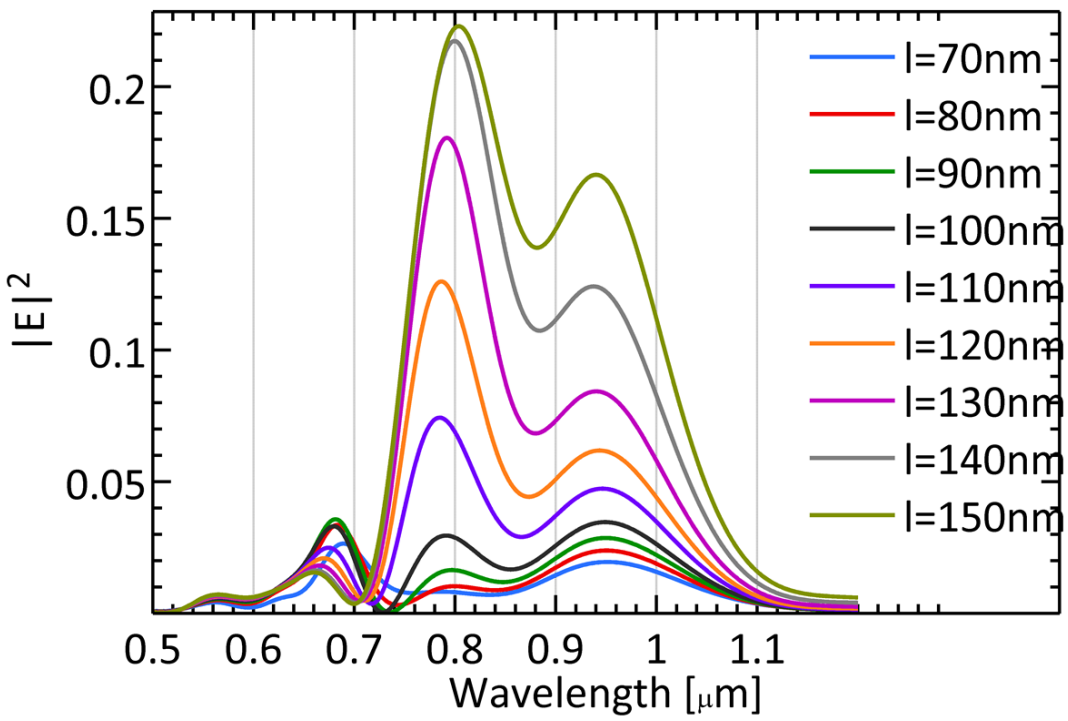

Figure 4-16. In-plane electric field perpendicular to a nanoslit of various lengths as a function of wavelength. This highlights a potential method to increase the device efficiency by utilizing a plasmonic resonance.

4.5.3 NSOM Imaging of the Surface Plasmon Polariton Wakes

When the metallic film is thin enough, the incident beam transmits through the film and can interfere with the in-plane components of the SPP. This results in the fringe pattern that we observed in our experiment—the interferogram. In fact, even though the in-plane components of the SPPs are weaker than the out-

of-plane one, when the NSOM is operated in collection mode with a coated tapered fiber, the NSOM preferentially detects the in-plane components of the surface waves as reported and discussed elsewhere (*120, 123*), and proved by the excellent agreement between our experimental data and simulations reported in the main text.

Our NSOM microscope is the Multiview 4000 from Nanonics Ltd. The probe is an Au-coated bent tapered optical fiber mounted on a tuning fork. The tip-to-sample stabilization is provided by normal-force monitoring. Photons coupled into the fiber from the near-field region are detected by means of a Single Photon Avalanche Diode (SPAD) by MPD S.r.l.

Chapter 5

Asymmetric Surface Plasmon Generation with a Bimodal V-antenna Based Metastructure

ABSTRACT

V-shaped nanoantennas are among the popular choices for the unit element of a metasurface, a nanostructured surface used for its ability to mold and control the wavefront of light. In general, the motivation for choosing the V-antenna as the unit element comes from its bimodal nature, where the introduction of the second mode offers extra control over the scattered wavefronts. Here, through near-field scanning optical microscopy, we study a 1D metastructure comprised of V-antennas in the context of generating asymmetric surface plasmon polariton

(SPP) wavefronts. The key point is that the use of the V-antenna allows for the creation of a two-dimensional phase gradient with a single line of antennas, where the extra phase dimension offers additional control and allows for asymmetric features. Two different asymmetries are created — 1) SPP wavefronts that have different propagation directions on either side of the metastructure, and 2) SPP wavefront asymmetry through focusing: one side of the metastructure focuses SPP wavefronts while the other side has diverging SPP wavefronts.

5.1 Introduction

Surface plasmon polaritons (SPPs) are electromagnetic modes that exist as propagating surface waves bound at the interface of a metal and dielectric. SPP modes offer an alternative to free space propagation, subwavelength energy confinement, and exhibit novel optical phenomena (*57*). As SPPs are 'dark modes' confined to a surface, directly imaging SPPs is difficult and requires probing the near-field component of the electromagnetic field, scattering the energy into a far-field propagating mode. This is most commonly achieved

through near-field scanning optical microscopy (NSOM) (*42, 124*), where a scanning probe tip is brought into the near-field and either scatters the SPPs into free space modes (apertureless, scattering-type NSOM) or into a propagating mode in an optical fiber which is then sent to a detector (aperture, collection mode NSOM).

Metasurfaces (*53, 61, 62*), with their ability to tailor the phase of light on a subwavelength scale, are particularly suited for engineering wavefronts, resulting in optical components such as lenses (*72, 125*), holograms (*86, 90, 92, 126*), and other exotic optical elements (*127-129*). SPP devices based on the phased-array methodology of metasurfaces have also resulted in the creation of SPP lenses (*73, 74, 117, 118*), unidirectional couplers (*35, 75, 130*), and holography based devices (*87, 89, 131*). The design of any optical metastructure is based on two things: the unit element that imparts a phase shift to the incident light, and the phase profile of the desired optical component. In this work, we distinguish two separate cases of asymmetric scattered wavefronts: 1) wavefronts with different propagation directions on either side of the metastructure, and 2)

wavefronts that focus or defocus on either side of the metastructure. To achieve such control, we utilize the Babinet inverse of a V-antenna—a nanoaperture in the shape of a V as our unit element.

V-antennas have received a lot of interest in the field of metasurfaces, including many early works, and have been characterized both in the far-field (*53, 61, 132*) and near-field (*133*). A single V-antenna supports two orthogonal electric dipole modes excited by orthogonal polarizations of light—a symmetric mode and an antisymmetric mode, where the symmetric or antisymmetric refers to the charge oscillation about the axis of the V. It is the existence of the two modes that offers an extra degree of control of the wavefront scattered from the V-antenna relative to a single mode antenna. As such, the bimodal or dual resonance methodology has become commonplace in the field of metasurfaces (*134, 135*). As shown in Ref. (*132*), both the resonant frequency and the scattering cross section of each mode can be independently controlled by tuning the length of the antenna arms and the angle of the V-shaped antennas. In our case, the extra dipolar mode of the V-antenna is used to introduce a two-dimensional phase gradient (in both x

and y) with a single line of phased antennas (1D metasurface), enabling us to achieve asymmetric SPP wavefronts.

5.2 Two-dimensional Phase Gradient

In order to understand the role of the V-antenna in creating asymmetric wavefronts, it is instructive to describe how a two-dimensional phase gradient can induce asymmetry in a wavefront. As a simplest case and proof of concept, consider a line of hypothetical point sources of SPPs, displaced from each other by an amount Δx in the x direction and Δy in the y direction. Determining the resulting wavefronts from the line of SPP sources is a matter of calculating a phase matching condition. Figure 5-1 shows the geometry of the SPP point sources with relevant parameters highlighted. There are two parts that contribute to the phase of the SPPs: 1) the propagation phase, equal to $k_{SPP}\Delta L$ where k_{SPP} is the SPP wavevector, and ΔL is the path length difference between two sources, and 2) a phase difference inherent to the sources themselves (i.e. different initial phases), which we denote as $\Delta\phi$ (the origin of this term is a consequence of the metastructure and is known as the Pancharatnam-Berry

phase, which will be discussed later). From a geometric analysis of Figure 5-1 and some algebra (see Section 5.7.2), the resultant angles of the wavefronts can be derived:

$$\text{Equation 5-1.}\quad \sin\gamma_{1,2} = \frac{1}{k_{SPP}}\frac{\Delta\phi}{\Delta x} \pm \frac{\Delta y}{\Delta x}\cos\gamma_{1,2}$$

where γ_1 and γ_2 are the wavefront angles, k_{SPP} is the SPP wavevector, $\Delta\phi/\Delta x$ is the Berry phase induced phase gradient in the x direction, and $\Delta y/\Delta x$ is the slope of the line that connects the elements, which would be zero for a one-dimensional phase gradient. We note that the wavefront angles appear on both sides of the equation, requiring numerical analysis to solve. Setting $\Delta y/\Delta x$ to zero recovers the symmetric wavefront angle equation from Equation 4-4. The asymmetry in the wavefront angles is a consequence of the sign the $\Delta y/\Delta x$ term

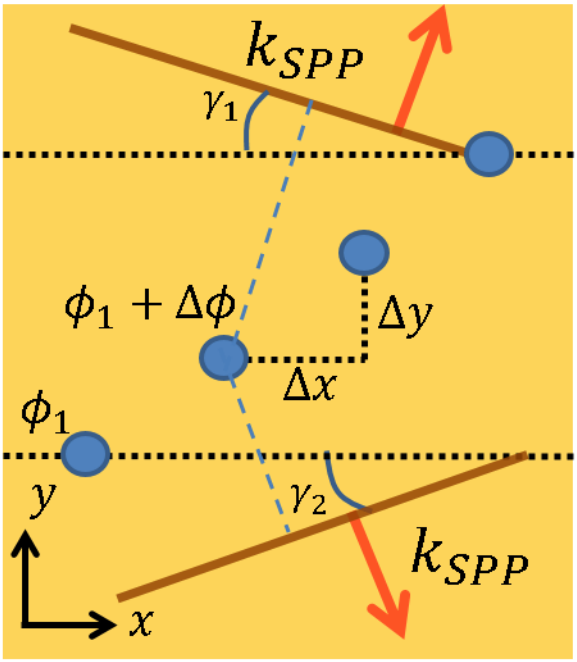

Figure 5-1. 2D phase gradient geometry. Schematic illustrating a phase gradient in two dimensions, resulting in the formation of wavefronts (brown lines) with different angles, γ_1 and γ_2. Hypothetical surface plasmon polariton (SPP) sources (represented by blue circles), are offset in two dimensions by amounts Δx and Δy, with path lengths for the emitted SPPs depicted by the blue dashed lines. Each successive source is dephased from the previous by an amount $\Delta\phi$. Through geometrical analysis and ensuring that the SPPs constructively interfere along the brown lines, the wavefront angles γ_1 and γ_2 can be derived (see Section 5.7.2).

In Chapter 4, a 1D metastructure consisting of sequentially rotated line aperture antennas was used to create symmetric SPP wavefronts, where the wavefront angles were studied and analyzed via NSOM. An analogy was made to 'wakes',

a wave phenomenon that occurs when a disturbance travels through a medium at a velocity faster than the phase velocity of the waves it creates, causing a characteristic buildup that explains the physics behind wakes from boats, Cherenkov radiation, and sonic booms. By choosing a suitable 1D metastructure, the authors were able to create a running wave of polarization along the metastructure with a phase velocity that exceeded the phase velocity of the SPPs, thereby creating SPP 'wakes'.

5.3 Bimodal V-antennas

Instead of using a 1D metastructure consisting of linear antennas, V-antennas allow us to design a two-dimensional phase gradient using a one-dimensional array of rotated antennas. Figure 5-2 illustrates the two modes of the bimodal V-antenna. The symmetric mode (Figure 5-2a) is symmetric about the axis of the V-antenna and can be approximated by a point dipole situated at the center of the V-antenna. The antisymmetric dipole mode (Figure 5-2b), is asymmetric about the axis of the V-antenna and can be approximated by a point dipole at the midpoint of the line connecting the two ends of the arms of the V. Given that the

effective length of the antenna that supports charge oscillation is different for the two modes ($2L$ for the antisymmetric mode and L for the symmetric mode), the modes have different resonance wavelengths. We use finite difference time domain (FDTD) simulations (Figure 5-6 and Figure 5-7) to obtain the scattering amplitude (resonance curve) for a single antenna as a function of wavelength for a given angle Δ and arm length L. We choose the parameters (angle Δ and arm length L) such that both modes have equal scattering amplitudes at a free space operating wavelength of $\lambda_0 = 632\ nm$. Figure 5-2c and Figure 5-2d highlight two different arrangements of sequentially rotated V-antennas. By design, the symmetric mode center always lies on the x axis, whereas the antisymmetric mode, displaced from the symmetric mode, is not constrained to lie on the x axis. This is a key point: the antisymmetric mode traces out a two-dimensional path and is responsible for the two-dimensional phase gradient. Figure 5-2c shows a distribution of antisymmetric mode centers that lie only below the x axis, while Figure 5-2d shows an even distribution of the antisymmetric mode about the x axis.

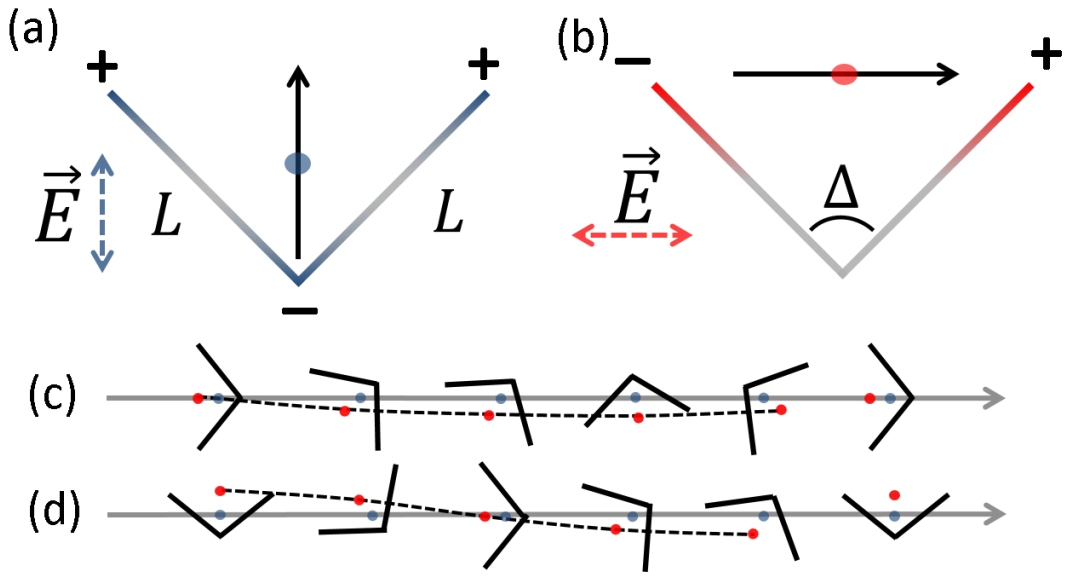

Figure 5-2. Bimodal V-antennas. (a) Symmetric mode of the V-antenna of arm length *L*, excited by light polarized in the direction given by the blue dashed arrow. The mode can be approximated by a single dipole, centered at the blue dot, with dipole moment given by the black arrow. (b) Antisymmetric mode, excited by light polarized in the direction of the red dashed arrow. This mode can be approximated by a single point dipole centered at the red dot, with dipole moment given by the black arrow. Note that the dipole centers of (a) and (b) are displaced from each other in space. (c) and (d) depict two different arrangements of rotated V-antennas, with the red and blue dots corresponding to the positions of the antisymmetric and symmetric modes, respectively. The black dashed lines highlight the spatial displacement of the antisymmetric mode throughout the period, denoting two different types of two-dimensional phase gradients that can be imposed, where (c) highlights an uneven distribution of the antisymmetric mode centers (with respect to the midline, denoted by the grey arrow) and (d) highlights an even distribution. The center of the symmetric mode of each V-antenna is chosen to lie on the midline.

We note that according to FDTD, there is a small scattering amplitude due to the quadrupole mode associated with the asymmetric charge oscillation (as in Figure 5-2b). We incorporate this into the antisymmetric mode as an effective dephasing of the mode, relative to the symmetric mode. The symmetric mode and antisymmetric mode will be displaced spatially by an amount $L/2\cos(\Delta/2)$. To account for the dephasing due to the quadrupole mode, we simply let the geometric separation between the modes vary as a fitting parameter, to be deduced from the experimental data. Thus, the dephasing due to the quadrupole mode is incorporated as a propagation phase, similar to Ref. (*130*). This methodology will also effectively incorporate dephasing due to fabrication imperfections as well.

The origin of the phase gradient is known as the Pancharatnam-Berry phase (*136*). It is a geometric phase accumulated by illuminating sequentially rotated V-antenna apertures with circularly or elliptically polarized light. The x and y components of circularly polarized light are dephased from each other, and this dephasing causes a dephasing in the excitation of the symmetric and

antisymmetric modes—this explains why the modes are excited $\pm\pi/2$ out of phase, depending on the handedness of the polarization. Furthermore, by sequentially rotating the V-antennas, each V-antenna can be dephased from the previous antenna by an amount equal to the rotation.

Consider only the antisymmetric mode centers in Figure 5-2d. If the period of the elements is much bigger than the displacement of the antisymmetric mode from the x axis, the sinusoidal distribution can be well approximated by a line. Hence, Equation 5-1 will accurately describe the wavefront angles. However, the arrangement shown in Figure 5-2c cannot be approximated by a single line, but by two lines of equal and opposite slope (forming a triangle with the x axis). The y direction phase gradient induced by these two lines will cancel out, leaving only the phase gradient in x to describe the wavefront angles, effectively recovering the one-dimensional case.

5.4 Analytical Modeling

In order to understand the behavior of these bimodal antennas, we analytically simulated SPP electric field distributions of such arrangements of bimodal structures. We approximate each mode of each antenna as a point dipole, with a phase dependent on: the mode (symmetric or antisymmetric, excited $\pi/2$ out of phase), and the rotation of the antenna (Berry phase term). Then, the fields of all the simulated dipoles are added together, employing the superposition principle to get the resultant total field. Furthermore, these fields are also added to electric field of the incident Gaussian beam transmitting through the gold, resulting in interference and allowing us to view the interference fringes of the SPPs and the incident light. This is similar to the actual experimental near-field imaging conditions. The simulation results for different cases are presented in Figure 5-3. Figure 5-3a shows the SPP electric field distribution for only the symmetric mode, which lies solely on the x axis. This configuration only has a one-dimensional phase gradient, and thus has symmetric wavefronts with angles given by Equation 5-1 with Δy set to 0. Figure 5-3c shows only the antisymmetric

mode (to isolate the effect of the 2D phase gradient), with a rotation arrangement shown by Figure 5-2d. As can be seen, this arrangement introduces asymmetry into the wavefront angles given by Equation 5-1. However, if the one-sided arrangement of Figure 5-2c is used for the antisymmetric mode, as can be seen in Figure 5-3b, little to no asymmetry in the wavefront angles is recovered because the phase gradient in the *y* direction cancels out. In this case, a focusing effect is seen in the wavefronts below the structure, which is due to the dipoles tracing out a curve. Flipping the handedness of the incident light polarization does not change the side of focusing because this feature only results from the symmetric and antisymmetric dipole positions.

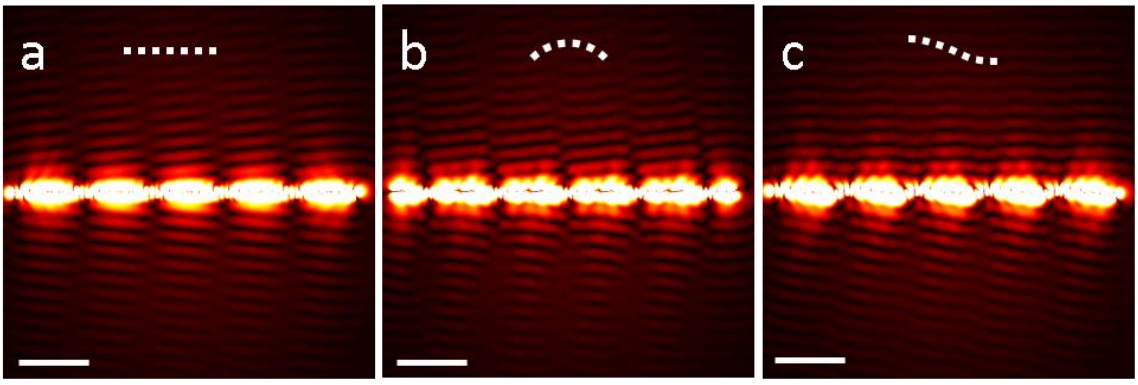

Figure 5-3. Analytical simulations. Results highlighting the different phase gradients that can be created with a phased line of V-antennas. (a) 1D phase gradient, denoted by the white dashed line, resulting in symmetric surface

plasmon wavefronts, for a period of $\Gamma = 3.0\ \mu m$ and left circularly polarized light, where $\gamma_1 = \gamma_2 = 5.8°$. (b) 2D phase gradient, as shown in Figure 5-2c, resulting in nearly symmetric wavefronts (phase gradient in y cancels out along the period) but with a slight focusing effect on the bottom side of the metastructure due to the curvature of the gradient. (c) 2D phase gradient, as shown in Figure 5-2d, which is monotonic decreasing and well-approximated by a line, giving rise to asymmetric wavefronts on either side of the array of V-nanoslits, where the wavefront angles are given by Equation 5-1 as $\gamma_{top} = 2.4°$ and $\gamma_{bottom} = 9.2°$. (b) and (c) use an antisymmetric mode and symmetric mode displacement of $\lambda_{SPP}/6.8$. Scale bar, 3 μm.

5.5 Experimental Setup and Results

To perform experiments, we first e-beam evaporated 50 nm of gold onto a polished silicon substrate, 1 μm thick. We then template strip the gold from the silicon wafer (*107*), using UV curable epoxy (Norland Optics 61) and a glass slide. This is done to reduce the surface roughness of the gold and increase the SPP propagation lengths. Next, we take the gold on glass and use focused ion beam (FIB, Zeiss NVision) to mill the V-antenna apertures into the gold film, with a beam current of 10 pA, with the resulting metastructure shown in the scanning electron micrograph of Figure 5-4a. Next, we mount our sample into a near-field scanning optical microscopy setup. Laser light at 632 nm is incident on the sample from below (transmitting through the glass and gold), and an

NSOM tip scans the top surface containing the metastructure. The NSOM tip is comprised of an atomic force microscopy tuning fork operating in tapping mode with a tapered optical fiber with a diameter of ~150 nm attached. In principle, collecting signal from the near-field allows for sub-diffraction limit imaging, but this is not necessary for our experiment. While scanning the surface in tapping mode, the NSOM tip scatters the SPPs and transmitted laser light into a propagating mode in an optical fiber, which is sent to a single photon avalanche photodiode to record the signal.

Figure 5-4 and Figure 5-5 present near-field scanning optical microscopy data for the focusing 2D gradient (Figure 5-2c) and the asymmetric wavefronts 2D gradient (Figure 5-2d), respectively. Figure 5-4b-d shows the behavior of the structure under different polarizations of the illuminating light. In Figure 5-4c, the 2D focusing effect is most noticeable because there is no phase gradient accumulated along the structure under linearly polarized light, isolating the geometrical effect of the dipole displacements. We find a focal distance from the data: $f = 2.5 \pm .6\ \mu m$, in reasonable agreement with the theoretical value of

2.0 μm (Figure 5-9). The large uncertainty is due to interference—experimental fringes are spaced by λ_{SPP}; the focal distance cannot be known more accurately than λ_{SPP}. Figure 5-5 shows NSOM data from an array of V antennas with a higher scattering cross section for the antisymmetric mode, allowing us to highlight the asymmetric wavefront angles effect. As mentioned earlier, it is beyond the scope of this paper to know the exact effect of fabrication imperfections on the individual V-antenna size (i.e., the ion beam mills wider arms, etc.), and the effect of the antisymmetric quadrupolar mode on the dephasing between the modes. Thus, we estimate from our data that the dephasing between the modes translates to an effective modal separation of $\lambda_{SPP}/6.8$, that is, the positions of the blue and red dots in Figure 5-2a and Figure 5-2b are effectively separated by $\lambda_{SPP}/6.8$ due to dephasing effects.

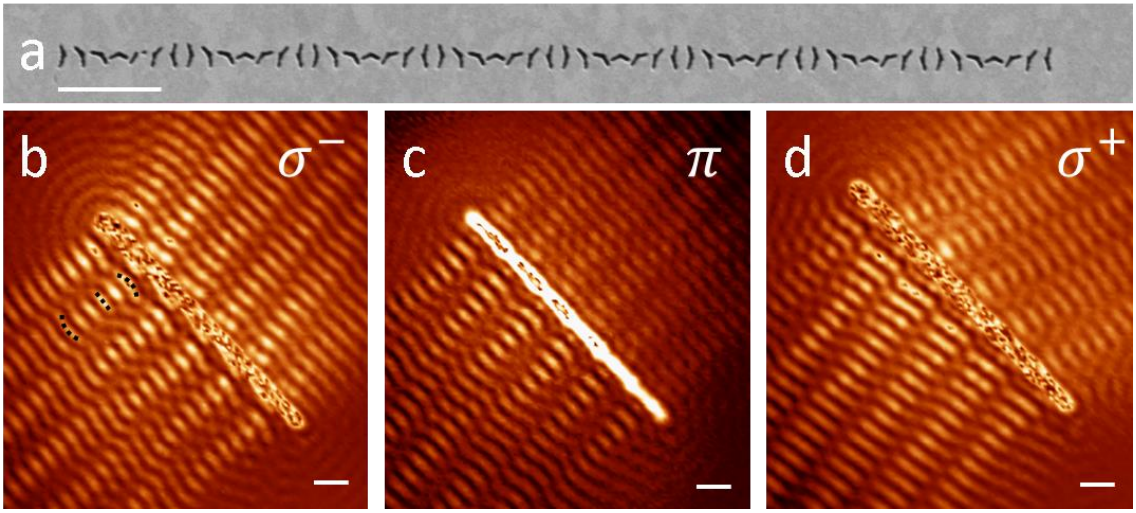

Figure 5-4. NSOM data for the focusing arrangement, scale bar 2 μm. a) Scanning electron micrograph highlighting the focusing 2D gradient, with V antennas with arm length 120 nm and angle of 140° and a period of $\Gamma = 2.0\ \mu m$. b) NSOM data for left circularly polarized light with a focusing effect visible on the left/underside of the structure and wavefront angles dictated by the Equation 5-1 with $\Delta y = 0$. c) NSOM data for linearly polarized light, which serves to further highlight the curved wavefronts due to focusing (highlighted by the black dashed lines)—it is more apparent for linearly polarized light because there is no phase gradient, so the geometrical effect is enhanced. d) NSOM data for right circularly polarized light. Note that the wavefront angles become equal and opposite to those in (b) because the handedness of the light has been reversed.

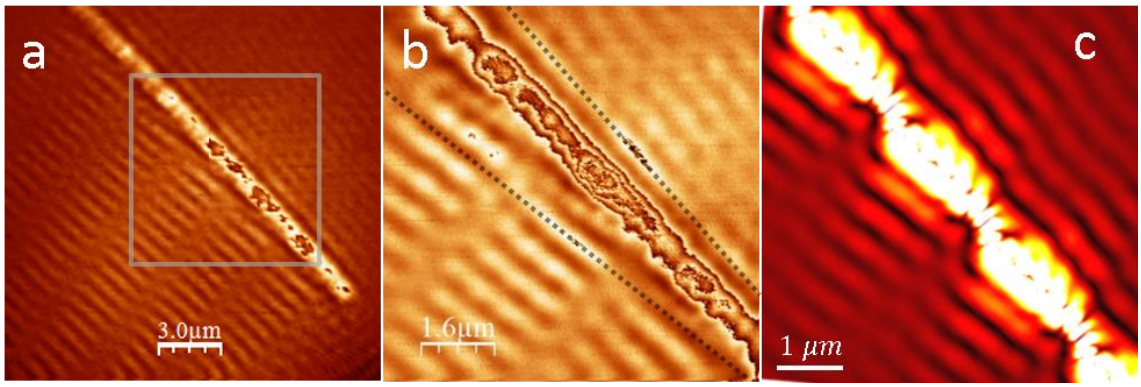

Figure 5-5. NSOM data for V-antennas that produce asymmetric wavefront angles, following the arrangement shown in Figure 5-2d and Figure 5-3c. a) Full-view NSOM data for period $\Gamma = 3.0\ \mu m$ and right circularly polarized light. b) Zoomed in NSOM scan for the area denoted by the grey box in (a). Highlighted by the black dashed lines, the wavefront angle asymmetry is visible on either side of the structure, with measured wavefront angles of $\gamma_1 = 9.2°$ and $\gamma_2 = 2.4°$. Comparison to Equation 5-1 suggests an antisymmetric mode and symmetric mode separation $\approx \lambda_{SPP}/6.8$. c) Analytical simulation of (b) for comparison.

5.6 Conclusion

In this paper, we have studied and shown the effects of using a bimodal unit element in a metastructure, which can be used to induce various anisotropies, namely, focusing or anisotropic effective indices for isotropic media. We use near-field scanning optical microscopy to experimentally measure and verify the induced anisotropies. We demonstrate that this extra mode and 2D phase

gradient can be harnessed to create and control asymmetric surface plasmon wavefronts. As another example of the possible anisotropies, we demonstrate asymmetric focusing/defocusing on either side of such a metastructure. We anticipate this work being used to design more complex and innovative metasurfaces, where the extra control of manipulating a second mode in the unit element can be used for more exotic wavefront control.

5.7 Supplementary Information

5.7.1 Formula for Analytical Simulations

Here we describe the analytical formula used to describe the dipole emission of each mode of the V-antenna, modified from main text References 15, 17, and 27 to include both of the modes of the V-antenna. For the symmetric mode, the electric field is:

Equation 5-2. $$E_s(x,y)_{total} = \sum_i (E_{0x}\cos\alpha_i - e^{j\xi}\, E_{0y}\sin\alpha_i)\frac{e^{jk_{SPP}\left[(x-x_i)^2+(y-y_i)^2\right]^{\frac{1}{2}}}}{\left[(x-x_i)^2+(y-y_i)^2\right]^{\frac{3}{4}}}\left[(x-x_i)\cos(\alpha_i)-(y-y_i)\sin(\alpha_i)\right]$$

and the antisymmetric mode is written as:

Equation 5-3. $$E_a(x,y)_{total} = \sum_i (E_{0x}\sin\alpha_i + e^{j\xi}\, E_{0y}\cos\alpha_i)\frac{e^{j\,k_{SPP}\left[(x-x_i)^2+(y-y_i)^2\right]^{\frac{1}{2}}}}{\left[(x-x_i)^2+(y-y_i)^2\right]^{\frac{3}{4}}}\left[(x-x_i)\cos(\alpha_i+\pi/2) - (y-y_i)\sin(\alpha_i+\pi/2)\right]$$

where: $E_{0x} = \left|\tilde{E}_{0x}\right|; E_{0y} = \left|\tilde{E}_{0y}\right|; \xi = Arg[\tilde{E}_{0x}] - Arg\left[\tilde{E}_{0y}\right]; j = \sqrt{-1}$.

Here, i refers to the antenna index and α refers to the angular orientation. The orthogonality of the modes manifests itself in the projection factor (cos - sin for the symmetric mode and sin + cos for the antisymmetric mode), and in the $\pi/2$ in the final factor (effectively a rotation of the emission of the dipole).

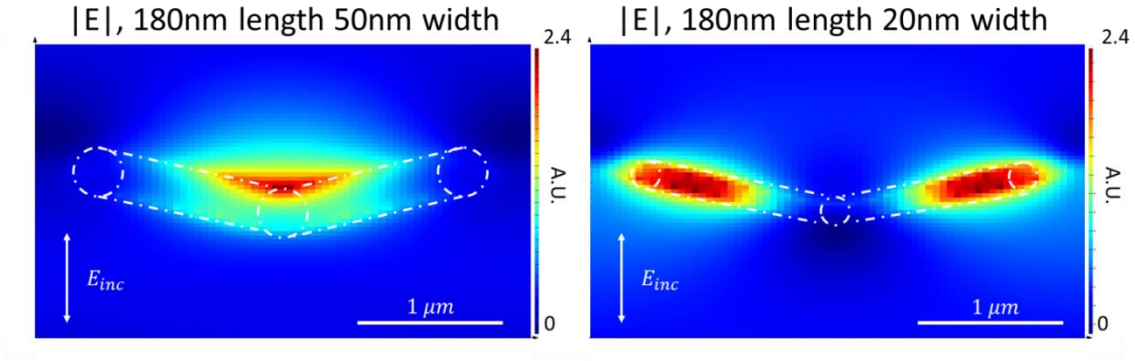

Figure 5-6. FDTD simulations highlighting electric field dependence on the thickness of the V-antenna. A single V-antenna etched into a gold film is simulated using FDTD with 50nm thickness (left) and 20 nm thickness (right). The two plots serve to highlight the necessity of calculating the dephasing

between the modes as a fitting parameter from the data, as the resolution of the FIB milling system can vary, producing different thickness antennas.

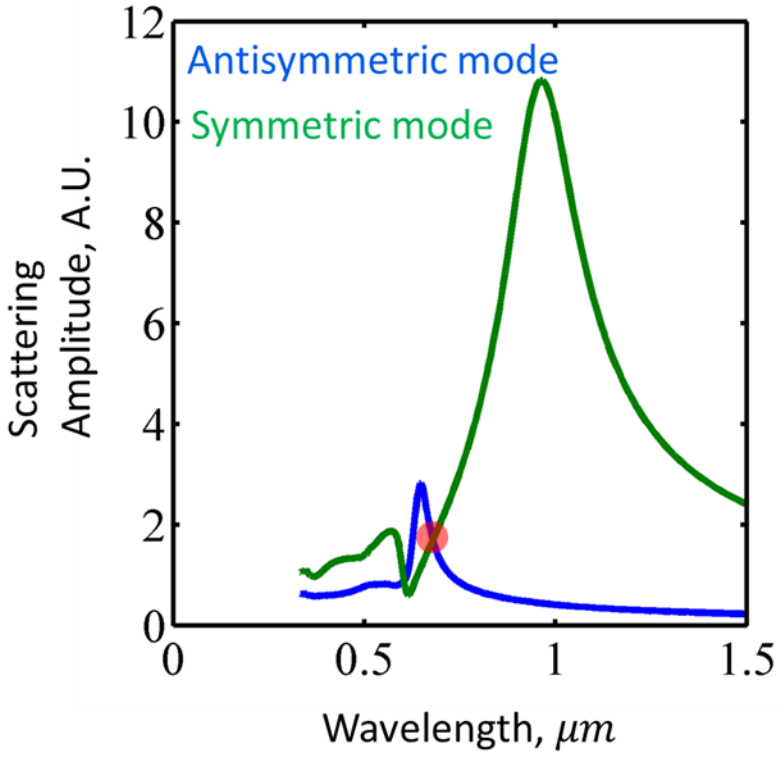

Figure 5-7. Scattering amplitude as a function of wavelength for the two V-antenna modes. FDTD simulations are performed for V parameters of $\Delta = 120°$ and $L = 140\ nm$ for orthogonal polarizations. The simulations suggest the scattering amplitude of both modes is equivalent for roughly 640 *nm*, denoted by the red circle.

5.7.2 Derivation of the Asymmetric Wavefront Angles

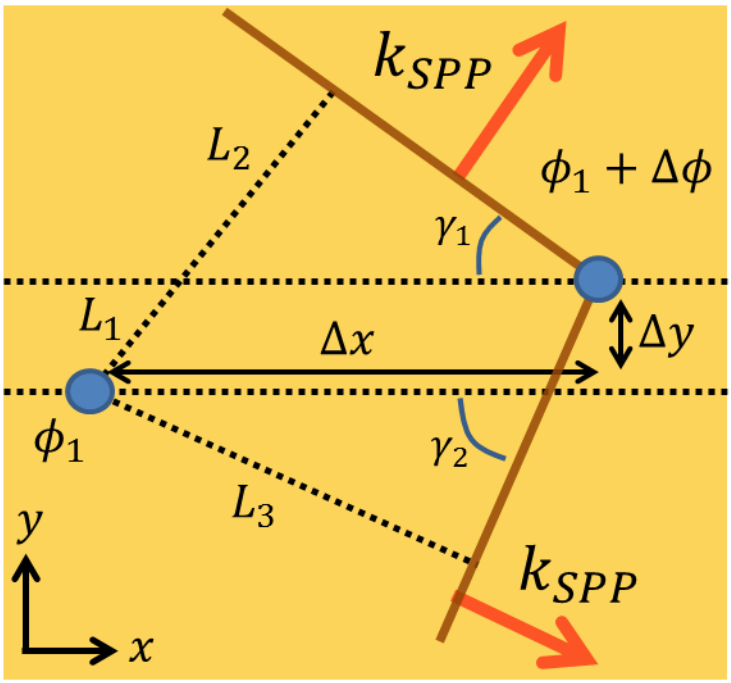

Figure 5-8. 2D phase gradient geometry. Schematic illustrating a phase gradient in two dimensions, resulting in the formation of wavefronts (brown lines) with different angles, γ_1 and γ_2. Surface plasmon polariton (SPP) sources (represented by blue circles), are offset in two dimensions by amounts Δx and Δy. The sources have phases ϕ_1 and $\phi_1 + \Delta\phi$, respectively. Calculating the wavefront angles amounts to setting the phase accumulation for the two sources to be equal: $k_{SPP}(L_1 + L_2) = \Delta\phi$ for γ_1 and $k_{SPP}(L_3) = \Delta\phi$ for γ_2, with results shown in Equation 5-1 in the main text.

5.7.3 Focal Distance Calculation

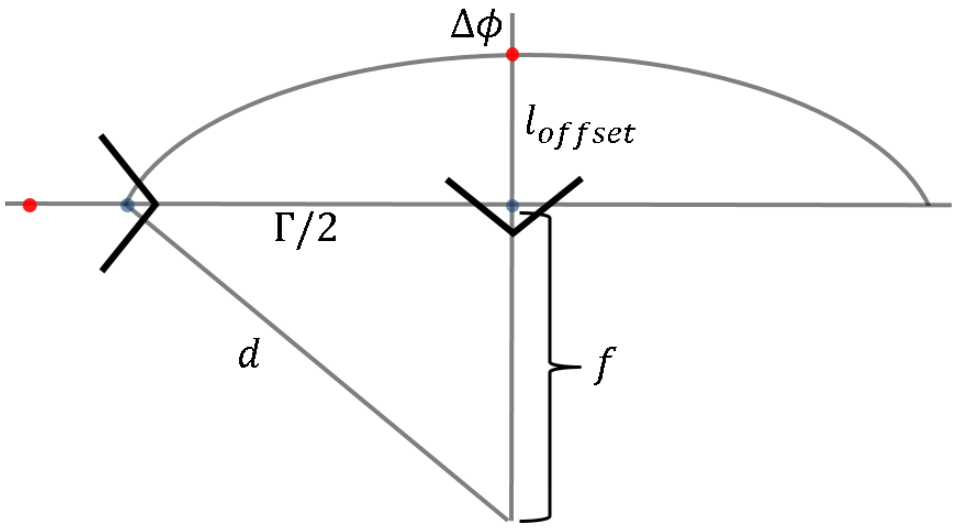

Figure 5-9. Focal distance calculation. Calculating the theoretical focal distance f amounts to a phase matching condition for the two V-antennas. $\Delta\Phi_1 = dk_{SPP}$ and $\Delta\Phi_2 = \Delta\phi + \left(l_{offset} + f\right)k_{SPP}$. Setting the phase accumulations equal and using $d^2 = f^2 + \Gamma^2/4$ allows for the calculation of the theoretical focal distance.

Chapter 6

Refractive Index Measurement of an Anisotropic Dielectric Material Using Near-field Techniques

ABSTRACT

Since the discovery of graphene, 2D materials have garnered significant research interest in the electronics community for their excellent transport properties, amenability to creating heterostructures, and status as a testbed for new physics. In optics, these materials have been used to create exotic photodetectors, and as platforms for surface plasmon polaritons and other hybrid surface waves.

However, an important roadblock remains, largely due to the fact that the extraction of optical constants (namely, the complex index of refraction) for thin, anisotropic, small-area ($< 100\ \mu m^2$), exfoliated flakes is quite difficult, hindering optics-based research. Here, with two near-field scanning optical microscopy (NSOM) experiments, we measure both the in-plane and out-of-plane index of refraction of thin, exfoliated, hexagonal boron nitride (h-BN) for visible frequencies. To do this, we utilize surface waves that probe the h-BN along the lateral dimensions of the flake, rather than the thickness, increasing the interaction length.

6.1 Introduction

Two-dimensional van der Waals materials and heterostructures have been the subject of great research focus and have made great strides in the areas of materials science, condensed matter physics, and nanophotonics (*137-140*). The wide variety of materials (graphene, h-BN, MoS2, etc.), spanning a wide range of conductivities (semimetal, insulator, semiconductor, etc.), makes creating exotic

heterostructures easier and easier as more and more materials are discovered (*141-143*). Recently, for example, black phosphorous has been discovered to have strong in-plane anisotropy, a thickness dependent bandgap, and promising figures-of-merit as a thin film field-effect transistor (*144, 145*).

Two-dimensional materials have interesting optical properties as well, with significant research efforts focused on infrared surface plasmon polaritons (SPPs) and other hybrid surface waves (*146-151*), photodetector devices (*152-154*), strong light-matter interactions (*155*), and exciton studies (*156-158*). However, a roadblock to 2D material optical research is the lack of complex index of refraction data for these thin films. Traditional measurement methods such as ellipsometry prove quite difficult (and/or inapplicable) for such small area flakes, where the ellipsometer beam size is much greater than the size of the flake, creating signal-to-noise ratio issues. Moreover, the need to *a priori* choose the fitting model can prove elusive for newer materials where little is known about their properties. Other techniques, such as high contrast optical microscopy, where exfoliated samples are transferred to a SiO_2/Si substrate and the SiO_2

accentuates the contrast between different thickness flakes through thin film interference, have similar problems—namely the need to use the Fresnel equations and phase differences. Furthermore, given the placement of the flake onto the substrate, measuring the out-of-plane component of the index of refraction requires an out-of-plane component of the electric field, which can severely complicate the optical system required for the measurement.

Here, with two independent experiments, we measure the in-plane and out-of-plane index of refraction for thin film hexagonal boron nitride. Hexagonal boron nitride is ubiquitous in the field of 2D materials, generally used as an encapsulating layer to preserve the quality of other 2D films, or as an insulator (bandgap ~6eV) in heterostructures (*159-161*). Tunable phonon polaritons have also been observed in the mid-IR, and h-BN shows promise as a hyperbolic metamaterial at these wavelengths as well (*146, 150, 162*).

In addition to the above, our choice to study h-BN is two-fold: 1) precise knowledge of h-BN's refractive index is critical to understand the optical

properties of more complex heterostructures, and 2) the large bandgap ensures little to no absorption in the visible ($k \approx 0$), meaning our two experiments can measure the two unknowns, $n_{\perp}$ and $n_{||}$. The methodology of both experiments is equivalent—a surface wave is chosen and h-BN is added to the geometry to alter the dispersion as the surface wave interacts with the modified dielectric environment. The altered dispersion is measured optically using near-field scanning optical microscopy (NSOM), giving information about the effective index of the mode, n_{eff}. Once the effective index and effective wavelength of the mode are measured, we compare the experimental values to finite difference time domain (FDTD) simulations. In the FDTD simulations we sweep a range of index of refraction values for the h-BN. The key point: after the sweep of refractive index values, we find where the simulated effective index matches the experimental effective index, thereby deducing a value for the refractive index of h-BN.

6.2 Standing Wave Mode Experiment for $n_{||}$

Figure 6-1 depicts the experimental setup used in the first experiment. A 300 nm layer of SiO2 is grown on top of a doped Si substrate. A thin film h-BN flake (50 nm) is then mechanically exfoliated directly onto the Si/SiO2 wafer. The 300 nm thick SiO2 supports waveguide modes for visible frequencies. The waveguide modes are altered by the presence of the h-BN flake, as the evanescent tail of the mode will interact with the h-BN, modifying the dispersion. The thickness of the h-BN determines how much electromagnetic energy (modal volume) is contained within the h-BN (Figure 6-5).

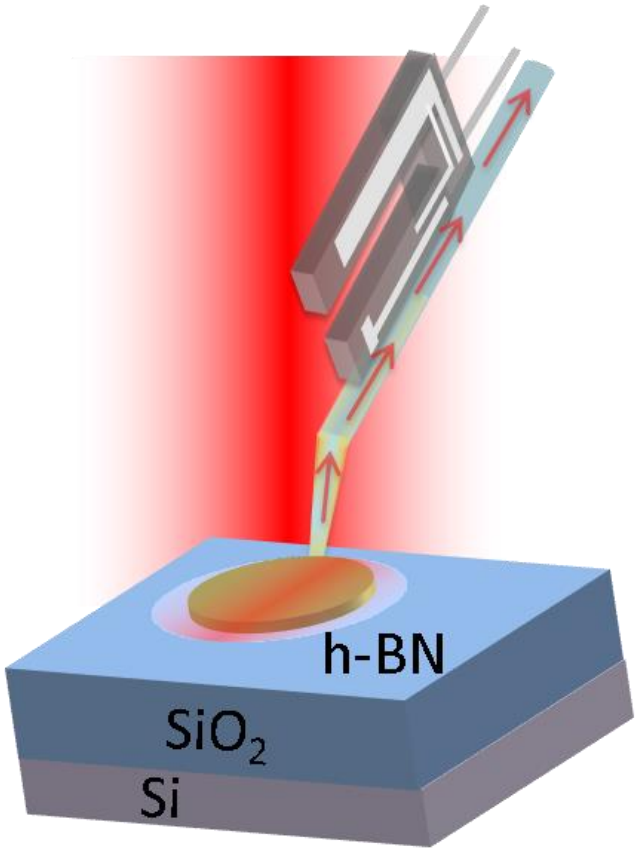

Figure 6-1. Near-field experimental setup to measure the in-plane component of the refractive index. a) Laser light is focused onto the sample from above and illuminates the h-BN disk, thickness 50 *nm*. A portion of the incident light scatters into the standing wave mode supported by the h-BN disk and SiO2 slab. An atomic force microscopy tuning fork with an optical fiber attached (NSOM tip) scans the surface and collects the optical signal. The other end of the optical fiber is attached to an avalanche photodiode (not shown) that records the optical signal.

After the h-BN is exfoliated onto the Si/SiO2 substrate, the h-BN is subsequently etched into a circular pattern using e-beam lithography and reactive ion etching. A regularized geometry is chosen so the structure will support standing wave modes, where the electromagnetic energy is mainly confined in the h-BN (50 nm thick) and partially in the SiO2. These standing wave modes have fringes spaced by the effective wavelength of the mode, which provides information on the overall effective mode index according to: $n_{eff} = \lambda_0/\lambda_{eff}$. As shown in Figure 6-1, polarized laser light is incident and focused onto the sample from above. The source is an NKT Photonics supercontinuum laser with the NKT Select filter, allowing us to choose a single wavelength in the visible range, with our experimental wavelengths ranging from $550 - 700\ nm$ in steps of $25\ nm$. A fraction of this laser light scatters off the edges of the h-BN and into the standing wave modes. To detect the light confined to the h-BN/SiO2 stack, we use collection mode NSOM. Collection mode NSOM is an atomic force microscopy (AFM) tuning fork with a tapered optical fiber attached. As the AFM probe is scanning the surface, the probe and tapered optical fiber interact with the evanescent tail of the standing wave mode (which protrudes into the air above

the h-BN). This interaction of the AFM probe and optical near-field causes some of the electromagnetic energy to scatter into the tapered optical fiber, and that fiber is connected to an avalanche photodiode for photon detection.

Figure 6-2a and Figure 6-2b feature a raw NSOM scan and its Fourier transform, respectively. In Figure 6-2a, the etched circular h-BN on SiO2 region supports standing wave modes, as evidenced by the smaller concentric rings of high intensity inside the h-BN. These rings are spaced by the effective wavelength of the mode, allowing for a straightforward calculation of the effective mode index, $n_{eff} = \lambda_0/\lambda_{eff}$, where λ_0 is the free space wavelength (Figure 6-2a, 650 nm). A region wholly inside the h-BN is selected as depicted by the grey square, and the Fourier transform computed from the selected region (*163*). Next, a radial average is computed from the k-space image, which gives a value for $k_{eff} = 2\pi/\lambda_{eff}$, allowing for effective mode index calculation.

The larger, brighter circular patterns centered at the edge of the h-BN disk in Figure 6-2a come from the focusing of the Gaussian beam. These fringes appear

in the FFT image of Figure 6-2b as a bright partial ring just around the zeroth order component in the center. Figure 6-2c presents an experimental image with periodicities from the Gaussian beam filtered out, with the filtered FFT shown in Figure 6-2d. Experimentally, the fringes in Figure 6-2c are the result of the standing wave mode in the h-BN/SiO2 stack. Figure 6-2c and Figure 6-2d are shown as pedagogical tools to help visualize the mode and pertinent data.

Figure 6-2e shows a full FDTD simulation. The geometry matches that of Figure 6-1, and simulations are performed while sweeping the in-plane refractive index of h-BN. The effective index of the simulation is computed from the fringe spacing and compared to the experimental fringe spacing. Figure 6-2f plots the best fit of the in-plane refractive index such that the simulation effective index matches with the experimental effective index from Figure 6-2a and Figure 6-2c. The dominant mode supported by the h-BN disk is exclusively polarized in-plane with a high extinction ratio much greater than 10: 1 for $|E_{||}|$: $|E_{\perp}|$ inside the disk (Figure 6-6). Thus, the experiment probes only the in-plane component of the refractive index, as both the electric field and magnetic field of the mode are

polarized in plane. The average value of the in-plane refractive index over the wavelength range $550 - 700\ nm$ is $< n_{||} > = 2.07$, in line with previous studies for the refractive index of h-BN in the visible portion of the spectrum (*164*).

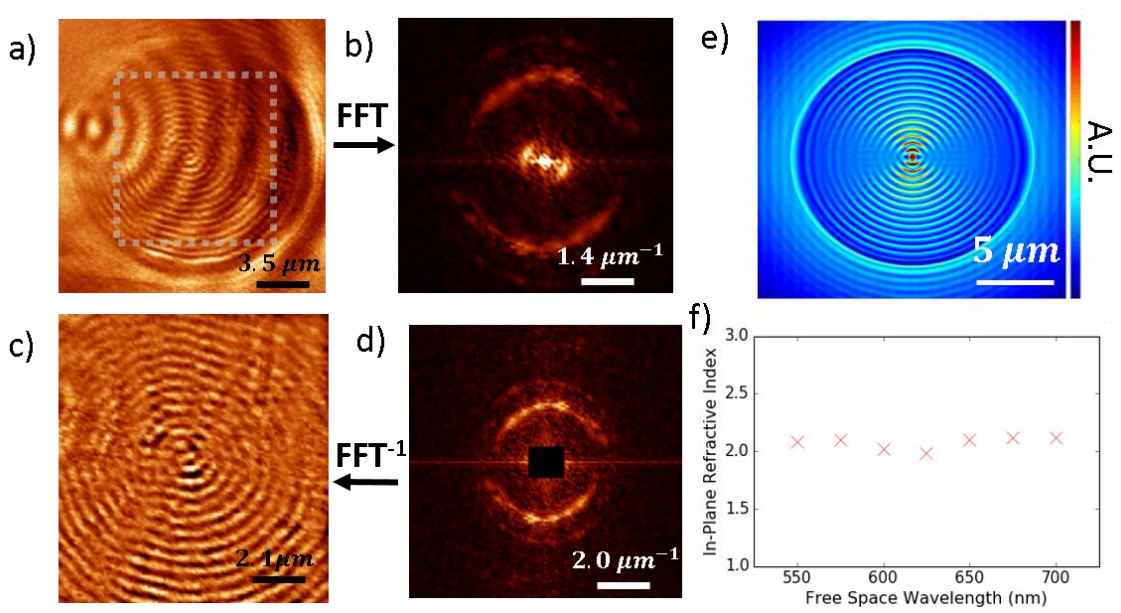

Figure 6-2. Standing wave mode experimental results. (a) Measurement of the optical intensity produced by the standing wave mode for $\lambda = 650\ nm$. The larger fringes with greater inter-fringe spacing are from the focusing of the Gaussian beam. b) Fourier transform of a region inside the disk from (a), denoted by the grey dashed square. The brightest ring around the center corresponds to the fringes produced by the focused beam, and the outer ring corresponds to the magnitude of the wavevector for the standing wave mode. (c) and (d) present the same data as in a) and b) respectively, but with the Gaussian fringes filtered out as a visual aid. e) Finite difference time domain simulation of the h-BN disk, highlighting the standing wave mode, with fringes spaced by $\lambda = \lambda_0/n_{eff}$ where λ_0 is the free space wavelength and n_{eff} is the effective index of the standing wave mode. f) Results for the in-plane refractive index of h-BN as a function of

wavelength. Values obtained by comparing the effective mode index from the experiment to the FDTD simulation mode index.

6.3 SPP Experiment for $n_{\perp}$

Obtaining a value for the in-plane refractive index of h-BN is paramount for the second experiment, which will be used to measure the out-of-plane refractive index of h-BN—using the in-plane data. The second experiment relies on the use of surface plasmon polaritons (SPPs). SPPs are elliptically polarized electromagnetic modes that are confined to propagate at the interface of a metal and a dielectric (refs), with a dispersion relation dictated by the dielectric constants of the dielectric and the metal, $k_{SPP} = k_0\sqrt{\frac{\epsilon_m\epsilon_d}{\epsilon_m+\epsilon_d}}$, where k_{SPP} is the wavevector of the surface plasmon, k_0 is the free space wavevector, ϵ_m is the complex dielectric constant of the metal, and ϵ_d is the complex dielectric constant of the dielectric. However, this dispersion formula only holds when the dielectric is isotropic and semi-infinite. For the case of a thin anisotropic dielectric such as h-BN, the elliptical polarization of the SPPs alters the dispersion relationship, as the polarization has both in-plane and out-of-plane

components, thus probing both the in-plane and out-of-plane dielectric constants. This dispersion relationship, of SPPs in the presence of an anisotropic, finite thickness dielectric, is known (Equation 6-1) (*165*). This is a key point: a measurement of the effective mode index of the elliptically polarized SPPs in the presence of the thin film, anisotropic h-BN will allow for the extraction of the out-of-plane refractive index, if the in-plane refractive index is known. With this methodology, the problem of measuring thin film anisotropic dielectrics is reduced to having two experiments with two unknowns.

Figure 6-3a presents the experimental setup for the near-field SPP experiment. 50 nm of silver is deposited onto a double side polished quartz substrate using an electron-beam evaporator. The double side polished quartz is used to both reduce the roughness of the evaporated silver (increasing SPP propagation length) and to preserve the quality of the laser beam incident through the sample. Next, focused ion beam (FIB) is used to mill a 20 μm long and $\sim$200 nm wide slit into the silver, which will serve as an SPP plane wave excitation source when illuminated with light polarized perpendicular to the slit. 10 nm h-BN is

exfoliated and transferred to the substrate close to the slit using a dry transfer technique (*159*).

Polarized laser light is incident onto the sample from below and focused with a low NA objective onto a FIB milled slit. When light polarized perpendicular to the slit passes through the subwavelength thick slit, the light undergoes diffraction. A portion of the light has a parallel wavevector that matches with the SPP wavevector ($k_{SPP} > k_0$), and can couple into the SPP mode. For the case of a long slit, SPP plane waves are excited with a wavevector perpendicular to the slit. SPPs propagate at the silver/air interface and encounter a refractive index change at the silver/h-BN/air interface, where a fraction of the SPPs are reflected. For the SPPs that continue propagating, their dispersion and effective mode index are altered by the presence of the h-BN. Figure 6-3b presents experimental data for $\lambda_0 = 675\ nm$. First, it is important to note a major difference between the two experiments: the interference fringes here are produced from the interference of the propagating SPPs and the laser light that is transmitted through the $50\ nm$ of silver. The laser light is focused in the plane of

the sample such that the incident light has a flat wavefront and interferes with the propagating SPPs, producing fringes of high intensity where the SPPs and incident light constructively interfere. SPPs are TM modes that have a component of their electric field that is parallel to the SPP wavevector, which is also parallel to the electric field of the incident light (polarization perpendicular to the slit). This interferometric method will produce fringes spaced by the SPP wavelength, λ_{SPP}. By design, this allows for the retrieval of phase information rather than just intensity information; in fact, the NSOM tips used in this experiment preferentially detect the in-plane component of the electric field intensity.

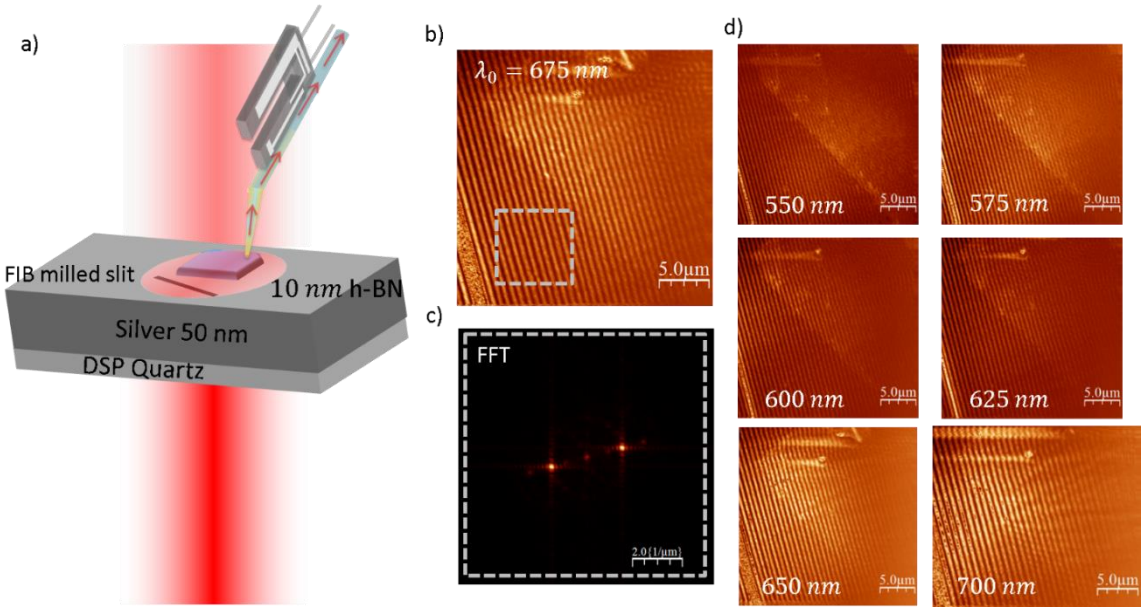

Figure 6-3. Surface plasmon polariton experiment and data. (a) Experimental setup. Laser light is focused onto the sample from below, where a fraction transmits through the optically thin silver. The polarization of the light is chosen to be perpendicular to the FIB milled slit to excite SPP plane waves. SPP waves propagate and interact with the h-BN. An NSOM tip scans the surface and records the optical signal. (b) NSOM data for $\lambda_0 = 675\ nm$. The slit is positioned in the bottom left corner (not fully pictured) where the optical signal on the detector saturates. The 10 nm h-BN flake is visible towards the middle and right side of the image, as depicted in (a), where the contrast changes. The dashed square in (b) denotes the portion of the image shown in the Fourier transform (c). The peaks represent the SPP fringes at the silver/air interface. (d) NSOM images for the remaining wavelengths, $550 - 700\ nm$.

To extract the information produced by the interference fringes, a 2D Fourier transform can be performed to calculate k_{SPP} in the silver/h-BN/air stack. The Fourier transform peaks in Figure 6-3c correspond to spatial frequencies

associated with waves of the form: $e^{\pm ik_{SPP}x}$, and the effective mode index can be calculated according to the relation $n_{eff} = k_{SPP}/k_0$ after a radial average is taken of the k-space image. Once the effective mode index is calculated for each wavelength, the results are compared to Lumerical's FDTD mode solver. The h-BN is treated as a user-input custom anisotropic dielectric, with the in-plane data imported from the previous experiment (Figure 6-2f). Out-of-plane refractive index results are obtained by sweeping only the out-of-plane refractive index of h-BN to find a match with the experimental results from Figure 6-3.

There are two non-obvious sources of error in the SPP experiment that we can calibrate out. The excitation laser has a bandwidth of approximately $10 - 15\ nm$. One source of error is the fact that SPP propagation length is frequency dependent. For higher frequencies closer to the plasma frequency, the free electrons in the silver have correspondingly less time to react because of the shorter period (higher frequency) of the incident electromagnetic field, and more of the incident electromagnetic field to extends into the silver. As such, higher frequencies have lower propagation lengths as more of the mode volume lies in

the lossy silver. The opposite is true for lower frequencies, which experience higher propagation lengths. Therefore, as the SPPs propagate, the lower wavelengths in the bandwidth of the laser are selectively absorbed more than the higher wavelengths. With the lower wavelengths absorbed more, the measured λ_{SPP} is shifted to higher values. This artificially higher λ_{SPP} causes a reduction in the measured effective mode index by virtue of the relation: $n_{eff} = \lambda_0/\lambda_{SPP}$. The other source of error comes from the focusing of the incident beam onto the sample. If the beam is perfectly focused into the plane of the sample, the wavefront of the incident light will be flat as it interferes with the propagating SPPs. This scenario produces sinusoidal interference fringes with high intensity peaks where the SPPs and the flat incident wavefront are in phase, with the fringes separated by λ_{SPP}. If, however, the incident beam is not perfectly focused into the plane of the sample, but instead has some curvature to the wavefront, the resulting interference fringes will be spaced by some amount greater than λ_{SPP} (see Section 6.5.1 and Figure 6-10).

We compensate for these systematic errors by calibrating at every wavelength using the SPP fringe spacing on the silver/air interface. The calibration factor is calculated by computing the ratio of the measured λ_{SPP} to the value predicted by theory using published data for thin film silver (*166*). The average value for the correction factor is 1.03 and the standard deviation is $< .01$. All correction factors are > 1 as well, indicating a systematic 3% increase in measured λ_{SPP} as compared to the expected value from theory.

6.4 Results

The in-plane and out-of-plane refractive index data are presented in Figure 6-4. Over the wavelength range $550 - 700\ nm$, $< n_{\perp} > = 1.87$ and $< n_{||} > = 2.07$. We find that both the in-plane and out-of-plane refractive indices have a minimum that occurs at $\lambda_0 = 625\ nm$. We believe this is due to defects in the h-BN crystals, which have been shown to strongly absorb light at $625\ nm$ (*167*). Significant absorption from these defects affects the assumption that the dielectric h-BN has no absorption. Qualitatively, the $625\ nm$ absorbing defect will ultimately give a

value for the refractive index that is lower than pure h-BN, as defects preferentially absorb the shorter wavelengths, giving a reduction in n_{eff}.

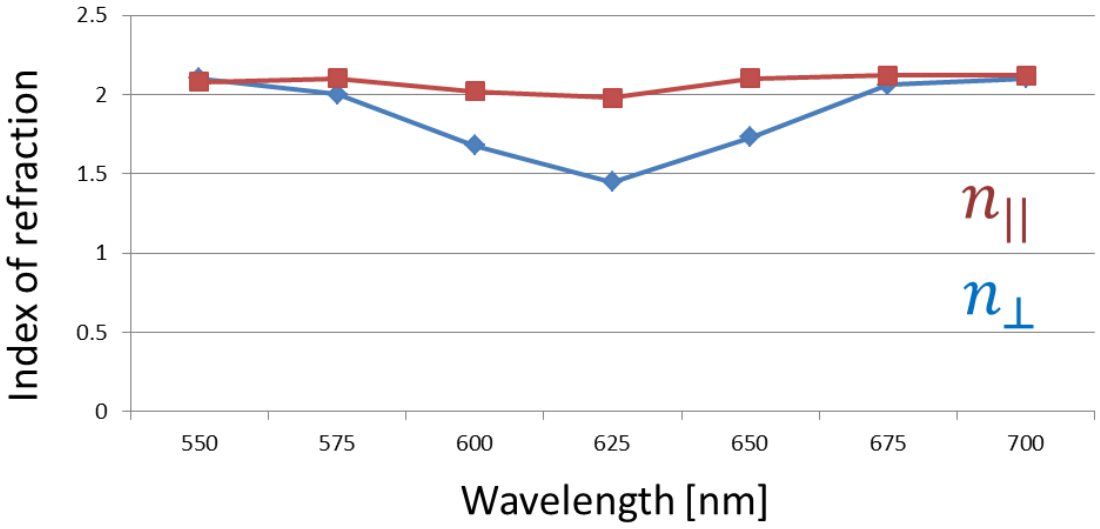

Figure 6-4. Results. In-plane (red) and out-of-plane (blue) refractive index data for thin film, exfoliated h-BN for visible frequencies. The large dip at 625 *nm* for the out-of-plane refractive index is due to defects in the h-BN crystal that absorb at that wavelength (*167*).

In this paper, we have demonstrated a methodology to experimentally measure the refractive index of a thin film, small-area material—traditionally a difficult experiment, even for isotropic materials. We use two experiments to measure two unknowns—the in-plane and out-of-plane refractive indices of hexagonal boron nitride, a major building block in van der Waals heterostructures. The first

experiment utilizes a standing wave mode mostly localized inside h-BN to probe the in-plane component, where the second experiment uses elliptically polarized SPPs to measure the out-of-plane component, using the in-plane component from the first experiment. The strategic material choice of h-BN has two main benefits: previous experiments have shown thin film h-BN to not differ from bulk h-BN too drastically, so the data can be checked against previous experiments, and it paves the way for the measurement of materials that require h-BN encapsulation, such as MoS2, black phosphorous, etc. We anticipate that the knowledge of the optical constants of 2D materials will allow for their use in a wider variety of optics experiments.

6.5 Supplementary Information

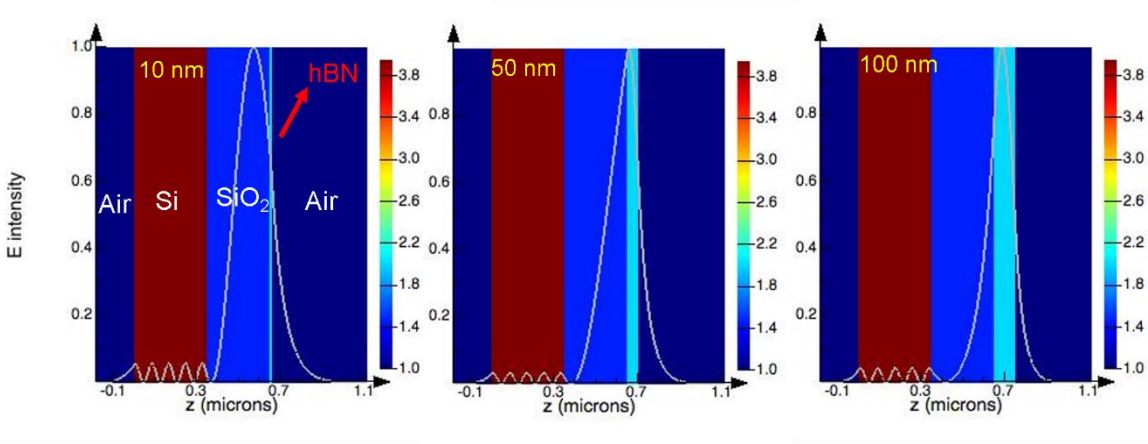

Figure 6-5. 1D mode profile simulations for varying h-BN thicknesses. $10-50-100\ nm$ h-BN thickness simulations (left to right), presented to visualize the modal volume present in the h-BN.

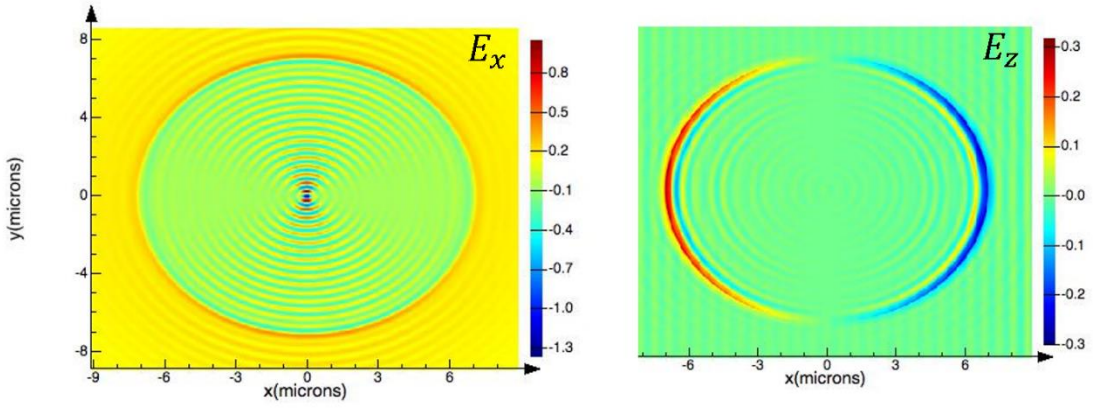

Figure 6-6. Full FDTD simulations at $\lambda_0 = 625\ nm$ highlighting the polarization of the h-BN standing wave mode measured experimentally. E_x (left) and E_z

(right). The only portion of the electric field that is *z*-polarized is the incident light scattering that occurs at the edges of the disk, but inside the h-BN the mode is polarized almost exclusively in-plane.

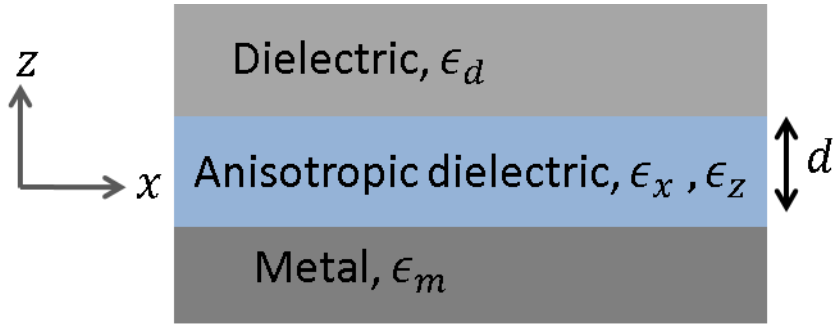

Figure 6-7. Geometry used to derive the dispersion relationship.

From Figure 6-7, the SPP dispersion relationship can be derived by solving Maxwell's Equations, similar to a procedure done in Section 2.2.2.2. Li *et al.* find(*165*):

Equation 6-1.

$$\left(\frac{k_a}{\epsilon_x}+\frac{k_d}{\epsilon_d}\right)\left(\frac{k_a}{\epsilon_x}+\frac{k_m}{\epsilon_m}\right)=\left(\frac{k_a}{\epsilon_x}-\frac{k_d}{\epsilon_d}\right)\left(\frac{k_a}{\epsilon_x}-\frac{k_m}{\epsilon_m}\right)e^{-2k_a d}$$

where k_i refers to the out-of-plane evanescent wavevector of the i^{th} medium, ϵ_i refers to the complex dielectric constant of the i^{th} medium (x and z refer to the anisotropic dielectric indices), and d is the thickness of the anisotropic dielectric.

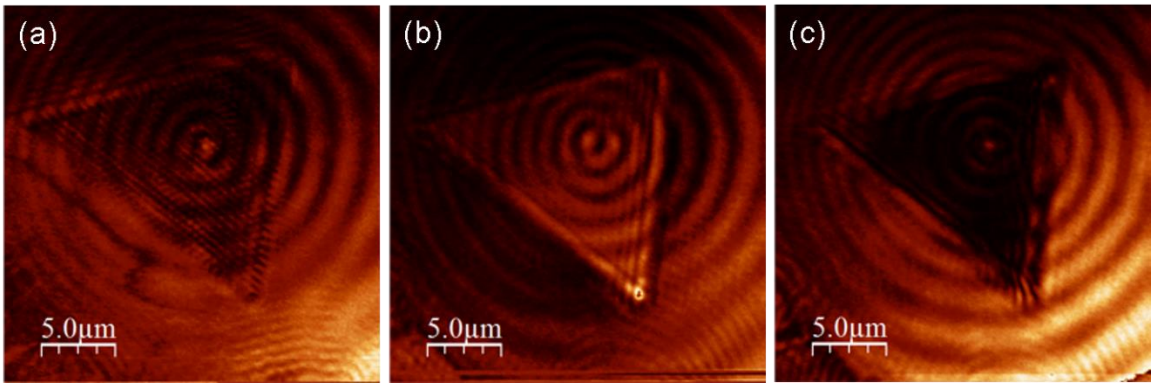

Figure 6-8. Standing wave mode is near-field. Triangular h-BN is illuminated and scanned at various probe heights. (a), roughly 10 *nm*, (b) 60 *nm* and (c) 110 *nm*. Standing wave fringes are only clearly visible in (a), and completely dark in (c).

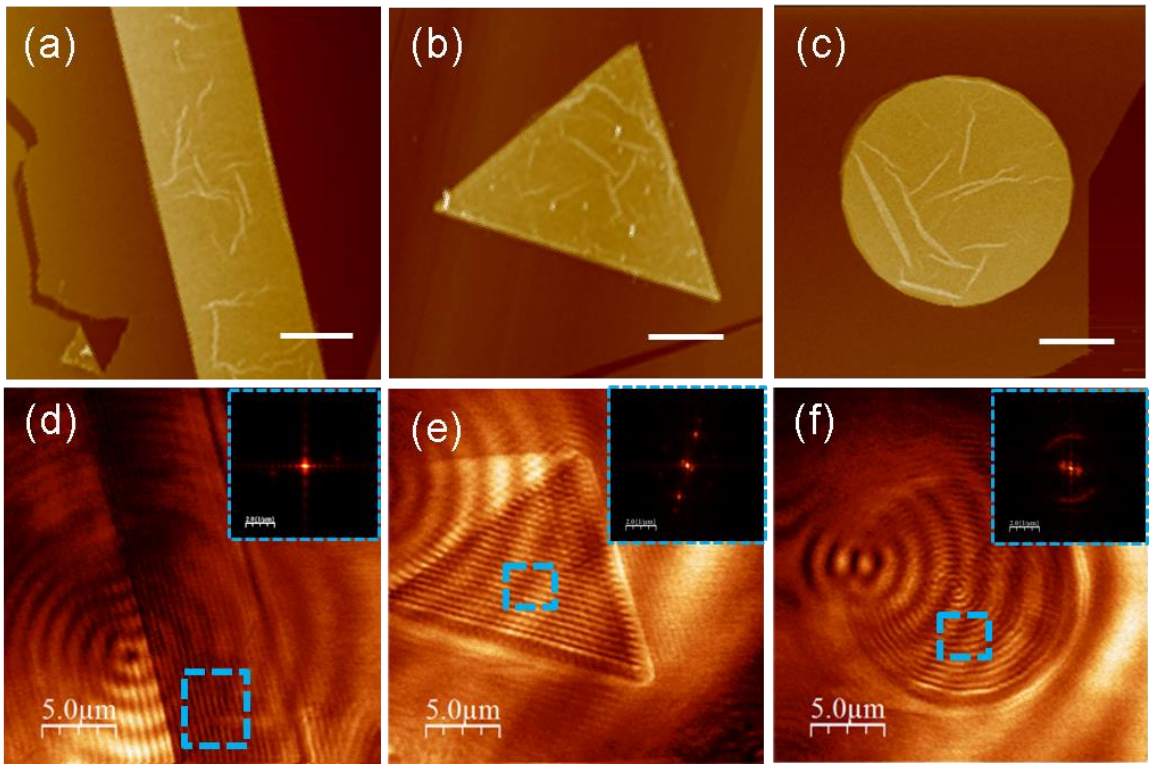

Figure 6-9. Various h-BN geometries. (a-c) AFM topography of samples shown in (d-f). (d-f) NSOM scans, with standing wave fringes visible in all geometries. Insets: Fourier transforms of the areas denoted by the blue rectangles, used for effective index/wavelength analysis.

6.5.1 Interference Fringes

The intereference observed in the SPP experiment comes from the incident light transmitting through the sample and the SPPs that are propagating. If the wavefront of the incident light is flat, e.g. $\phi = \pi/4$ in the plane of the sample, then constructive interference will occur wherever the SPPs have phase $\pi/4$. Bright fringes will be spaced by λ_{SPP}. If, however, the incident wavefront has some curvature, the fringes will be spaced by an amount greater than λ_{SPP}. To see why, let us consider the phase evolution of the incident light and the SPPs. The SPPs accumulate phase as they propagate in the form: $\phi_{SPP} = 2\pi x/\lambda_{SPP}$, and the slope of the line is k_{SPP} (we take $x = 0$ to be the position of the slit). If the impinging light is incident at an angle, the phase accumulated in the plane of the sample will be given by $\phi = 2\pi x \sin\theta\,/\lambda_0 + \phi_0$, where θ is the angular deviation from a flat wavefront and ϕ_0 is the phase relative to the SPPs at $x = 0$. This is the

reason why the fringes are spaced by greater than λ_{SPP} when the incident wavefront is not flat, plotted mathematically in Figure 6-10.

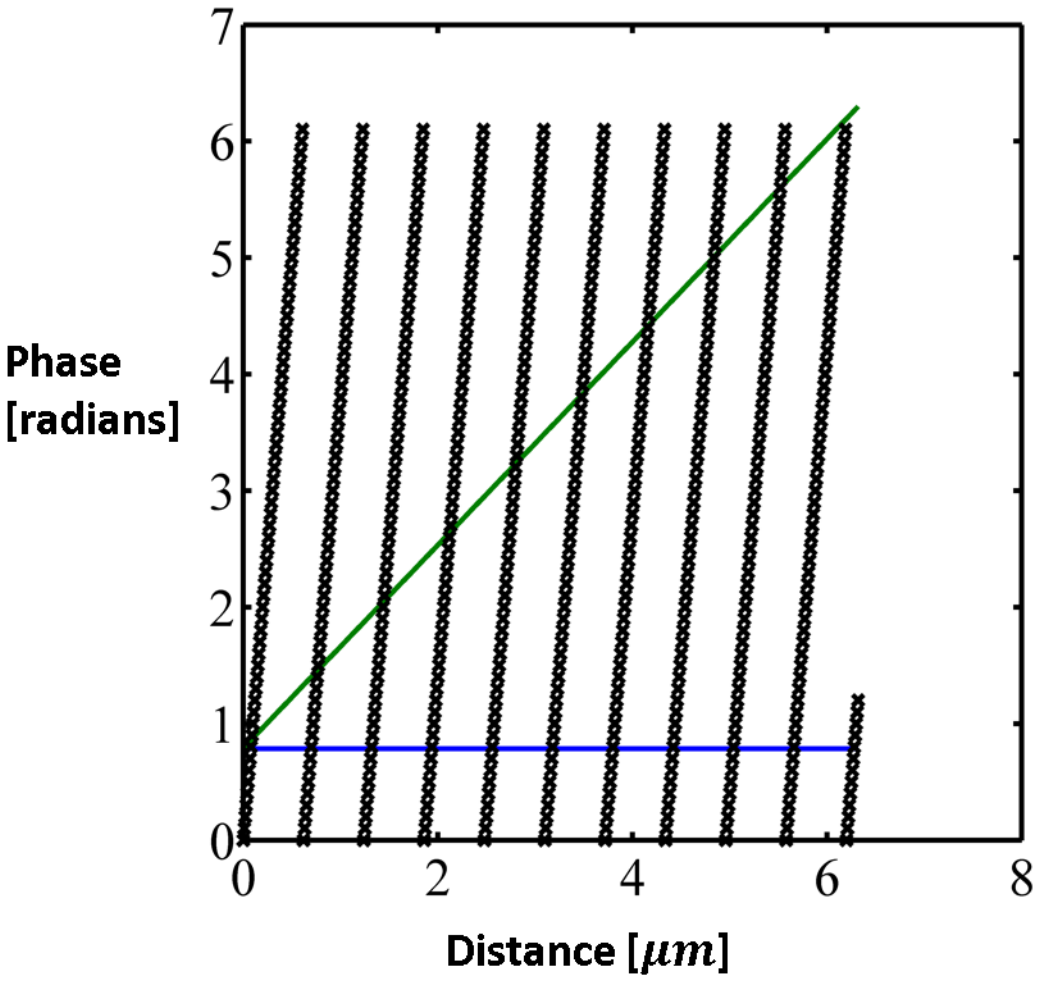

Figure 6-10. Curved wavefront interference. Black Xs plot the phase accumulation (modulo 2π), of the SPPs as they propagate away from the slit at $x = 0$. Blue line highlights the phase of a flat wavefront, and the intersections

with the SPP phase will be the positions of constructive interference. The green line plots the phase accumulation of light incident on the sample at an angle of $\theta = 5°$, with $\phi_0 = \pi/4$. $\lambda_0 = 632\ nm$, $\lambda_{SPP} = 620\ nm$. Geometric considerations prove that the interference fringes for the light incident at an angle must be larger than λ_{SPP}.

Bibliography

1. J. M. Enoch, History of mirrors dating back 8000 years. *Optometry & Vision Science* **83**, 775-781 (2006).
2. G. Sines, Y. A. Sakellarakis, Lenses in antiquity. *American Journal of Archaeology*, 191-196 (1987).
3. T. L. Heath, *The thirteen books of Euclid's Elements*. (Courier Corporation, 1956).
4. A. M. Smith, Ptolemy's Theory of Visual Perception: An English Translation of the" Optics" with Introduction and Commentary. *Transactions of the American Philosophical Society* **86**, iii-300 (1996).
5. S. S. Harlan, The Earth's Magnetism: An Introduction for Geologists. *Eos, Transactions American Geophysical Union* **88**, 123-124 (2007).
6. E. Grant, *A source book in medieval science*. (Harvard University Press, 1974), vol. 1.
7. M. B. Hall, *The scientific renaissance 1450-1630*. (Courier Corporation, 1994).
8. P. Dear, *Revolutionizing the sciences: European knowledge and its ambitions, 1500-1700*. (Palgrave Macmillan, 2008).
9. N. Copernicus, 1543. De Revolutionibus orbium coelestium. *Trans. AM Duncan*, (1995).
10. A. Van Helden, The telescope in the seventeenth century. *Isis* **65**, 38-58 (1974).
11. P. Barker, B. R. Goldstein, Theological foundations of Kepler's astronomy. *Osiris* **16**, 88-113 (2001).
12. J. Kepler, F. Hammer, *Astronomiae pars optica*. (CH Beck'sche Verlagsbuchhandlung, 1939).
13. D. Wintz, Kepler's 1603 remains the only challenger to Einstein's 1905 for the throne of 'best year by a scientist'. (2016).

14. M. S. Mahoney, *The mathematical career of Pierre de Fermat, 1601-1665*. (Princeton University Press, 1994).
15. B. B. Baker, E. T. Copson, *The mathematical theory of Huygens' principle*. (American Mathematical Soc., 2003), vol. 329.
16. B. Franklin, *Experiments and Observations on Electricity, Made at Philadelphia in America by Benjamin Franklin... To which are Added, Letters and Papers on Philosophical Subjects. The Whole Corrected, Methodized... and Now First Collected Into One Volume, and Illustrated with Copper Plates*. (David Henry, 1769).
17. I. Newton, *Opticks, or, a treatise of the reflections, refractions, inflections & colours of light*. (Courier Corporation, 1979).
18. O. S. Heavens, R. W. Ditchburn, *Insight into optics*. (Wiley Chichester, West Sussex,, England, 1991).
19. J. D. Jackson, *Classical electrodynamics*. (Wiley, 1999).
20. A. Sommerfeld, Über die Ausbreitung der Wellen in der drahtlosen Telegraphie. *Annalen der Physik* **333**, 665-736 (1909).
21. J. Zenneck, Propagation of plane EM waves along a plane conducting surface. *Ann. Phys.(Leipzig)* **23**, 907 (1907).
22. H. M. Barlow, J. Brown, *Radio surface waves*. (Clarendon Press, 1962).
23. D. Bohm, D. Pines, A collective description of electron interactions. I. Magnetic interactions. *Physical Review* **82**, 625 (1951).
24. D. Pines, D. Bohm, A collective description of electron interactions: II. Collective vs individual particle aspects of the interactions. *Physical Review* **85**, 338 (1952).
25. D. Bohm, D. Pines, A collective description of electron interactions: III. Coulomb interactions in a degenerate electron gas. *Physical Review* **92**, 609 (1953).
26. R. Ritchie, Plasma losses by fast electrons in thin films. *Physical Review* **106**, 874 (1957).
27. O. Benson, Assembly of hybrid photonic architectures from nanophotonic constituents. *Nature* **480**, 193-199 (2011).
28. P. Drude, Zur elektronentheorie der metalle. *Annalen der Physik* **306**, 566-613 (1900).

29. P. Drude, Zur elektronentheorie der metalle; II. Teil. galvanomagnetische und thermomagnetische effecte. *Annalen der Physik* **308**, 369-402 (1900).
30. N. Ashcroft, N. Mermin, Solid State Physics (Brooks Cole, 1976). *Cited on*, 26.
31. A. Sommerfeld, Zur elektronentheorie der metalle. *Naturwissenschaften* **15**, 825-832 (1927).
32. A. Otto, Excitation of nonradiative surface plasma waves in silver by the method of frustrated total reflection. *Zeitschrift für Physik* **216**, 398-410 (1968).
33. E. Kretschmann, H. Raether, Notizen: radiative decay of non radiative surface plasmons excited by light. *Zeitschrift für Naturforschung A* **23**, 2135-2136 (1968).
34. J. White. (2007).
35. S.-Y. Lee *et al.*, Role of magnetic induction currents in nanoslit excitation of surface plasmon polaritons. *Physical review letters* **108**, 213907 (2012).
36. E. Kretschmann, Die bestimmung optischer konstanten von metallen durch anregung von oberflächenplasmaschwingungen. *Zeitschrift für Physik* **241**, 313-324 (1971).
37. P. B. Johnson, R.-W. Christy, Optical constants of the noble metals. *Physical review B* **6**, 4370 (1972).
38. B. USA.
39. A. D. McFarland, R. P. Van Duyne, Single silver nanoparticles as real-time optical sensors with zeptomole sensitivity. *Nano letters* **3**, 1057-1062 (2003).
40. R. Jorgenson, S. Yee, A fiber-optic chemical sensor based on surface plasmon resonance. *Sensors and Actuators B: Chemical* **12**, 213-220 (1993).
41. M. Fleischmann, P. J. Hendra, A. McQuillan, Raman spectra of pyridine adsorbed at a silver electrode. *Chemical Physics Letters* **26**, 163-166 (1974).
42. L. Novotny, B. Hecht, *Principles of nano-optics*. (Cambridge university press, 2012).
43. E. Synge, XXXVIII. A suggested method for extending microscopic resolution into the ultra-microscopic region. *The London, Edinburgh, and Dublin Philosophical Magazine and Journal of Science* **6**, 356-362 (1928).

44. E. Betzig, A. Lewis, A. Harootunian, M. Isaacson, E. Kratschmer, Near field scanning optical microscopy (NSOM): development and biophysical applications. *Biophysical Journal* **49**, 269 (1986).
45. J. R. Zurita-Sánchez, J.-J. Greffet, L. Novotny, Friction forces arising from fluctuating thermal fields. *Physical Review A* **69**, 022902 (2004).
46. D. R. Turner. (Google Patents, 1984).
47. O. P. Hamill, A. Marty, E. Neher, B. Sakmann, F. Sigworth, Improved patch-clamp techniques for high-resolution current recording from cells and cell-free membrane patches. *Pflügers Archiv* **391**, 85-100 (1981).
48. B. Hecht *et al.*, Scanning near-field optical microscopy with aperture probes: Fundamentals and applications. *The Journal of Chemical Physics* **112**, 7761-7774 (2000).
49. P. Ikonen, Artificial dielectrics and magnetics in microwave engineering: A brief historical revision. *Radio Laboratory/SMARAD, Helsinki University of Technology*.
50. S. John, Strong localization of photons in certain disordered dielectric superlattices. *Physical review letters* **58**, 2486 (1987).
51. J. B. Pendry, Negative refraction makes a perfect lens. *Physical review letters* **85**, 3966 (2000).
52. D. Schurig *et al.*, Metamaterial electromagnetic cloak at microwave frequencies. *Science* **314**, 977-980 (2006).
53. N. Yu *et al.*, Light propagation with phase discontinuities: generalized laws of reflection and refraction. *science* **334**, 333-337 (2011).
54. R. C. Hansen, *Phased array antennas*. (John Wiley & Sons, 2009), vol. 213.
55. R. J. Mailloux, *Phased array antenna handbook*. (Artech House Boston, 2005), vol. 2.
56. M. Khorasaninejad *et al.*, Metalenses at visible wavelengths: Diffraction-limited focusing and subwavelength resolution imaging. *Science* **352**, 1190-1194 (2016).
57. S. A. Maier, *Plasmonics: fundamentals and applications*. (Springer Science & Business Media, 2007).
58. V. M. Shalaev, S. Kawata, *Nanophotonics with surface plasmons*. (Elsevier, 2006).

59. W. L. Barnes, A. Dereux, T. W. Ebbesen, Surface plasmon subwavelength optics. *Nature* **424**, 824-830 (2003).
60. E. Ozbay, Plasmonics: merging photonics and electronics at nanoscale dimensions. *science* **311**, 189-193 (2006).
61. X. Ni, N. K. Emani, A. V. Kildishev, A. Boltasseva, V. M. Shalaev, Broadband light bending with plasmonic nanoantennas. *Science* **335**, 427-427 (2012).
62. N. Yu, F. Capasso, Flat optics with designer metasurfaces. *Nature materials* **13**, 139-150 (2014).
63. N. Yu *et al.*, A broadband, background-free quarter-wave plate based on plasmonic metasurfaces. *Nano letters* **12**, 6328-6333 (2012).
64. A. Pors, M. G. Nielsen, S. I. Bozhevolnyi, Broadband plasmonic half-wave plates in reflection. *Optics letters* **38**, 513-515 (2013).
65. X. Ni, S. Ishii, A. V. Kildishev, V. M. Shalaev, Ultra-thin, planar, Babinet-inverted plasmonic metalenses. *Light: Science & Applications* **2**, e72 (2013).
66. X. Chen *et al.*, Dual-polarity plasmonic metalens for visible light. *Nature communications* **3**, 1198 (2012).
67. M. Kang, T. Feng, H.-T. Wang, J. Li, Wave front engineering from an array of thin aperture antennas. *Optics express* **20**, 15882-15890 (2012).
68. B. Memarzadeh, H. Mosallaei, Array of planar plasmonic scatterers functioning as light concentrator. *Optics letters* **36**, 2569-2571 (2011).
69. X. Li *et al.*, Flat metasurfaces to focus electromagnetic waves in reflection geometry. *Optics letters* **37**, 4940-4942 (2012).
70. A. Pors, M. G. Nielsen, R. L. Eriksen, S. I. Bozhevolnyi, Broadband focusing flat mirrors based on plasmonic gradient metasurfaces. *Nano letters* **13**, 829-834 (2013).
71. F. Aieta, P. Genevet, M. Kats, F. Capasso, Aberrations of flat lenses and aplanatic metasurfaces. *Optics express* **21**, 31530-31539 (2013).
72. F. Aieta *et al.*, Aberration-free ultrathin flat lenses and axicons at telecom wavelengths based on plasmonic metasurfaces. *Nano letters* **12**, 4932-4936 (2012).
73. T. Tanemura *et al.*, Multiple-wavelength focusing of surface plasmons with a nonperiodic nanoslit coupler. *Nano letters* **11**, 2693-2698 (2011).

74. Y.-G. Chen, F.-Y. Yang, J. Liu, Z.-Y. Li, Broadband focusing and demultiplexing of surface plasmon polaritons on metal surface by holographic groove patterns. *Optics express* **22**, 14727-14737 (2014).
75. J. Lin *et al.*, Polarization-controlled tunable directional coupling of surface plasmon polaritons. *Science* **340**, 331-334 (2013).
76. K. Lee, Q.-H. Park, Coupling of surface plasmon polaritons and light in metallic nanoslits. *Physical review letters* **95**, 103902 (2005).
77. F. López-Tejeira *et al.*, Efficient unidirectional nanoslit couplers for surface plasmons. *Nature Physics* **3**, 324-328 (2007).
78. Z. Liu *et al.*, Focusing surface plasmons with a plasmonic lens. *Nano letters* **5**, 1726-1729 (2005).
79. L. Yin *et al.*, Subwavelength focusing and guiding of surface plasmons. *Nano letters* **5**, 1399-1402 (2005).
80. D. Gabor, in *Proceedings of the Royal Society of London A: Mathematical, Physical and Engineering Sciences*. (The Royal Society, 1949), vol. 197, pp. 454-487.
81. Y. N. Denisyuk, in *Soviet Physics Doklady*. (1962), vol. 7, pp. 543.
82. E. N. Leith, J. Upatnieks, Reconstructed wavefronts and communication theory. *JOSA* **52**, 1123-1130 (1962).
83. J. Cowan, The surface ace plasmon resonance effect in holography. *Optics Communications* **5**, 69-72 (1972).
84. S. Maruo, O. Nakamura, S. Kawata, Evanescent-wave holography by use of surface-plasmon resonance. *Applied optics* **36**, 2343-2346 (1997).
85. G. P. Wang, T. Sugiura, S. Kawata, Holography with surface-plasmon-coupled waveguide modes. *Applied optics* **40**, 3649-3653 (2001).
86. P. Genevet, F. Capasso, Holographic optical metasurfaces: a review of current progress. *Reports on Progress in Physics* **78**, 024401 (2015).
87. M. Ozaki, J.-i. Kato, S. Kawata, Surface-plasmon holography with white-light illumination. *Science* **332**, 218-220 (2011).
88. P. Genevet, J. Lin, M. A. Kats, F. Capasso, Holographic detection of the orbital angular momentum of light with plasmonic photodiodes. *Nature communications* **3**, 1278 (2012).
89. I. Dolev, I. Epstein, A. Arie, Surface-plasmon holographic beam shaping. *Physical review letters* **109**, 203903 (2012).

90. X. Ni, A. V. Kildishev, V. M. Shalaev, Metasurface holograms for visible light. *Nature communications* **4**, (2013).
91. F. Zhou, Y. Liu, W. Cai, Plasmonic holographic imaging with V-shaped nanoantenna array. *Optics express* **21**, 4348-4354 (2013).
92. L. Huang *et al.*, Three-dimensional optical holography using a plasmonic metasurface. *Nature communications* **4**, (2013).
93. E. Orabona *et al.*, Holographic patterning of graphene-oxide films by light-driven reduction. *Optics letters* **39**, 4263-4266 (2014).
94. M. Hegner, P. Wagner, G. Semenza, Ultralarge atomically flat template-stripped Au surfaces for scanning probe microscopy. *Surface Science* **291**, 39-46 (1993).
95. W. Thomson, On the waves produced by a single impulse in water of any depth, or in a dispersive medium. *Proceedings of the Royal Society of London* **42**, 80-83 (1887).
96. L. D. Landau *et al.*, *Electrodynamics of continuous media*. (elsevier, 2013), vol. 8.
97. V. G. Veselago, The electrodynamics of substances with simultaneously negative values of and? *Soviet physics uspekhi* **10**, 509 (1968).
98. A. Grbic, G. V. Eleftheriades, Experimental verification of backward-wave radiation from a negative refractive index metamaterial. *Journal of Applied Physics* **92**, 5930-5935 (2002).
99. S. Xi *et al.*, Experimental verification of reversed Cherenkov radiation in left-handed metamaterial. *Physical review letters* **103**, 194801 (2009).
100. S. J. Smith, E. Purcell, Visible light from localized surface charges moving across a grating. *Physical Review* **92**, 1069 (1953).
101. G. Doucas, J. Mulvey, M. Omori, J. Walsh, M. Kimmitt, First observation of Smith-Purcell radiation from relativistic electrons. *Physical review letters* **69**, 1761 (1992).
102. C. Luo, M. Ibanescu, S. G. Johnson, J. Joannopoulos, Cerenkov radiation in photonic crystals. *Science* **299**, 368-371 (2003).
103. K. Casey, C. Yeh, Z. Kaprielian, Čerenkov Radiation in Inhomogeneous Periodic Media. *Physical Review* **140**, B768 (1965).

104. F. G. De Abajo, Interaction of radiation and fast electrons with clusters of dielectrics: a multiple scattering approach. *Physical review letters* **82**, 2776 (1999).
105. G. Adamo *et al.*, Light well: a tunable free-electron light source on a chip. *Physical review letters* **103**, 113901 (2009).
106. F. G. De Abajo, Optical excitations in electron microscopy. *Reviews of modern physics* **82**, 209 (2010).
107. P. Nagpal, N. C. Lindquist, S.-H. Oh, D. J. Norris, Ultrasmooth patterned metals for plasmonics and metamaterials. *Science* **325**, 594-597 (2009).
108. P. Genevet, F. Capasso, Breakthroughs in Photonics 2013: Flat Optics: Wavefronts Control With Huygens' Interfaces. *IEEE Photonics Journal* **6**, 1-4 (2014).
109. P. Genevet *et al.*, Ultra-thin plasmonic optical vortex plate based on phase discontinuities. *Applied Physics Letters* **100**, 013101 (2012).
110. N. Shitrit, S. Maayani, D. Veksler, V. Kleiner, E. Hasman, Rashba-type plasmonic metasurface. *Optics letters* **38**, 4358-4361 (2013).
111. N. Shitrit, I. Yulevich, V. Kleiner, E. Hasman, Spin-controlled plasmonics via optical Rashba effect. *Applied Physics Letters* **103**, 211114 (2013).
112. N. Shitrit *et al.*, Spin-optical metamaterial route to spin-controlled photonics. *Science* **340**, 724-726 (2013).
113. Z. Duan, B.-I. Wu, J. Lu, J. A. Kong, M. Chen, Reversed Cherenkov radiation in a waveguide filled with anisotropic double-negative metamaterials. *Journal of Applied Physics* **104**, 063303 (2008).
114. S. Sun *et al.*, Gradient-index meta-surfaces as a bridge linking propagating waves and surface waves. *Nature materials* **11**, 426-431 (2012).
115. S. Sun *et al.*, High-efficiency broadband anomalous reflection by gradient meta-surfaces. *Nano letters* **12**, 6223-6229 (2012).
116. C. Qu, S. Xiao, S. Sun, Q. He, L. Zhou, A theoretical study on the conversion efficiencies of gradient meta-surfaces. *EPL (Europhysics Letters)* **101**, 54002 (2013).
117. S.-Y. Lee *et al.*, Plasmonic meta-slit: shaping and controlling near-field focus. *Optica* **2**, 6-13 (2015).

118. D. Wintz, P. Genevet, A. Ambrosio, A. Woolf, F. Capasso, Holographic metalens for switchable focusing of surface plasmons. *Nano Lett* **15**, 3585-3589 (2015).
119. D. R. Jackson, C. Caloz, T. Itoh, Leaky-wave antennas. *Proceedings of the IEEE* **100**, 2194-2206 (2012).
120. L. Yin *et al.*, Surface plasmons at single nanoholes in Au films. *Applied physics letters* **85**, 467-469 (2004).
121. J. Tetienne *et al.*, Dipolar modeling and experimental demonstration of multi-beam plasmonic collimators. *New Journal of Physics* **13**, 053057 (2011).
122. J. B. Mueller, F. Capasso, Asymmetric surface plasmon polariton emission by a dipole emitter near a metal surface. *Physical Review B* **88**, 121410 (2013).
123. A. Bouhelier *et al.*, Surface plasmon interference excited by tightly focused laser beams. *Optics letters* **32**, 2535-2537 (2007).
124. F. Keilmann, R. Hillenbrand, Near-field microscopy by elastic light scattering from a tip. *PHILOSOPHICAL TRANSACTIONS-ROYAL SOCIETY OF LONDON SERIES A MATHEMATICAL PHYSICAL AND ENGINEERING SCIENCES*, 787-806 (2004).
125. M. Khorasaninejad *et al.*, Achromatic metasurface lens at telecommunication wavelengths. *Nano letters* **15**, 5358-5362 (2015).
126. G. Zheng *et al.*, Metasurface holograms reaching 80% efficiency. *Nature nanotechnology* **10**, 308-312 (2015).
127. D. Lin, P. Fan, E. Hasman, M. L. Brongersma, Dielectric gradient metasurface optical elements. *science* **345**, 298-302 (2014).
128. A. A. High *et al.*, Visible-frequency hyperbolic metasurface. *Nature* **522**, 192-196 (2015).
129. F. Aieta, M. A. Kats, P. Genevet, F. Capasso, Multiwavelength achromatic metasurfaces by dispersive phase compensation. *Science* **347**, 1342-1345 (2015).
130. D. Vercruysse *et al.*, Unidirectional side scattering of light by a single-element nanoantenna. *Nano letters* **13**, 3843-3849 (2013).
131. J. Lin, P. Genevet, M. A. Kats, N. Antoniou, F. Capasso, Nanostructured holograms for broadband manipulation of vector beams. *Nano letters* **13**, 4269-4274 (2013).

132. M. A. Kats *et al.*, Giant birefringence in optical antenna arrays with widely tailorable optical anisotropy. *Proceedings of the National Academy of Sciences* **109**, 12364-12368 (2012).
133. B. J. Bohn *et al.*, Near-field imaging of phased array metasurfaces. *Nano letters* **15**, 3851-3858 (2015).
134. Y. F. Yu *et al.*, High-transmission dielectric metasurface with 2π phase control at visible wavelengths. *Laser & Photonics Reviews* **9**, 412-418 (2015).
135. K. Huang *et al.*, Silicon multi-meta-holograms for the broadband visible light. *Laser & Photonics Reviews* **10**, 500-509 (2016).
136. M. V. Berry, in *Proceedings of the Royal Society of London A: Mathematical, Physical and Engineering Sciences*. (The Royal Society, 1984), vol. 392, pp. 45-57.
137. Y. Zhang, Y.-W. Tan, H. L. Stormer, P. Kim, Experimental observation of the quantum Hall effect and Berry's phase in graphene. *Nature* **438**, 201-204 (2005).
138. K. Novoselov *et al.*, Two-dimensional gas of massless Dirac fermions in graphene. *nature* **438**, 197-200 (2005).
139. J. Crossno *et al.*, Observation of the Dirac fluid and the breakdown of the Wiedemann-Franz law in graphene. *Science* **351**, 1058-1061 (2016).
140. B. Hunt *et al.*, Massive Dirac fermions and Hofstadter butterfly in a van der Waals heterostructure. *Science* **340**, 1427-1430 (2013).
141. A. K. Geim, I. V. Grigorieva, Van der Waals heterostructures. *Nature* **499**, 419-425 (2013).
142. C.-H. Lee *et al.*, Atomically thin p–n junctions with van der Waals heterointerfaces. *Nature nanotechnology* **9**, 676-681 (2014).
143. R. Mas-Balleste, C. Gomez-Navarro, J. Gomez-Herrero, F. Zamora, 2D materials: to graphene and beyond. *Nanoscale* **3**, 20-30 (2011).
144. L. Li *et al.*, Black phosphorus field-effect transistors. *Nature nanotechnology* **9**, 372-377 (2014).
145. F. Xia, H. Wang, Y. Jia, Rediscovering black phosphorus as an anisotropic layered material for optoelectronics and electronics. *Nature communications* **5**, (2014).
146. D. Basov, M. Fogler, F. G. de Abajo, Polaritons in van der Waals materials. *Science* **354**, aag1992 (2016).

147. P. Alonso-González *et al.*, Controlling graphene plasmons with resonant metal antennas and spatial conductivity patterns. *Science* **344**, 1369-1373 (2014).
148. A. Woessner *et al.*, Highly confined low-loss plasmons in graphene–boron nitride heterostructures. *Nature materials* **14**, 421-425 (2015).
149. J. Chen *et al.*, Optical nano-imaging of gate-tunable graphene plasmons. *Nature* **487**, 77-81 (2012).
150. S. Dai *et al.*, Tunable phonon polaritons in atomically thin van der Waals crystals of boron nitride. *Science* **343**, 1125-1129 (2014).
151. Z. Fei *et al.*, Gate-tuning of graphene plasmons revealed by infrared nano-imaging. *Nature* **487**, 82-85 (2012).
152. Y. Yao *et al.*, Broad electrical tuning of graphene-loaded plasmonic antennas. *Nano letters* **13**, 1257-1264 (2013).
153. M. Engel, M. Steiner, P. Avouris, Black phosphorus photodetector for multispectral, high-resolution imaging. *Nano letters* **14**, 6414-6417 (2014).
154. X. Gan *et al.*, Chip-integrated ultrafast graphene photodetector with high responsivity. *Nature Photonics* **7**, 883-887 (2013).
155. L. Britnell *et al.*, Strong light-matter interactions in heterostructures of atomically thin films. *Science* **340**, 1311-1314 (2013).
156. H. Shi *et al.*, Exciton dynamics in suspended monolayer and few-layer MoS2 2D crystals. *ACS nano* **7**, 1072-1080 (2013).
157. A. Chernikov *et al.*, Exciton binding energy and nonhydrogenic Rydberg series in monolayer WS 2. *Physical review letters* **113**, 076802 (2014).
158. D. Y. Qiu, H. Felipe, S. G. Louie, Optical spectrum of MoS 2: many-body effects and diversity of exciton states. *Physical review letters* **111**, 216805 (2013).
159. C. R. Dean *et al.*, Boron nitride substrates for high-quality graphene electronics. *Nature nanotechnology* **5**, 722-726 (2010).
160. D. Pacile, J. Meyer, C. O. Girit, A. Zettl, The two-dimensional phase of boron nitride: few-atomic-layer sheets and suspended membranes. *Applied Physics Letters* **92**, 133107 (2008).
161. K. Watanabe, T. Taniguchi, H. Kanda, Direct-bandgap properties and evidence for ultraviolet lasing of hexagonal boron nitride single crystal. *Nature materials* **3**, 404-409 (2004).

162. J. D. Caldwell *et al.*, Sub-diffractional volume-confined polaritons in the natural hyperbolic material hexagonal boron nitride. *Nature communications* **5**, (2014).
163. I. Horcas *et al.*, WSXM: a software for scanning probe microscopy and a tool for nanotechnology. *Review of Scientific Instruments* **78**, 013705 (2007).
164. M. Schubert *et al.*, Anisotropy of boron nitride thin-film reflectivity spectra by generalized ellipsometry. *Applied physics letters* **70**, 1819-1821 (1997).
165. X. Li, Y. Gu, R. Luo, L. Wang, Q. Gong, Effects of dielectric anisotropy on surface plasmon polaritons in three-layer plasmonic nanostructures. *Plasmonics* **8**, 1043-1049 (2013).
166. K. M. McPeak *et al.*, Plasmonic films can easily be better: rules and recipes. *ACS photonics* **2**, 326-333 (2015).
167. T. T. Tran, K. Bray, M. J. Ford, M. Toth, I. Aharonovich, Quantum emission from hexagonal boron nitride monolayers. *Nature nanotechnology* **11**, 37-41 (2016).